DISSERTATION

SUBMITTED TO THE

COMBINED FACULTIES FOR THE NATURAL SCIENCES AND FOR MATHEMATICS

OF THE RUPERTO-CAROLA UNIVERSITY OF HEIDELBERG, GERMANY

FOR THE DEGREE OF

DOCTOR OF NATURAL SCIENCES

PRESENTED BY

DIPLOM-PHYSIKER EWALD PUCHWEIN

BORN IN LINZ, AUSTRIA

ORAL EXAMINATION: OCTOBER 17, 2007

ON THE STRUCTURE
OF
GALAXY CLUSTERS

REFEREES: PROF. DR. MATTHIAS BARTELMANN
PROF. DR. EVA GREBEL

Über die Struktur der Galaxienhaufen

Zusammenfassung

Ich gebe in dieser Arbeit einen Überblick über den Stand der Erforschung der Struktur der Galaxienhaufen und präsentiere zwei neue Studien. Diese befassen sich mit Methoden zur Haufenrekonstruktion mittels einer gemeinsamen Röngten-, thermischen Sunyaev-Zeldovich- und Gravitationslinsenanalyse, sowie mit der Untersuchung des Einflusses baryonischer Physik auf den starken Linseneffekt und die Struktur der Galaxienhaufen.

Die von mir vorgestellten Haufenrekonstruktionsmethoden setzen nur axiale Symmetrie bezüglich einer beliebig orientierten Achse voraus. Dichte- und Temperaturverteilungen des Haufengases lassen sich aus Röngten- und Sunyaev-Zeldovich-Daten ermitteln. Kumulative totale Massenprofile und dreidimensionale Gravitationspotentiale können dann aus den Gasverteilungen unter Annahme hydrostatischen Gleichgewichts bestimmt werden. Unabhängig davon, und ohne diese Annahme, lassen sie sich aus Gravitationslinsendaten rekonstruieren. Durch einen Vergleich der beiden Rekonstruktionen lässt sich hydrostatisches Gleichgewicht quantitativ testen. Diese Methoden sind detailliert beschrieben und wurden mithilfe von zunehmend realistischen synthetischen Beobachtungen erfolgreich getestet.

Bisher wurde der Einfluss des Haufengases auf den starken Linseneffekt in Galaxienhaufen vernachlässigt. Hier untersuche ich diesen mithilfe eines Satzes von Haufensimulationen, die Gasdynamik in unterschiedlicher Komplexität enthalten. Es zeigte sich, dass adiabatisches Gas Wirkungsquerschnitte für den starken Linseneffekt entweder unverändert lässt oder etwas verringert, je nach verwendeter Implementierung der künstlichen Viskosität. Radiative Kühlung und Sternbildung hingegen lassen zentrale Dichteprofile steiler werden und erhöhen Linsenwirkungsquerschnitte beträchtlich.

On the Structure of Galaxy Clusters

Abstract

I summarise the state of the scientific exploration of the structure of galaxy clusters and present two new studies, namely, I propose and test a novel method to model clusters by a joint X-ray, thermal Sunyaev-Zeldovich and lensing analysis, and I investigate the impact of baryonic physics on strong cluster lensing and cluster structure.

The three-dimensional reconstruction methods I propose assume only axial symmetry of the cluster with respect to an arbitrarily inclined axis. Cluster gas density and temperature distributions are found from X-ray and Sunyaev-Zeldovich data. Cumulative total-mass profiles and three-dimensional gravitational potentials are then obtained from these gas reconstructions assuming hydrostatic equilibrium, or independently by a gravitational lensing analysis, neglecting it. Hydrostatic equilibrium is quantitatively probed by comparing the two. The methods are described in detail and shown to perform well on progressively realistic synthetic data.

Previous strong cluster lensing studies neglected the impact of the intracluster gas. I investigate it comparing simulations including gas physics at different levels of complexity. I found that adiabatic gas leaves strong lensing cross sections unchanged or somewhat reduces them, depending on the artificial viscosity implementation, while cooling and star formation steepen core density profiles and increase strong-lensing efficiencies considerably.

Contents

Chapter 1

Introduction

1.1 Galaxy clusters - historical remarks

> *"The constellation Virgo and especially the northern wing is one of the constellations which encloses the most nebulae. This catalogue contains 13 which have been determined, viz. Nos. 49, 58, 59, 60, 61, 84, 85, 86, 87, 88, 89, 90 and 91. All these nebulae appear to be without stars and can be seen only in a good sky and near meridian passage. Most of these nebulae have been pointed out to me by M. Méchain."*
>
> -note by Charles Messier in his catalogue, 1781

The quote above shows that the Virgo cluster of galaxies appeared in the scientific literature already in the 1780's, although the true nature of galaxy clusters was by no means recognised at that time. Significant progress was only made after Edwin Hubble identified Cepheid variables in several "nebulae" in the 1920's and could thereby proof that they are far outside the Milky Way and are thus objects similar to the Milky Way rather than parts of it. This allowed correctly interpreting concentrations of such "nebulae" as clusters of galaxies.

In 1933 Fritz Zwicky measured galaxy velocities in nearby galaxy clusters. By then applying the virial theorem he obtained unexpectedly large mass-to-light ratios.

This was the first evidence of dark matter in clusters of galaxies. Since then many other observations, most directly gravitational lensing, have confirmed the necessity of its existence, at least assuming that gravity is correctly understood.

As the earth's atmosphere absorbs most X-rays, X-ray astronomy really started only after the beginning of the Space Age. When galaxy clusters were observed in X-rays, extended emission was discovered [37]. It was interpreted as thermal emission from an about 10-100 million Kelvin hot plasma with which galaxy clusters are filled and which makes them the most luminous X-ray sources on the sky.

During the 1980's galaxy clusters were shown to gravitationally lens background galaxies [114, 115] and distort the cosmic microwave background (CMB) by inverse Compton scattering [16]. Together with X-ray observations this inspired new ways to probe the physics of galaxy clusters.

1.2 A galaxy cluster's constituents

Galaxy clusters are the most massive gravitationally bound objects in the universe and also form most recently in hierarchical models of structure formation. Assuming that gravity is correctly described by general relativity, they must consist of a halo of non-baryonic dark matter, which dominates the cluster's mass and drives its formation, and a baryonic component, which resides mostly in the form of a hot plasma filling the cluster, namely the intra-cluster medium (ICM). However, as apparent from any optical observation of a galaxy cluster, the baryons also fragment into stars, which are primarily gravitationally bound inside the cluster's galaxies. Nevertheless, there is also a population of unbound intra-cluster stars, which contributes to a cluster's optical emission (see e.g. [143]).

The mass budget of a galaxy cluster of about 10^{14}-10^{15} solar masses ($M_\odot$) can be split into roughly 85-90% dark matter and 10-15% baryons (e.g. [68]), with cluster X-ray studies typically yielding slightly smaller baryon mass fractions than inferred from recent CMB data by assuming that there is no efficient mechanism to segregate baryons from dark matter on the scale of galaxy clusters [134, 31, 68]. Of the baryons about the same percentage of 10-15% resides in stars (e.g. [29]).

Galaxy clusters contain about 50-1000 galaxies. Smaller concentrations of galaxies are usually called groups. The population of cluster galaxies differs from the population of field galaxies. In clusters, there is typically a larger fraction of elliptical galaxies and a smaller fraction of spirals, especially close to the cluster centre [89, 135], which is often dominated by a giant elliptical or a cD galaxy.

1.3 Simple analytic models

The formation and evolution of galaxy clusters is governed by non-linear equations. Detailed numerical simulations of the gravitational collapse and of complex baryonic physics are needed to reproduce the structure of galaxy clusters. Conclusions from such simulations will be discussed in Sect. 2.2. There are, however, also a couple of things one can learn from simple analytic models. Some of these analytic models are discussed below.

1.3.1 The spherical collapse model

The probably most simple useful model of halo formation is the collapse of a homogeneous spherically symmetric overdense region in an otherwise isotropic, homogeneous, and expanding universe (e.g. [92]). I will first consider this process in a flat matter dominated universe. The motion of a spherical shell of the overdense region which has a radius r and encloses a mass M is given by

$$\frac{d^2r}{dt^2} = -\frac{GM}{r^2}, \tag{1.1}$$

where G is Newton's constant, t is time, and it is assumed that the spatial extension of the overdensity is much smaller than the size of the horizon, so that the Newtonian approximation is valid. Integrating Eq. (1.1) once yields

$$\frac{1}{2}\left(\frac{dr}{dt}\right)^2 - \frac{GM}{r} = C, \tag{1.2}$$

where C is a constant of integration. The overdense region will first expand with the background space-time, then slow down, eventually turn around and collapse. Collapse only happens for $C < 0$. In this case a solution in parametric form is given by

$$r = A(1 - \cos\Theta), \tag{1.3}$$

$$t = B(\Theta - \sin\Theta) - T, \tag{1.4}$$

where A and B are related by

$$A^3 = GMB^2, \tag{1.5}$$

and T is a constant, which just sets the time coordinate's zero point. Assuming that $r = 0$ at $t = 0$ and using the radius r_m at "turn-around" this can be rewritten as

$$r = \frac{r_m}{2}(1 - \cos\Theta), \tag{1.6}$$

$$t = \frac{\left(\frac{r_m}{2}\right)^{3/2}}{(GM)^{1/2}}(\Theta - \sin\Theta). \tag{1.7}$$

In a matter dominated universe also

$$t = \frac{2}{3H} = \frac{2}{3\sqrt{(8\pi G\rho_b)/3}}, \tag{1.8}$$

is satisfied, where H is the Hubble parameter and ρ_b the background matter density. The enclosed mass M can be written as

$$M = \frac{4\pi}{3} r^3 \rho, \tag{1.9}$$

where ρ is the density in the overdense region. Combining Eqs. (1.6) to (1.9) and solving for ρ/ρ_b one obtains

$$\frac{\rho}{\rho_b} = \frac{9}{2} \frac{(\Theta - \sin\Theta)^2}{(1 - \cos\Theta)^3}, \tag{1.10}$$

for the density in the overdense region in units of the background density. It is also useful to define the density contrast by $\delta \equiv \rho/\rho_b - 1$. One can calculate the density contrast from Eqs. (1.7) and (1.10) to lowest order in t. For small t one finds

$$\delta \approx \frac{3}{20} \left(\frac{6t}{B} \right)^{2/3} = \frac{3}{20} 6^{2/3} (\Theta - \sin\Theta)^{2/3} \equiv \delta_L. \tag{1.11}$$

As the scale factor a is proportional to $t^{2/3}$ during matter domination, δ is proportional to a for small t, or in other words for small overdensities. This is the scale factor dependence found by linear perturbation theory in a matter dominated universe. I, thus, define a linear density contrast δ_L by the right hand side of Eq. (1.11).

One can now analyse how the density contrast δ and the linear approximation δ_L evolve. The overdensity reaches its maximum spatial expansion at $\Theta = \pi$. Then the density contrast is given by $\delta = 4.55$, corresponding to $\rho/\rho_b = 5.55$, and $\delta_L = 1.06$. Then the shell turns around and the overdensity starts to collapse. Formally the density will go to infinity at $\Theta = 2\pi$, when the overdense region has collapsed to a point. For a real halo however, the assumptions of spherical symmetry and negligible random particle motion will break down before and the halo will relax and approach virial equilibrium instead. The virial theorem states that the mean potential energy equals twice the total energy. Using energy conservation and the fact that the kinetic energy at "turn-around" vanishes one finds

$$-2\frac{3GM^2}{5r_m} = -\frac{3GM^2}{5r_{\rm vir}}, \tag{1.12}$$

where the potential energy $E_{\rm pot} = -\frac{3GM^2}{5r}$ of a constant density sphere with radius r has been used. Thus the virial radius $r_{\rm vir}$ of the collapsed halo is given by

$$r_{\rm vir} = \frac{r_m}{2}. \tag{1.13}$$

In the following it is assumed that virialisation happens roughly at collapse time $t_{\rm coll}$, which corresponds to $\Theta = 2\pi$. From Eq. (1.7) it follows that $t_{\rm coll} = 2t_m$, where t_m is the "turn-around" time. For the scale factors one thus obtains $a_{\rm coll} = 2^{2/3}a_m$. The mean density $\rho_{\rm coll}$ of the collapsed halo can then be written as

$$\rho_{\rm coll} = \left(\frac{r_m}{r_{\rm vir}}\right)^3 \rho_m = \left(\frac{r_m}{r_{\rm vir}}\right)^3 [\delta(t_m)+1]\ \rho_b(t_m) = \left(\frac{r_m}{r_{\rm vir}}\right)^3 [\delta(t_m)+1]\ \left(\frac{a_{\rm coll}}{a_m}\right)^3 \rho_b(t_{\rm coll}). \tag{1.14}$$

Plugging in the numbers yields

$$\rho_{\rm coll} \approx 178\,\rho_b(t_{\rm coll}), \tag{1.15}$$

and a linear density contrast of

$$\delta_{L,{\rm coll}} \approx 1.69, \tag{1.16}$$

at collapse time. This means that the virialised region of a halo has an overdensity of roughly 178 with respect to the background density in a matter dominated universe. In different background space-times this numerical value changes and also becomes collapse redshift dependent.

Eq. (1.16) can be interpreted such that a halo has collapsed once the matter density contrast found by linear perturbation theory exceeds 1.69. This value depends only weakly on the background cosmology.

1.3.2 The Press-Schechter mass function

Based on the spherical collapse model one can study the halo mass function [96]. More pedagogical reviews are given in [92, 9]. It is convenient to use the Fourier transform of the density contrast $\delta(\vec{x},t) \equiv \rho(\vec{x},t)/\rho_b(t) - 1$ for this purpose

$$\hat{\delta}(\vec{k},t) \equiv \int d^3x \delta(\vec{x},t) e^{i\vec{k}\cdot\vec{x}}. \tag{1.17}$$

Due to statistical homogeneity and isotropy different Fourier modes are uncorrelated. One can thus define the power spectrum $P(k,t)$ by

$$\langle \hat{\delta}(\vec{k},t) \hat{\delta}^*(\vec{k}',t) \rangle \equiv (2\pi)^3 P(k,t) \delta_D(\vec{k}-\vec{k}'), \tag{1.18}$$

where δ_D is Dirac's delta distribution and $k = |\vec{k}|$. It is also useful to introduce a filtered density contrast

$$\delta_R(\vec{x},t) \equiv \int d^3y \delta(\vec{y},t) W_R(|\vec{x}-\vec{y}|), \tag{1.19}$$

which is obtained by convolving with a window function W_R on a scale R. Then the variance of $\delta_R(\vec{x},t)$ is given by

$$\sigma_R^2(t) \equiv \langle \delta_R(\vec{x},t)^2 \rangle = \int \frac{d^3k}{(2\pi)^3} P(k) |\hat{W}_R(\vec{k})|^2, \tag{1.20}$$

where $\hat{W}_R$ is the Fourier transform of W_R and the Fourier convolution theorem has been used. The normalisation of the power spectrum is usually described by σ_8 which one obtains for $R = 8h^{-1}$Mpc, where h is the reduced Hubble constant.

In the following it is assumed that the filtered density contrast δ_R is normally distributed. Its probability distribution function is then given by

$$p(\delta_R,t) = \frac{1}{\sqrt{2\pi}\sigma_R(t)} \exp\left(-\frac{\delta_R^2}{2\sigma_R^2(t)}\right). \tag{1.21}$$

From the fact that δ_R cannot be smaller than -1 it is clear that this is not an accurate description of the full non-linear density contrast. However, it accurately describes the linear density contrast. The filter radius R can be related to a mass scale $M(R)$ by

$$M(R) = \frac{4\pi}{3} R^3 \rho_b. \tag{1.22}$$

One can then assume that a region at point $\vec{x}$ has collapsed into a halo of mass $M(R)$ or larger, if $\delta_{R'}(\vec{x}, t) > \delta_{L,\mathrm{coll}}$ for some $R' \geq R$. This is the case if either $\delta_R(\vec{x}, t) > \delta_{L,\mathrm{coll}}$ or if $\delta_R(\vec{x}, t) < \delta_{L,\mathrm{coll}}$ but $\delta_{R'}(\vec{x}, t) > \delta_{L,\mathrm{coll}}$ for some $R' > R$. It was shown that the probability for both cases is the same [17], at least when using a window function with a sharp cutoff in k-space. Then the volume fraction $F(M, t)$ that has collapsed into halos of mass M or larger is given by

$$F(M, t) = \int_{\delta_{L,\mathrm{coll}}}^{\infty} 2p(\delta_R, t) d\delta_R. \tag{1.23}$$

The number density dn of halos in the mass interval $[M, M + dM]$ is thus found as

$$\frac{dn}{dM}(M, t) = -\frac{\rho_b}{M} \frac{\partial F(M, t)}{\partial M}. \tag{1.24}$$

Combining everything and performing the integration in Eq. (1.23) and the differentiation in Eq. (1.24) one gets

$$\frac{dn}{dM}(M, t) = -\frac{\rho_b}{M} \sqrt{\frac{2}{\pi}} \frac{\delta_{L,\mathrm{coll}}}{\sigma_R(t)} \frac{\partial \ln \sigma_R(t)}{\partial M} \exp\left(-\frac{\delta_{L,\mathrm{coll}}^2}{2\sigma_R^2(t)}\right). \tag{1.25}$$

This equation allows calculating the halo mass function from the linear power spectrum of density fluctuations. It is remarkably accurate. A comparison with cosmological simulations is discussed in Sect. 2.2.

1.3.3 Isothermal spheres

A simple model of a halo's matter distribution can be obtained by assuming that the kinetic energy of the matter particles is described by a constant temperature T and that the halo is spherically symmetric and in hydrostatic equilibrium. Then

$$\frac{1}{\rho} \frac{dp}{dr} = -\frac{d\phi}{dr} = -\frac{GM_{<r}}{r^2}, \tag{1.26}$$

where $p = \rho k_B T/m$ is the pressure, k_B Boltzmann's constant, m the particle mass, ϕ the gravitational potential and $M_{<r}$ the mass inside radius r. Multiplying by r^2 and taking the derivative with respect to r one obtains a differential equation for the density ρ, namely

$$\frac{d}{dr}\left(r^2 \frac{d\ln\rho}{dr}\right) = -\frac{4\pi G m}{k_B T} r^2 \rho. \tag{1.27}$$

It is solved by the singular density profile

$$\rho(r) = \frac{k_B T}{2\pi G M}\frac{1}{r^2}. \tag{1.28}$$

Such halos are hence called "singular isothermal spheres". Another non-singular solution exists, it can be expanded into a series and there are also several analytic approximations around [82]. It has a constant density core and drops proportional to r^2 for large r.

Both profiles can reproduce flat rotation curves. A comparison to simulated and observed profiles will be given in Sects. 2.2 and 3.4.

1.3.4 Scaling relations

It is possible to obtain relations between a cluster's mass and different cluster observables by simple scaling arguments. Using the following proportionality relation between a cluster's potential energy $E_{\rm pot}$, its mass M and its size R,

$$E_{\rm pot} \propto -\frac{M^2}{R}, \tag{1.29}$$

as well as a relation between cluster radius and mass, given by $R \propto M^{1/3}$, one finds

$$E_{\rm pot} \propto -M^{5/3}. \tag{1.30}$$

One can then apply the virial theorem, $2\overline{E}_{\rm kin} = -\overline{E}_{\rm pot}$ and use the proportionality of the mean kinetic energy $\overline{E}_{\rm kin}$ to the product of temperature T and mass M to obtain

$$TM \propto M^{5/3} \Rightarrow T \propto M^{2/3}. \tag{1.31}$$

The bolometric X-ray luminosity L_{X} of a cluster is roughly proportional to the product of its mass, density and temperature's square root (see Sect. 1.4.1 for a more detailed discussion of X-ray emission). Using the scaling relations above one can write this as

$$L_{\mathrm{X}} \propto M \frac{M}{R^3} T^{1/2} \propto M^{4/3} \propto T^2, \tag{1.32}$$

to get a scaling relation between bolometric X-ray luminosity and temperature.

1.4 Cluster observables

Galaxy clusters can be observed in many different parts of the electromagnetic spectrum. Optical observations allow studying cluster galaxies, their velocities and, by analysing distorted images of background galaxies, also cluster mass distributions. X-ray observations show the thermal emission from the hot ICM and allow determining the ICM's temperature and density. Alternative and complementary probes of the ICM's physics are microwave observations of the Sunyaev-Zel'dovich (SZ) effect. By this term distortions of the CMB spectrum due to inverse Compton scattering with ICM electrons are referred to. Below, cluster X-ray and SZ emission and cluster lensing signals are described in more detail.

1.4.1 Thermal X-ray emission

Galaxy clusters are filled with 10^7-10^8 K ($\sim$ 1-10 keV) hot plasma. This plasma thermally emits radiation by several processes. The dominant process is free-free bremsstrahlung but also line emission from metals present in the ICM is relevant.

The emitted energy at frequency ν per unit time, unit volume and unit frequency due to free-free bremsstrahlung by a hot plasma is given by (e.g. [105])

$$\frac{dE}{dV\,dt\,d\nu} = \sum_i \left[\frac{32\pi Z_i^2 n_{Z_i} n_e e^6}{3 m_e c^3} \sqrt{\frac{2\pi}{3 m_e k_B T}}\, \bar{g}_{\mathrm{ff},i}(\nu, T) \exp\left(-\frac{h\nu}{k_B T}\right) \right], \tag{1.33}$$

where the sum extends over all species of ions and Z_i and n_i are the atomic number and number density of species i, respectively. n_e is the number density of free electrons, e the electron charge, m_e the electron mass, c the speed of light, h Planck's constant and T the plasma's temperature. $\bar{g}_{ff,i}(\nu, T)$ is a velocity averaged Gaunt factor that takes care of quantum effects in the scattering of electrons with ions of species i. However, except for the Gaunt factors' exact numerical values, Eq. (1.33) can be most conveniently obtained by using classical electrodynamics, considering only dipole emission, applying Born's approximation to the electron-ion scattering processes, and assuming a Maxwellian electron velocity distribution. The proportionality to the product of ion and electron densities of course just reflects the fact that bremsstrahlung is a two-body process.

The energy emitted in an energy band with minimum photon energy E_a and maximum photon energy E_b can be found from Eq. (1.33) by integration over the frequency ν. Neglecting the weak dependence of the Gaunt factor on T, ν, and Z_i and using a reasonable average value of 1.2 [41] one obtains

$$\frac{dE}{dV dt} = \frac{1.17 \times 10^{-23}}{1+f} \left(\frac{k_B T}{\mathrm{keV}}\right)^{1/2} \left(\frac{n_e}{\mathrm{cm}^{-3}}\right)^2 \left[\exp\left(-\frac{E_a}{k_B T}\right) - \exp\left(-\frac{E_b}{k_B T}\right)\right] \mathrm{erg\,cm^{-3}\,s^{-1}}, \tag{1.34}$$

for a fully ionised hydrogen-helium-plasma with hydrogen mass fraction f.

A more precise determination of the ICM's X-ray emission would not only require using the exact frequency averaged Gaunt factor but also to consider line emission from metals present in the ICM, which gets enriched with material that has been processed in stars by various mechanisms like ram-pressure stripping, galactic winds and galaxy-galaxy interactions. Typical metal abundances in the ICM are about 0.3 times the solar value [33]. Fortunately, simulating such a hot plasma's X-ray emission is made easy by publicly available software packages like XSPEC [4], that allow calculating a plasma's X-ray emission with emission models that take these effects into account.

1.4.2 The Sunyaev-Zel'dovich effect

Interactions between CMB photons and the ICM change the spectrum of the microwave background when seen through a galaxy cluster, as some of the CMB photons are shifted towards higher energies by inverse Compton scattering with the ICM's thermal distribution of hot electrons. This can be quantified by plugging a Planck spectrum into Kompaneets' equation and assuming that deviations from it are small, as was first done by Zel'dovich and Sunyaev [142]. Hence, the effect is called thermal Sunyaev-Zel'dovich effect.

Performing the calculation one obtains

$$\frac{\Delta n_{\mathrm{t}SZ}(\nu)}{n_0(\nu)} = xy\frac{e^x}{e^x-1}\left[\frac{x}{\tanh(x/2)} - 4\right], \tag{1.35}$$

where n_0 is the CMB photon occupation number that would be observed without the cluster and $\Delta n_{\mathrm{t}SZ}$ denotes its change due to inverse Compton scattering with thermal ICM electrons. x is defined as the ratio of the considered photon energy to the energy corresponding to the CMB temperature, namely $x \equiv h\nu/k_B T_{CMB}$. y is the so called Compton y-parameter given by

$$y = \int \frac{k_B T}{m_e c^2} n_e \sigma_T c dt, \tag{1.36}$$

where the integration follows the line-of-sight, σ_T is the Thomson cross section, and T and n_e are the temperature and electron number density at the position passed by the light ray at time t. Note that the Compton y-parameter and thus the distortion of the spectrum does not depend on the cluster redshift. The independence on redshift is also reflected by the fact that a photon's x value is not changed by the expansion of the universe, as both ν and T_{CMB} scale as the inverse a^{-1} of the scale factor.

$\Delta n_{\mathrm{t}SZ}$ is negative for $x < 3.83$ and positive otherwise. For $T_{CMB} = 2.726$ K [66] this corresponds to a decrease in CMB surface brightness for $\nu < 217$ GHz and to an increase for $\nu > 217$ GHz. The ratio of the surface brightness change to the original surface brightness is of course equal to the ratio of the corresponding occupation numbers described by Eq. (1.35). The fact that the total photon number is not affected by the scattering makes also immediately clear that the CMB spectrum observed through a cluster is no longer Planckian.

Of course ICM electrons can not only transfer energy to CMB photons due to their thermal motion, but also due to a bulk motion of the ICM in the CMB frame. This is called the kinetic Sunyaev-Zel'dovich effect [125]. Then, in the ICM's rest frame the CMB has a dipole structure. However, when the ICM velocity is very small compared to the speed of light, the effect of this dipole structure is averaged out by Thomson scattering. Hence, the temperature change due to the kinetic SZ effect can be described as a Doppler shift of the scattered radiation from the ICM's to the observers rest frame and is thus given by

$$\frac{\Delta T_{\mathrm{k}SZ}}{T_0} = -\int \frac{v_r}{c} n_e \sigma_T c dt, \tag{1.37}$$

where v_r is the ICM's velocity parallel to line of sight, which is positive for a receding ICM and negative if it is approaching the observer. It is assumed that both the thermal and the kinetic SZ effects are small. Then, the effects superpose linearly and can be added after converting Eqs. (1.35) and (1.37) to intensity ratios. Note that $\Delta T_{\mathrm{k}SZ}$ is either positive or negative for all frequencies. It is thus possible to separate the kinetic and the thermal SZ effect from each other as well as from other CMB anisotropies by observing them in several different frequency bands.

1.4.3 Gravitational lensing

General relativity predicts that light is deflected by gravity. Observing this effect can be used to study the masses that induce the gravitational field (see e.g. [80] for a pedagogical review of gravitational lensing).

The metric of a locally flat Minkowskian spacetime that is only weakly perturbed by the mass distribution of a gravitational lens can be written as

$$ds^2 = -(1 + \frac{2\phi}{c^2})dt^2 + (1 - \frac{2\phi}{c^2})d\vec{x}^2, \tag{1.38}$$

where ϕ is the Newtonian potential and $|\phi| \ll c^2$ is assumed. It is also assumed that the matter constituting the lens moves at non-relativistic speeds. One can define an effective index of refraction by

$$n \equiv \frac{c}{(|d\vec{x}|/dt)_{\text{light ray}}} = 1 - \frac{2\phi}{c^2}, \tag{1.39}$$

where $|d\vec{x}|/dt$ is to be evaluated for a light ray and may in general depend on position and direction. The second equality holds in a spacetime whose metric is given by Eq. (1.38). Then it follows from the relativistic version of Fermat's principle, which states that a light ray's arrival time is stationary, that a lightlike geodesics satisfies $\delta \int n|d\vec{x}| = 0$ [110]. The corresponding Euler-Lagrange equation is

$$\frac{d\vec{e}}{dl} = -\frac{2\vec{\nabla}_\perp \phi}{c^2}, \tag{1.40}$$

where $dl = |d\vec{x}|$, $\vec{e}$ is the light ray's unit tangent vector and $\vec{\nabla}_\perp \phi$ is the projection of $\vec{\nabla}\phi$ onto the plane orthogonal to the ray. Thus, the deflection angle is given by

$$\vec{\hat{\alpha}} \equiv \vec{e}_{\text{in}} - \vec{e}_{\text{out}} = \frac{2}{c^2} \int \vec{\nabla}_\perp \phi \, dl, \tag{1.41}$$

where $\vec{e}_{\text{in}}$ is the original direction of the light ray and $\vec{e}_{\text{out}}$ is its direction after passing the lens. In principle the integration should follow the deflected light ray. However, if the deflection is small and occurs only close to a single lens one can also integrate along an unperturbed ray with the same impact parameter.

It is convenient to introduce the reduced deflection angle $\vec{\alpha}$, which is the angular distance on the sky between a source and its image

$$\vec{\alpha} \equiv \frac{D_{ds}}{D_s} \vec{\hat{\alpha}}, \tag{1.42}$$

where D_{ds} and D_s are the angular diameter distances of the source from the lens and from the observer, respectively. The angular positions of the source $\vec{\beta}$ and the image $\vec{\theta}$ are then related by

$$\vec{\beta} = \vec{\theta} - \vec{\alpha}(\vec{\theta}). \tag{1.43}$$

It is further useful to define the lensing potential ψ by

$$\psi = \frac{D_{ds}}{D_d D_s} \frac{2}{c^2} \int \phi \, dl, \tag{1.44}$$

where D_d is the angular diameter distance of the lens from the observer. Then the reduced deflection angle can be written as

$$\vec{\nabla}_{\vec{\theta}} \psi = \vec{\alpha}, \tag{1.45}$$

where $\vec{\nabla}_{\vec{\theta}}$ is the gradient in the lens plane angular coordinate $\vec{\theta}$, or in other words $\vec{\nabla}_{\vec{\theta}} = D_d \vec{\nabla}_{\perp}$ at the lens. Using Eq. (1.44) and Poisson's equation for the three-dimensional gravitational potential, one finds the following two-dimensional Poisson's equation as the latter's scaled projection

$$\vec{\nabla}^2_{\vec{\theta}} \psi = 2\kappa, \tag{1.46}$$

where κ is called convergence and given by

$$\kappa = \frac{\Sigma}{\Sigma_{\mathrm{crit}}}, \tag{1.47}$$

Σ is the surface mass density, and the critical density $\Sigma_{\rm crit}$ defines a characteristic surface mass density scale

$$\Sigma_{\rm crit} = \frac{c^2}{4\pi G}\frac{D_s}{D_d D_{ds}}. \tag{1.48}$$

Another important quantity is the shear. Its components γ_1 and γ_2 are given by

$$\gamma_1(\vec{\theta}) = \frac{1}{2}\left(\frac{\partial^2\psi}{\partial\theta_1\partial\theta_1} - \frac{\partial^2\psi}{\partial\theta_2\partial\theta_2}\right) \equiv \gamma(\vec{\theta})\cos\left(2\phi(\vec{\theta})\right), \tag{1.49}$$

$$\gamma_2(\vec{\theta}) = \frac{\partial^2\psi}{\partial\theta_1\partial\theta_2} = \frac{\partial^2\psi}{\partial\theta_2\partial\theta_1} \equiv \gamma(\vec{\theta})\sin\left(2\phi(\vec{\theta})\right), \tag{1.50}$$

where θ_1 and θ_2 are the components of the lens plane angular coordinate $\vec{\theta}$. With these definitions one can write the Jacobian matrix A of the lens mapping described by Eq.(1.43) as

$$A \equiv \frac{\partial\vec{\beta}}{\partial\vec{\theta}} = \delta_{ij} - \frac{\partial^2\psi}{\partial\theta_i\partial\theta_j} = \begin{pmatrix} 1-\kappa-\gamma_1 & -\gamma_2 \\ -\gamma_2 & 1-\kappa+\gamma_1 \end{pmatrix}, \tag{1.51}$$

or

$$A = (1-\kappa)\begin{pmatrix} 1 & 0 \\ 0 & 1 \end{pmatrix} - \gamma\begin{pmatrix} \cos(2\phi) & \sin(2\phi) \\ \sin(2\phi) & -\cos(2\phi) \end{pmatrix}. \tag{1.52}$$

From the last equation one can easily get an intuitive understanding of the effects of convergence and shear. Convergence alone causes an isotropic magnification, while shear introduces anisotropy. For example for a circular source with unit radius an elliptic image is observed with major axis $(1-\kappa-\gamma)^{-1}$ and minor axis $(1-\kappa+\gamma)^{-1}$. The orientation of the major axis is given by the angle ϕ.

The magnification μ due to gravitational lensing can be obtained from the Jacobian matrix A and is given by

$$\mu = (\det A)^{-1} = \left[(1-\kappa)^2 - \gamma^2\right]^{-1}. \tag{1.53}$$

For large enough surface densities and shear fields, there will be curves were $\det A$ vanishes and thus μ goes to infinity. These curves are called critical curves. The corresponding curves in the source plane are called caustics. Highly magnified, but strongly distorted images like giant arcs are typically found close to such critical curves. The relevant source is then close to the caustic.

One can distinguish tangential and radial critical curves. Close to the former the magnification in tangential direction with respect to the lens is large, while close to the latter the radial magnification dominates. Images of background galaxies that appear along a cluster's tangential or radial critical curve are thus extended in tangential or radial direction respectively and hence called tangential or radial arcs.

Typically one also distinguishes different regimes of cluster lensing. Strong lensing can be observed only close to the critical curves and leads to strongly distorted and highly magnified arcs, while weak lensing refers to small distortions and thus small changes in the observed ellipticities of background galaxies, which can be analysed only statistically, but also allow probing the outskirts of a cluster's mass distribution.

1.5 Open questions

Since Charles Messier's days, the scientific exploration of galaxy clusters has made enormous progress. However, there are still many open questions related to clusters of galaxies.

The most obvious and probably also most fundamental open question concerns the nature of the dark matter that makes up most of a cluster's mass and drives its formation. Closely related is the question how dark matter is distributed in halos of different mass. The amount of substructure in dark matter halos and the central slopes of density profiles are still not well constrained.

The baryonic physics is better known on a fundamental level. However, due to its complexity, many processes relevant for the evolution of clusters still evade a thorough understanding. AGN feedback, radio halos, cosmic rays, magnetic fields, non-thermal pressure components, metal enrichment or soft X-ray excess are just some of the baryonic processes in clusters that are only partly understood, not to mention difficulties with understanding the formation, evolution and properties of clusters' galaxy populations.

Methods to analyse clusters data also need improvement. Even estimates of the most basic cluster properties like cluster mass or concentration have a huge scatter. Deviations are most likely related to the breakdown of simple commonly used assumptions like spherical symmetry, hydrostatic equilibrium or negligible non-thermal pressure. In Chapter 3, I will propose and test novel methods to relax these assumptions.

Also the abundance of clusters as a function of redshift is not well known. Its accurate determination, although difficult, would be very valuable for probing cosmology, e.g. for constraining σ_8 or the dark energy equation of state. A more detailed discussion is given in Chapter 4.

An interesting consistency check is to compare the theoretically expected abundance of giant arcs to the one inferred from observations. It is still not clear whether or not they are compatible. In Chapter 5, I will use gasdynamical cluster simulations to analyse how baryonic physics affects such a comparison.

Chapter 2

Cluster simulations

Since the beginning of the computer age astrophysicists used computers to simulate the formation and evolution of astrophysical objects and cosmic structures. However, the first N-body simulation was done even before digital computers were available for that purpose. Its results were published in 1941 [40]. The first real three-dimensional cluster simulation followed 29 years later [93]. Since then the number of particles, whose interactions can be simulated, has increased by a factor larger than 10^7 to about $N \approx 10^{10}$ [122]. About half of this progress is due to better algorithms, the other half due to faster computers.

2.1 An introduction to cosmological simulations

I will first discuss how the motion of matter that interacts only by gravity can be simulated. Then methods to follow the hydrodynamics of the baryonic gas will be introduced.

2.1.1 The dynamics of collisionless matter

In principle one could follow the dynamics of collisionless gravitationally interacting matter, like cold dark matter (CDM), by solving the corresponding Boltzmann equation on a grid in six-dimensional position-momentum phase space. However, this is computationally overly expensive.

Thus, one typically applies the N-body technique and samples phase space by particles, whose interactions and trajectories are then followed. Usually a gravitational force law that is softened for small distances is used in order to prevent large unphysical scattering angles for closely passing particles.

However, calculating the $\sim N^2$ forces between all particles by direct summation is still unfeasible for large particle numbers N. A faster way, than this particle-particle (PP) method, is to project the masses of all simulation particles onto a grid and solve Poisson's equation in Fourier space to obtain the gravitational potential, which can then be used to update the particles' velocities. However, in such particle-mesh (PM) schemes the force resolution is limited by the dimension of the grid. Structures smaller than a few mesh lengths can not be accurately resolved and increasing the grid size is computationally expensive.

An alternative is to use a combination of the direct summation and the PM schemes (see e.g. [28]). Long range forces can be quickly calculated using the PM method, while corrections to the short range forces can be made by direct summation. This particle-particle-particle-mesh (PPPM or P^3M) scheme has been widely used to simulate cold dark matter universes.

Also tree codes allow a fast and accurate determination of the gravitational forces between simulation particles. They arrange the particles into cells and use only the total mass and the centre of mass of all particles in a cell to calculate their forces

[8]. The used cell size depends on the distance from the point, where the force shall be calculated. This reduces the required number of operations from $\mathcal{O}(N^2)$ to $\mathcal{O}(N \log N)$. Recently combinations of tree and PM codes have been used [5]. Again the long range forces are found with the PM scheme, while the short range forces are calculated using the tree algorithm.

2.1.2 Simulating the baryonic gas with SPH

In the previous subsection I discussed methods to simulate the dynamics of collisionless matter that interacts only by gravity. However, for gas particles collisions are important and pressure forces have to be taken into account. The gravitational interaction of baryonic gas can be simulated as above, but temperature and pressure forces need to be calculated in addition. For that the gas is considered as a fluid.

One can either follow its hydrodynamics on a three-dimensional grid or represent the gas by particles and calculate the pressure forces between them. I will first comment on the former method and then discuss the latter in more detail.

The difficulty with solving the hydrodynamics on a grid is that with an equally spaced grid, one can either not reach a high dynamic range or needs enormous amounts of computing resources. A more efficient way is to use adaptive mesh refinement (AMR) methods [88], which adaptively refine the mesh length and use small mesh lengths only in high density regions, where they are required to resolve small scale structure. Such AMR codes have been successfully used for many astrophysical purposes [87].

Alternatively one can represent the baryonic gas by particles, assign a mass, density, and thermal energy to each of them and follow their hydrodynamics [35, 75].

The equations that need to be solved are (e.g. [123]) the continuity equation

$$\frac{d\rho}{dt} + \rho\vec{\nabla}\cdot\vec{v} = 0, \tag{2.1}$$

where ρ is the gas density, $\vec{v}$ its velocity field and d/dt the Lagrangian derivative given by

$$\frac{d}{dt} = \frac{\partial}{\partial t} + \vec{v}\cdot\vec{\nabla}, \tag{2.2}$$

the Euler equation

$$\frac{d\vec{v}}{dt} = -\frac{\vec{\nabla}p}{\rho} - \vec{\nabla}\phi, \tag{2.3}$$

where p is gas pressure and ϕ the gravitational potential, as well as the equation for the time evolution of the internal energy per unit mass u

$$\frac{du}{dt} = -\frac{p}{\rho}\vec{\nabla}\cdot\vec{v} - \frac{\Lambda(u,\rho)}{\rho}, \tag{2.4}$$

where the cooling function $\Lambda(u,\rho)$ describes external sources or sinks of heat, like for example radiative cooling.

In order to represent the smooth gas distribution, the particles are not considered pointlike but extended. Thus this method is called "smoothed particle hydrodynamics" or SPH. The particles' spatial extensions are described by a kernel function $W(\vec{r}-\vec{r'},h)$, where h is a kernel radius, also called the SPH smoothing length. The kernel satisfies $\int W(\vec{r}-\vec{r'},h)d^3r' = 1$ and $\lim_{h\to 0} W(\vec{r}-\vec{r'},h) = \delta_D(\vec{r}-\vec{r'})$. Using it one can define an integral interpolant of a function $A(\vec{r})$ by

$$A_I(\vec{r}) = \int d^3r' A(\vec{r'})W(\vec{r}-\vec{r'},h). \tag{2.5}$$

In the SPH formalism it is approximated by a summation interpolant

$$A_S(\vec{r}) = \sum_i \frac{m_i}{\rho_i} A_i W(\vec{r}-\vec{r}_i,h), \tag{2.6}$$

where the sum is over all SPH particles and A_i is the value of quantity A at the position of particle i. m_i, ρ_i and $\vec{r}_i$ are its mass, density and position, respectively.

Thus m_i/ρ_i is essentially the volume occupied by particle i. Often a kernel that vanishes for $|\vec{r}-\vec{r'}| > h$ is chosen, so that only nearby particles need to be considered in the sum. In the SPH formalism all quantities are approximated by the above or similar summation interpolants. I will thus omit the "S" for summation interpolant in the following.

Derivatives can be obtained in a similar way, namely by

$$\vec{\nabla} A(\vec{r}) = \sum_i \frac{m_i}{\rho_i} A_i \vec{\nabla} W(\vec{r}-\vec{r}_i, h). \tag{2.7}$$

There is no unique way of performing such SPH approximations. For example instead of using Eq. (2.7) one could use

$$\vec{\nabla} A(\vec{r}) = \vec{\nabla} A(\vec{r}) - A(\vec{r}) \vec{\nabla} 1, \tag{2.8}$$

to rewrite $\vec{\nabla} A(\vec{r})$ before the interpolation and then evaluate the terms $\vec{\nabla} A(\vec{r})$, $A(\vec{r})$, and $\vec{\nabla} 1$ separately in order to reduce particle noise. The latter is then given by $\vec{\nabla} 1 = \sum_i \frac{m_i}{\rho_i} \vec{\nabla} W(\vec{r}-\vec{r}_i, h)$.

In SPH the smoothing length h is not constant. A value h_i, depending on the local particle density, is assigned to each particle. Thus Eq. (2.6) could be written as $A(\vec{r}) = \sum_i \frac{m_i}{\rho_i} A_i W(\vec{r}-\vec{r}_i, h_i)$. However in SPH simulations the interpolants are evaluated at the positions of other particles. Hence, there are two ways of interpreting the summation for calculating the value of some quantity at the position of particle j. Either as collecting the contributions of all nearby extended particles using their kernel functions $W(\vec{r}_j - \vec{r}_i, h_i)$ or as sampling the space around $\vec{r}_j$ using the other particles only as sampling points and assigning a weight proportional to their volume and the kernel $W(\vec{r}_j - \vec{r}_i, h_j)$ of particle j to them. Sometimes symmetric versions are used (see e.g. Eq. (2.10) below).

In SPH simulations, typically the density is computed directly from the particle distribution at each timestep, namely by

$$\rho_j = \sum_i m_i W(\vec{r}_j - \vec{r}_i, h_j). \tag{2.9}$$

The particles' accelerations and internal energy changes could be calculated directly from Eqs. (2.3) and (2.4) by using SPH approximations for the terms $-\frac{\vec{\nabla}p}{\rho}$ and $-\frac{p}{\rho}\vec{\nabla}\cdot\vec{v}$.

Typically however, additional viscosity terms are added to both equations in order to allow capturing shock fronts, which are otherwise to narrow to be resolved by SPH simulations. Adding a small amount of artificial viscosity broadens the shock fronts, so that they can be resolved by SPH, and allows entropy generation, which microphysics provides in real gas shocks. A disadvantage of using artificial viscosity is that it can cause unphysical, excess heating also where the viscosity is not required to capture shocks. Probably most widely used is the Monaghan-Balsara form of artificial viscosity [76, 7], where the viscous acceleration is given by

$$\left.\frac{d\vec{v}_j}{dt}\right|_{\text{visc}} = -\sum_i m_i \Pi_{ij} \vec{\nabla}_j \left[\frac{1}{2}W(\vec{r}_j - \vec{r}_i, h_j) + \frac{1}{2}W(\vec{r}_j - \vec{r}_i, h_i)\right]. \tag{2.10}$$

Here Π_{ij} is defined by

$$\Pi_{ij} = \frac{-\alpha\frac{1}{2}(c_i + c_j)\mu_{ij} + \beta\mu_{ij}^2}{\frac{1}{2}(\rho_i + \rho_j)} \quad \text{for} \quad (\vec{v}_i - \vec{v}_j)\cdot(\vec{r}_i - \vec{r}_j) < 0, \tag{2.11}$$

or in other words for approaching particles, and by $\Pi_{ij} = 0$ otherwise. c_i and c_j are the sound speeds at the positions of particles i and j respectively and μ_{ij} is given by

$$\mu_{ij} = \frac{\frac{1}{2}(h_i + h_j)(\vec{v}_i - \vec{v}_j)\cdot(\vec{r}_i - \vec{r}_j)}{(\vec{r}_i - \vec{r}_j)^2 + \eta^2}. \tag{2.12}$$

α, β and η are free parameters. I will comment on their choice in Sect. 2.3, when I present the simulated cluster sample that is used throughout this work.

Additional baryonic physics, like radiative cooling, can be included in SPH simulations. Also more complicated processes, like star formation and associated feedback can be taken into account by using sub-resolution models.

2.2 The structure of simulated clusters

In the mid 1990's Julio Navarro, Carlos Frank and Simon White showed that the density profiles of numerically simulated cold dark matter halos with different mass can be well fitted by scaling a simple universal density profile [84, 85]. The profile, which was hence called NFW profile, can be written as

$$\rho = \frac{4\rho_s}{\frac{r}{r_s}(1+\frac{r}{r_s})^2}, \tag{2.13}$$

where r_s is a characteristic radius and ρ_s fixes the profile's normalisation. It is shallower than isothermal for $r \ll r_s$ and steeper for $r \gg r_s$. The ratio $c \equiv r_{200}/r_s$ is called concentration. Here r_{200} denotes the radius inside which the mean density is 200 times the critical density of the universe. The NFW profile is widely used in astrophysics and was confirmed by other studies (e.g. [23, 94]), although some authors find somewhat steeper inner slopes (e.g. [77, 34]).

The shape of dark matter halos is much better described by triaxial ellipsoids than by spheres [43, 1]. The mean axis ratios depend on halo mass, with cluster-sized halos being less spherical than lower mass galactic halos. Typical minor to major axis ratios for cluster halos are around 0.5.

Numerical studies of the halo mass function showed that it is qualitatively well described by the Press-Schechter formalism. Quantitatively, however, the Press-Schechter mass function slightly overpredicts the abundance of low mass halos and underpredicts the abundance of high mass halos (see e.g. [113, 42]). More accurate fitting formulae are provided in these references. Better agreement with theoretical predictions can be achieved by considering ellipsoidal rather then spherical collapse for the derivation of a mass function [112].

2.3 The cluster sample

The numerical cluster simulations that are used throughout this work were carried out by Klaus Dolag with GADGET-2 [118], a new version of the parallel TreeSPH simulation code GADGET [123]. It uses an entropy-conserving SPH formulation [119], and allows to include radiative cooling and heating by a UV background. Star formation and feedback processes can be treated with a sub-resolution model for the multi-phase structure of the interstellar medium [120]. For some of the cluster simulations a new method to provide heat conduction in SPH simulations [44] was used. It is stable and conserves thermal energy, even when using individual and adaptive time-steps. An isotropic effective conductivity with a fixed fraction of the Spitzer rate [117] is assumed.

I used four massive simulated galaxy clusters (called *g1*, *g8*, *g51*, and *g72*), spanning a mass-range between $1.3 \times 10^{15}\, h^{-1} M_\odot$ and $2.3 \times 10^{15}\, h^{-1} M_\odot$, as well as the three largest halos of a simulation of a super-cluster region (called *g696*), which range in mass between $0.8 \times 10^{15}\, h^{-1} M_\odot$ and $1.5 \times 10^{15}\, h^{-1} M_\odot$. All clusters were extracted from the same dissipation-less (dark-matter-only) parent simulation with a box-size of $479\, h^{-1}$ Mpc of a flat ΛCDM cosmology with a matter density parameter $\Omega_m = 0.3$, a reduced Hubble constant $h = 0.7$, and an amplitude of matter fluctuations given by $\sigma_8 = 0.9$ (see [137]).

They were then re-simulated with an increased mass and force resolution using the "Zoomed Initial Conditions" (ZIC) technique [126], which means that their Lagrangian volumes in the initial domain were populated with more particles and appropriate small-scale power was added. The initial particle distributions were of glass type [133]. The initial region was selected by an iterative process involving several low-resolution, dissipation-less re-simulations to optimise the simulated volume. This ensures that all haloes are free of contaminating boundary effects out to at least 3 to 5 times the virial radius. Thus these simulations also adequately resolve the clusters' outskirts and include the effects of filaments connected to them.

To introduce gas into the high-resolution region of gasdynamical simulations, each parent particle was split into a gas and a dark-matter particle, which were then displaced by half the original mean inter-particle distance such that their centre-of-mass and momentum were conserved. A baryon density parameter $\Omega_\mathrm{b} = 0.04$ was assumed. The resulting mass resolution of these simulations is $m_\mathrm{DM} = 1.13 \times 10^9\,h^{-1}M_\odot$ and $m_\mathrm{gas} = 1.7 \times 10^8\,h^{-1}M_\odot$ for dark matter and gas particles within the high-resolution region, respectively. The cluster were thus resolved with between 10^6 and 4×10^6 particles.

For all simulations, a gravitational softening length of $\epsilon = 30.0\,h^{-1}\,\mathrm{kpc}$ comoving was used for redshifts $1 + z > 6$, which was then switched to a physical softening length of $\epsilon = 5.0\,h^{-1}\,\mathrm{kpc}$ for $1 + z < 6$.

Five different types of simulations of this galaxy-cluster set were used, namely:

- dark matter only simulations (DM)
- simulations that follow the adiabatic evolution of the gas but ignore radiative cooling (GAS)
- simulations including radiative cooling, heating by a UV background, and a treatment of star formation and feedback processes (CSF)
- simulations additionally including thermal conduction at a fixed fraction of $\kappa = 1/3$ of the Spitzer rate (CSFC)
- a second kind of simulations with adiabatic gas with a different implementation of artificial viscosity, it is suppressed where not numerically needed (GAS_NV)

For the four massive clusters *g1*, *g8*, *g51* and *g72* all five types of simulations were available, while for the three cluster-sized halos extracted from the super-cluster region I only had DM and GAS runs. All different simulations of a specific cluster were started from the same initial conditions, so as to allow a direct comparison and studying the impact of gas physics on cluster properties.

The feedback scheme in the CSF and CSFC runs was calibrated to produce a wind velocity of $\approx 350\,\mathrm{km\,s^{-1}}$. The choice of κ in the CSFC simulations is suitable in the presence of magnetised domains with randomly oriented B-fields (e.g. [108]) or for a chaotically tangled magnetic field [81].

In the GAS, CSF and CSFC simulations the artificial viscosity implementation is based on the Monaghan-Balsara form given by Eq. (2.11). However an additional viscosity limiting factor f_{ij} was used. It is the mean between particles i and j of

$$f_i = \frac{|\langle \vec{\nabla} \cdot \vec{v} \rangle_i|}{|\langle \vec{\nabla} \cdot \vec{v} \rangle_i| + |\langle \vec{\nabla} \times \vec{v} \rangle_i| + \sigma_i}. \tag{2.14}$$

This limiting factor suppresses spurious angular momentum and vorticity transfers, as suggested in [124] for simulations of galactic discs. The following parameters were used in this artificial viscosity implementation $\alpha = 0.75$, $\beta = 2\alpha$, $\eta = \frac{0.01}{2}(h_i + h_j)$, and $\sigma_i = 0.0001 c_i / h_i$.

In the GAS_NV simulations the build-up of viscosity is damped in the time domain, resulting in a reduced artificial viscosity where it is not needed. In combination with the absence of a limiting physical viscosity this allows stronger turbulence in the centres of clusters simulated with this scheme. In contrast to the artificial viscosity implementation in the GAS, CSF and CSFC simulations, the viscosity parameter α in Eq. (2.11) is no longer considered a constant but an evolving particle property as proposed in [78]. Thus, every particle evolves its own parameter α_i. It does so by

$$\frac{d\alpha_i}{dt} = -\frac{\alpha_i - \alpha_{min}}{\tau} + S_i, \tag{2.15}$$

which causes it to decay to a minimum value $\alpha_{min} = 0.01$ with e-folding time τ. The latter is adjusted so that α_i decays over two smoothing lengths after the shock. The source term S_i, which lets α_i grow as particles approach a shock, was assumed to be

$$S_i = S^* f_i \max(0, -|\langle \vec{\nabla} \cdot \vec{v_i} \rangle_i|), \tag{2.16}$$

where $S^* = 0.7$ was chosen. Further details on this implementation and its consequences for the generation of turbulence within the intra-cluster medium are described in [26].

2.4 The impact of baryonic physics on cluster structure

Before using the simulated galaxy clusters to test cluster reconstruction methods and study strong lensing, I compared their shapes, density profiles, and angular momentum distributions for the five different physical gas models used in the simulations. This comparison was also published in [99].

Figure 2.1 shows typical profiles of the total density (dark matter and baryons) for the different types of gas physics. The most obvious difference is the steeper inner slope in the simulations with cooling and star formation. Although a state-of-the-art implementation of cooling, feedback, and star formation [121] was used, I should point out that it is not entirely clear how realistic the profiles of these simulated clusters are close to the centre, as a central cD galaxy will contribute substantially to the core density profiles [55, 138]. The core density of stars in the simulations is larger than observed (the simulated clusters seem to suffer to some degree from over-cooling), but some authors (see [50]) argue that part of the discrepancy may be due to stellar mass missed in observations.

Despite the isotropic thermal gas pressure, the density profile in the GAS model is not significantly shallower than in the DM simulation. This can be understood from the fact that gas particles can reduce their angular momentum by collisions (see below), which lets them sink towards the cluster centre more easily. In the GAS_NV simulation, the additional pressure support due to strong turbulence allowed by the lower viscosity reduces the gas density in the inner region of the simulated cluster (see [26] for more detail). However, the impact of the turbulence on the density profiles of real clusters requires further investigation because there the physical viscosity, which is not yet included in the simulations, may or may not limit the amount of turbulence to smaller values.

The effects discussed here can also be seen in Fig. 2.2, which shows the baryonic mass fractions for the GAS and GAS_NV simulations, and the fractions of gas, stars, and the total baryon fraction for the CSF simulation of cluster *g1* as a function of the radius of the sphere around the cluster centre in which it was computed. The baryon fractions of the GAS and CSF simulations are also in good agreement with the results obtained by [50].

Figure 2.3 displays the mass fraction of the particles with specific angular momentum $|\vec{L}|/m < j$ against the threshold j for the cluster *g1* at redshift $z = 0.2975$. Here, $\vec{L}$ and m are the angular momentum and the mass of the cluster particles, respectively. This quantity is plotted for the particles of the simulations with only dark matter and for the gas and dark matter particles of the simulation including adiabatic gas. The angular-momentum profiles of the GAS_NV, CSF, and CSFC simulations, which were not plotted for clarity, are qualitatively similar to the GAS case. Only particles with a distance smaller than $250\,h^{-1}$ kpc from the cluster centre were included. The figure illustrates that the specific angular momentum profiles of the dark-matter particles in the two different simulations are almost identical. However,

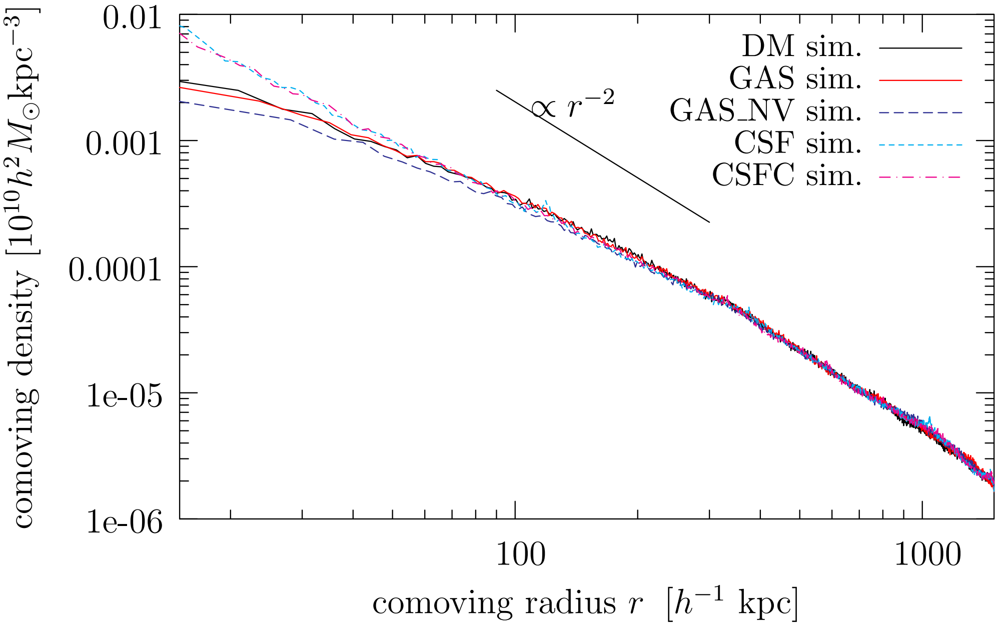

Figure 2.1: Profiles of the total density of cluster *g1* at redshift $z = 0.2975$ for different gas-physical models.

the gas particles typically have a significantly lower specific angular momentum, and the same behaviour is also found in the simulations with cooling and star formation and in the simulations with the new model for artificial viscosity. When studying the time evolution of these profiles, I found that the specific angular momenta of both dark matter and gas particles are boosted towards higher values during mergers. Afterwards, the angular-momentum profile of the dark matter is almost conserved, while the gas relaxes and the particles lose specific angular momentum in collisions. This happens because the cluster halos lack a well-defined rotation axis and the orbital planes of gas clumps have essentially random orientations. Collisions tend to average out differences in orbit orientation and thereby reduce the specific angular momentum of the gas. Therefore, the difference between the specific angular momentum of dark matter and gas increases with each merger. I thus find somewhat larger deviations in large halos, which have on average experienced more mergers. Reducing their spe-

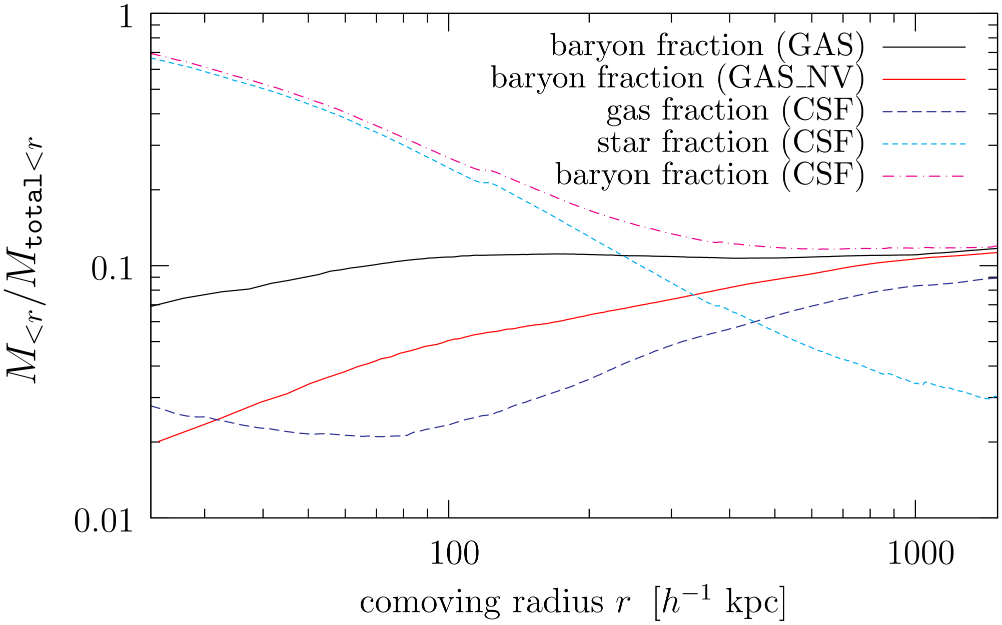

Figure 2.2: Baryonic mass fraction $M_{<r}/M_{\mathtt{total}<r}$ in the GAS and GAS_NV simulation, and mass fractions of gas, stars, and all baryons in the CSF simulation, of cluster *g1* at redshift $z = 0.2975$ as a function of distance r from the cluster centre.

cific angular momenta allows the gas particles to sink more easily towards the cluster centre. A similar behaviour of the specific angular momenta of gas and dark matter was found by [83] and [86] in galaxy-sized halos.

By comparing the monopole to the quadrupole moment in circular shells around the cluster centre, I recover the result obtained by [47], who found that halos are more spherical in simulations with cooling, feedback, and star formation than in dissipationless and adiabatic gas simulations. For example at the scale radius I find 15 percent smaller ratios of quadrupole to monopole moments in projections of simulations with cooling and star formation. I also find more substructure in the form of small clumps in the CSF and CSFC models.

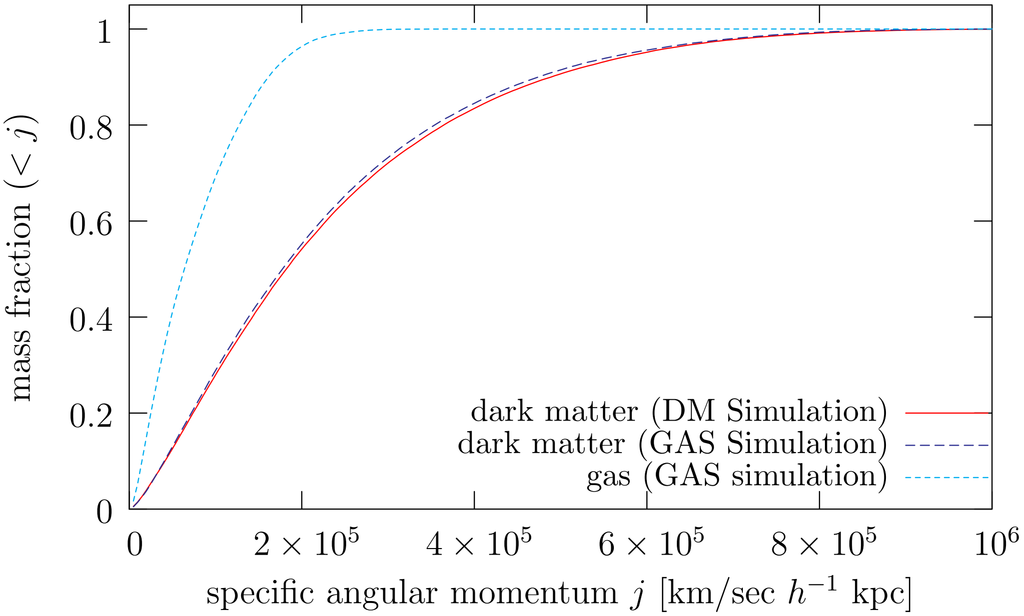

Figure 2.3: Cumulative distributions of the specific angular momentum of the particles contained in the central region of cluster *g1* at $z = 0.2975$, within a radius of $r = 250\,h^{-1}$ kpc.

Chapter 3

Cluster modelling

The modelling of clusters is complicated by the fact that cluster observations yield only projections of physical quantities along the line-of-sight, like for example the X-ray surface brightness as a projection of the X-ray emissivity. Thus one is always confronted with the problem of modelling a three-dimensional object based on two-dimensional data. In order to build such a three-dimensional model one needs to assume some kind of symmetry. Most widely used is the simplest possible assumption, namely that clusters can be described as spherical symmetric objects.

However, the validity of this assumption is questionable considering the halo shapes found in simulations and the frequently observed violent dynamics of clusters. In addition often hydrostatic equilibrium and negligible non-thermal pressure need to be assumed. For example, [39] show that intrinsic variations in clusters limit the accuracy of cluster gas mass estimates to about 10% when using such simple assumptions. Total mass estimates for specific clusters obtained with different methods sometimes differ by a factor of ~ 2 or more (e.g. [136, 91]). The deviations are most likely related to the breakdown of these simple assumptions.

The methods I propose in Sects. 3.5 to 3.8 allow relaxing the symmetry assumption (only axial symmetry with respect to an arbitrarily inclined axis needs to be assumed) and probing hydrostatic equilibrium instead of assuming it. They are also described in [97, 98].

3.1 Spherical symmetric cluster models

Independent of the assumed symmetry one can also distinguish parametric and non-parametric cluster modelling methods. When assuming spherical symmetry the former usually means fitting some kind of profile to the observations.

Still widely used in the analysis of X-ray data is the isothermal beta model [21], in which the gas density is given by

$$\rho = \rho_0 \left(1 + \frac{r^2}{r_c^2}\right)^{-\frac{3}{2}\beta} , \tag{3.1}$$

where r_c is a core radius and ρ_0 is the density in the centre. β is another free parameter which will be discussed below. When considering only continuous bremsstrahlung and assuming isothermality this corresponds to an X-ray surface brightness of

$$S_X = S_{X,0} \left(1 + \frac{r^2}{r_c^2}\right)^{-3\beta+\frac{1}{2}} , \tag{3.2}$$

where $S_{X,0}$ is the central brightness. One can of course easily obtain a similar formula for the Compton y-parameter to analyse thermal SZ data.

The beta model can be motivated by assuming that both the X-ray emitting gas and the cluster galaxies are in hydrostatic equilibrium with the cluster's gravitational field and that both the gas temperature as well as the galaxy velocity dispersion are constant throughout the cluster. In addition it is assumed that the galaxy density is $\propto (1+r^2/r_c^2)^{-3/2}$ [48]. β is then the ratio of the specific kinetic energy of the galaxies to the specific thermal energy of the gas.

The profile given by Eq. (3.2) can be fit to X-ray observations, typically taking an additional term for the instrument background into account. While the observed surface brightnesses are often fit rather well by isothermal beta models, the masses derived from such fits under the assumption of hydrostatic equilibrium are typically too low (e.g. [12]).

More sophisticated analytic, spherically symmetric cluster models have been suggested. For example in [61] it is proposed to use a triple beta model, which is a sum of three terms of the form given in Eq. (3.1), for the gas distribution and a generalised NFW profile for the dark matter distribution. In that work it is suggested to do simultaneous fits to all available data sets (e.g. X-ray, thermal SZ and weak lensing data) directly in the data plane by reprojecting the model halo.

An alternative to fitting parametric models to X-ray or SZ observations is to first use non-parametric methods to deproject the cluster gas distribution under the assumption of spherical symmetry and then derive a mass estimate by assuming hydrostatic equilibrium. The deprojection can be performed with an “onion peeling” technique (see e.g. [51, 30]). Then the cluster is considered to consist of concentric spherical shells each with a specific but constant gas density and temperature. For an X-ray analysis, the observed X-ray counts are binned into circular concentric annuli centred on the cluster centre. Starting from the outermost annulus and taking into account how much of the volume of each shell is projected onto a specific annulus one can “peel the onion” and calculate the X-ray emission observed from each shell. Using X-ray spectral information this allows finding the gas density and temperature in each shell. From that a mass estimate can be derived by either directly applying the hydrostatic equilibrium condition or by fitting a total density profile, e.g. a NFW profile, under the assumption of hydrostatic equilibrium. An “onion peeling” method, that does not rely on X-ray spectral information but jointly analyses X-ray surface brightness and thermal SZ data is proposed in [2].

3.2 Cluster models with less restricting symmetry assumptions

All the cluster reconstruction methods discussed so far use the restricting assumption that clusters can be considered as spherically symmetric systems. Several authors tried to relax this assumption and aimed at a joint analysis of different types of cluster data.

One of the proposed approaches was to base the reconstruction of axisymmetric galaxy clusters on the Fourier slice theorem [141], which states that the Fourier transforms of some source function $\lambda(x, y, z)$ and of its projected image $I(x, y) \equiv \int \lambda(x, y, z) dz$ are related by

$$\hat{\lambda}(k_x, k_y, 0) = \hat{I}(k_x, k_y). \tag{3.3}$$

The assumed axial symmetry also holds for the Fourier transform $\hat{\lambda}(k_x, k_y, k_z)$ of the source function. Using this property and Eq. (3.3) allows finding $\hat{\lambda}(k_x, k_y, k_z)$ for all $\vec{k} = (k_x, k_y, k_z)$ from the Fourier transform of the image, unless the angle between $\vec{k}$ and the symmetry axis is smaller than $\pi/2 - i$, where i is the inclination angle between the line of sight and the symmetry axis. By extrapolating into this "cone of ignorance" and Fourier transforming one can reconstruct the axisymmetric three-dimensional source function. This technique was applied to simulated X-ray, SZ and weak lensing data and shown to perform well [140].

Other approaches that were proposed, include considering perturbations around a spherically symmetric cluster model [27], and adapting parameters of triaxial halo models [52]. Both techniques allow combining different data sets such as X-ray, thermal SZ or weak lensing maps. A method similar to the latter approach was applied to data [25].

An alternative technique based on the iterative Richardson-Lucy deconvolution was suggested by [101] and [102]. It aims at the gravitational potential, assumes only axial symmetry of the main cluster body, avoids extrapolations in Fourier space, and allows to jointly analyse different data sets.

3.3 Lensing reconstruction techniques

Gravitational lensing is, in the thin lens approximation, only sensitive to the projected surface mass density (see Eq. (1.46)). Thus, there is no immediate need to consider a cluster's three-dimensional structure in a lensing analysis. One can start with reconstructing its projected mass distribution and lensing potential.

A standard technique for weak lensing reconstructions is the Kaiser & Squires algorithm ([46], or e.g. [80] for a pedagogical review). It works in Fourier space and uses relations between the Fourier transforms of lensing potential, convergence, and shear. When Fourier transformed Eqs. (1.46), (1.49), and (1.50) take the following forms

$$\hat{\kappa}(\vec{k}) = -\frac{1}{2}(k_1^2 + k_2^2)\hat{\psi}(\vec{k}), \tag{3.4}$$

$$\hat{\gamma_1}(\vec{k}) = -\frac{1}{2}(k_1^2 - k_2^2)\hat{\psi}(\vec{k}), \tag{3.5}$$

$$\hat{\gamma_2}(\vec{k}) = -k_1 k_2 \hat{\psi}(\vec{k}), \tag{3.6}$$

where k_1 and k_2 are the components of $\vec{k}$. Combining these equations one obtains

$$\hat{\kappa}(\vec{k}) = \frac{1}{k_1^2 + k_2^2}\left(k_1^2 - k_2^2, 2k_1 k_2\right) \cdot \begin{pmatrix} \hat{\gamma_1}(\vec{k}) \\ \hat{\gamma_2}(\vec{k}) \end{pmatrix}, \tag{3.7}$$

which relates the convergence to the shear components. However, the latter can be measured. It is convenient to define a complex ellipticity of an image by

$$\epsilon \equiv \epsilon_1 + i\epsilon_2 \equiv \frac{a-b}{a+b} e^{2i\phi}, \tag{3.8}$$

where a, b and ϕ are the images major axis, minor axis and major axis orientation angle, respectively. From the discussion in Sect. 1.4.3 about lensing a circular source, one finds that the ellipticity of a circular source's image is given by

$$\epsilon_1 = \frac{\gamma_1}{1-\kappa}, \tag{3.9}$$

$$\epsilon_2 = \frac{\gamma_2}{1-\kappa}. \tag{3.10}$$

In the weak lensing limit this also holds for the mean ellipticity of the images of a sample of randomly oriented elliptical sources. Then $1-\kappa \approx 1$ is satisfied and one obtains

$$\gamma_1(\vec{\theta}) \approx \langle \epsilon_1(\vec{\theta}) \rangle, \tag{3.11}$$

$$\gamma_2(\vec{\theta}) \approx \langle \epsilon_2(\vec{\theta}) \rangle, \tag{3.12}$$

where $\langle \epsilon_1(\vec{\theta}) \rangle$ and $\langle \epsilon_2(\vec{\theta}) \rangle$ are determined by averaging the measured ellipticities of background galaxies close to $\vec{\theta}$. The size of the region which is averaged over should be chosen such as to obtain a reasonable signal-to-noise ratio.

In practice there are some difficulties in applying the Kaiser & Squires algorithm. The shear can only be measured on a finite field. Thus the involved Fourier transforms can introduce artefacts. In addition there is no unique solution for a convergence κ determined from observed galaxy ellipticities alone. Other solutions can be found by the transformation $\kappa' = \lambda(\kappa - 1) + 1$ and $\gamma' = \lambda\gamma$ for any λ. This is called the "mass sheet degeneracy". Furthermore, the fact that background galaxies have different redshifts is neglected.

In principle Eqs. (3.4) to (3.6) can also be used to reconstruct lensing potentials, however with the same problems due to finite observed fields.

An alternative is to use maximum likelihood or least square methods. They avoid artefacts due to Fourier transforms and allow including strong lensing data in the analysis. The strong lensing data can be used to constrain the position of the critical curve in reconstructions of the lensing potential [20].

3.4 The structure of observed cluster halos - a brief summary

X-ray observations can probe cluster density profiles over a wide radial range, from about ~ 0.001 to 0.7 times the virial radius [54, 95]. The obtained density profiles are typically well fit by the NFW model, while flattened core and singular isothermal profiles usually provide no good fit to the data (e.g. [109]). However, the range of logarithmic inner slopes found in the literature is still rather large, with extreme values of -0.35 [107] and -1.9 [3].

A qualitatively similar picture is obtained by galaxy-galaxy lensing, or more precisely by stacking weak lensing signals around SDSS Luminous Red Galaxies. A NFW model fits the measured shear signal well, while a singular isothermal profile is ruled out [64]. Weak lensing also allows probing the outer slopes of density profiles. For example an outer slope smaller than -2.4, which is consistent with a NFW profile, was found in [49].

By a joint analysis of stellar velocity dispersion in Brightest Cluster Galaxies and strong lensing data an inner logarithmic slope of density profiles of ~ -0.52 was found [106]. However, due to neglecting cluster ellipticity and substructure these estimates may be biased towards flat cusps [70].

The ellipticities of cluster halos were studied by fitting prolate and oblate spheroid halo models, which can be arbitrarily inclined with respect to the line-of-sight, to X-ray surface brightness maps and central SZ temperature decrements [111]. Observations are fit with a mixed population of prolate and oblate models, with prolate models preferred by a factor of ~ 2 to 3. Typical major to minor axis ratios that were found range from roughly 0.3 to 0.7 for prolate and from 0.5 to 0.8 for oblate clusters. However, the symmetry axis of the fitted halo models in these analyses are preferentially aligned with the line-of-sight, which could either be a selection effect or a systematic error.

3.5 A novel method to reconstruct clusters by a joint analysis of X-ray and thermal SZ data

In this section I suggest a novel cluster reconstruction algorithm, which like the algorithms described in [101] and [102] is based on the iterative Richardson-Lucy deconvolution technique [59, 60] . However, instead of aiming at the gravitational potential, which would require assuming a relation between the cluster gas distribution and the gravitational field, like hydrostatic equilibrium, I propose to aim at the cluster gas density and temperature distributions using a joint analysis of X-ray and thermal SZ data. This allows ignoring the commonly used hydrostatic equilibrium assumption for the moment. The proposed technique assumes only axial symmetry of the cluster gas distribution with respect to an arbitrarily inclined symmetry axis and requires no equilibrium assumption other than local thermal equilibrium. The three-dimensional reconstruction algorithm is described in detail below. It is tested using synthetic observations of analytically modelled and numerically simulated galaxy clusters. The impact of realistic observational noise and deviations from axial symmetry on the reconstruction quality is quantified.

From these gas reconstructions, either cumulative mass profiles and reconstructions of the three-dimensional gravitational potential can be obtained by using the hydrostatic equilibrium assumption, or alternatively, hydrostatic equilibrium can be quantitatively probed by comparing cumulative mass profiles obtained in this way to profiles found by an analysis of lensing data. The latter method is described in Sects. 3.6 and 3.8.

An introduction to Richardson-Lucy deconvolution is given in Appendix A.

3.5.1 Deprojection of axisymmetric distributions using Richardson-Lucy deconvolution

As pointed out in [15], Richardson-Lucy deconvolution can be used to reconstruct an inclined axisymmetric three-dimensional distribution of some physical quantity ϕ from a two-dimensional map ψ of its projection along the line-of-sight. In astrophysical applications, ψ will be data obtained from observations, for example the X-ray flux, the lensing potential, or the Sunyaev-Zel'dovich decrement of an approximately axisymmetric galaxy cluster. Because of the assumed symmetry, ϕ can be written as a function of only two cylindrical coordinates R and Z, where I choose the symmetry axis as the Z-axis (see Fig. 3.1). Then, R is the distance from the symmetry axis. The projection along the line-of-sight can be understood as a convolution of $\phi(R, Z)$ with a kernel function $P(x, y|R, Z)$,

$$\psi(x, y) \equiv \int_{-\infty}^{\infty} dz \; \phi(x, y, z) = \int_{0}^{\infty} \pi dR^2 \int_{-\infty}^{\infty} dZ \; \phi(R, Z) \; P(x, y|R, Z). \tag{3.13}$$

The kernel function for a given pair (R, Z) is non-zero only on the ellipse obtained by projecting the ring onto the sky which is defined by R and Z (see Fig. 3.1). It is derived in Appendix A of [15] and can be obtained by considering

$$\int_{-\infty}^{\infty} dz\ \phi(x,y,z) = \int_{-\infty}^{\infty} dz \int_{0}^{\infty} dR^2 \int_{-\infty}^{\infty} dZ\ \phi(R,Z)\, \delta_D(R^2(x,y,z) - R^2)\, \delta_D(Z(x,y,z) - Z), \tag{3.14}$$

where R^2 and Z are integration variables, while $R^2(x,y,z)$ and $Z(x,y,z)$ are given by

$$R^2(x,y,z) = x^2 + (y\cos i - z\sin i)^2, \tag{3.15}$$

$$Z(x,y,z) = y\sin i + z\cos i, \tag{3.16}$$

which is easily found considering Fig. 3.1. Here i is the inclination angle of the symmetry axis, defined as the angle between the symmetry axis and the line-of-sight. Plugging these relations into Eq. (3.14) and performing the z integration yields

$$P(x,y|R,Z) = \frac{\delta[(\frac{y}{\cos i} - Z\tan i)^2 - (R^2 - x^2)]}{\pi\cos i}. \tag{3.17}$$

This kernel satisfies the normalisation condition

$$\int_{-\infty}^{\infty} dx \int_{-\infty}^{\infty} dy\ P(x,y|R,Z) = 1. \tag{3.18}$$

Assuming that the orientation of the symmetry axis is known and that one has a two-dimensional map of the projection ψ, one can reverse the convolution using the iterative Richardson-Lucy deconvolution technique [59, 60] and solve for ϕ as a function of R and Z. Starting with an initial guess ϕ_0 for ϕ and using the Richardson-Lucy iteration scheme, as given by Eqs. (A.9) and (A.10), or in this context by

$$\phi_{n+1}(R,Z) = \phi_n(R,Z) \int_{-\infty}^{\infty} dx \int_{-\infty}^{\infty} dy\ \frac{\psi(x,y)}{\psi_n(x,y)}\ P(x,y|R,Z), \tag{3.19}$$

one can obtain approximations of ϕ with increasing quality. Here, ψ_n is the projection along the line-of-sight of the approximation ϕ_n. If one plugs Eq. (3.17) into Eq. (3.19), performs the y integration, and uses the new coordinate α defined by $x = R\cos\alpha$, one obtains [15]

$$\frac{\phi_{n+1}(R,Z)}{\phi_n(R,Z)} = \int_0^{2\pi} \frac{d\alpha}{2\pi}\, \frac{\psi\,(R\cos\alpha, Z\sin i + R\sin\alpha\cos i)}{\psi_n\,(R\cos\alpha, Z\sin i + R\sin\alpha\cos i)}, \tag{3.20}$$

where the integration follows the ellipse shown in Fig. 3.1.

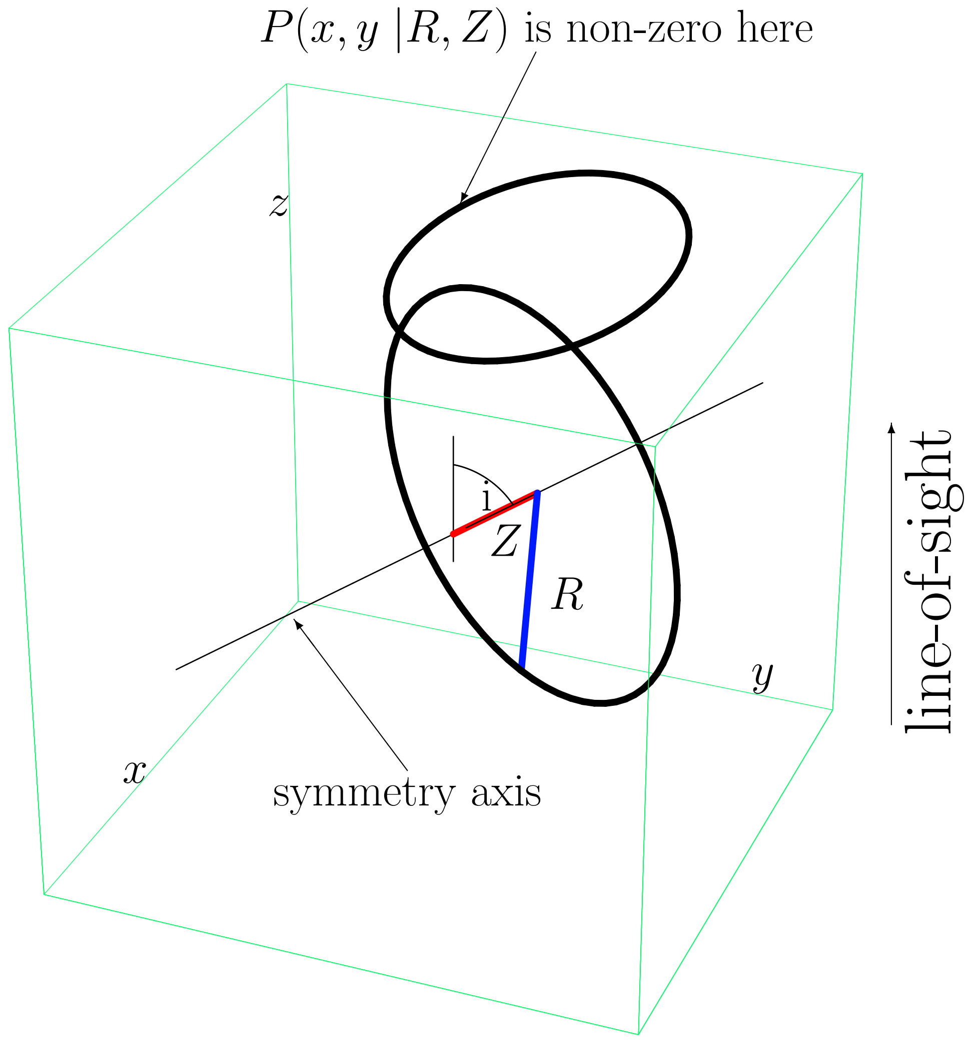

Figure 3.1: Projection of an axisymmetric distribution. The ellipse at the top marks the region where the kernel function corresponding to the projection along the line-of-sight is non-zero for fixed R and Z.

For numerical reconstructions of axisymmetric three-dimensional distributions, the integral in Eq. (3.20) can be replaced by a sum over points, which are distributed along the ellipse and are equally spaced in α. To evaluate the sum, the ratio ψ/ψ_n at these points needs to be computed. I use two grids for the iterative reconstructions, one in x, y-space for ψ and ψ_n, and one in R, Z-space for ϕ_n. First, I project ϕ_n along the line-of-sight on the grid in x, y-space to find ψ_n. I do not use the kernel function for that, but perform a direct summation using a discretised version of the first equality in Eq. (3.13). The projection integral is approximated by a sum over N_z equally spaced points that cover a section of length L_z of the line-of-sight. This section is centred on the z-coordinate of the halo. Then, ψ_n is obtained by

$$\psi_n(x_j, y_k) = \frac{L_z}{N_z} \sum_{l=1}^{N_z} \phi_n(R(x_j, y_k, z_l), Z(x_j, y_k, z_l)), \tag{3.21}$$

where x_j and y_k are the x and y coordinates of the grid point (j, k). The z_l are the z coordinates of the N_z points used for the projection. The function $\phi_n(R(x_j, y_k, z_l), Z(x_j, y_k, z_l))$ is approximated by bilinear interpolation from the values of ϕ_n at neighbouring grid points in R, Z-space. Since I know ψ and have calculated the projection ψ_n of ϕ_n, I can find the ratio ψ/ψ_n at points on the ellipse by bilinear interpolation from neighbouring points of the x, y-space grid. This allows me to approximate the integral in Eq. (3.20) by a sum over N_α points,

$$\frac{\phi_{n+1}(R, Z)}{\phi_n(R, Z)} = \frac{1}{N_\alpha} \sum_{m=1}^{N_\alpha} \frac{\psi\ (R \cos\alpha_m, Z \sin i + R \sin\alpha_m \cos i)}{\psi_n\ (R \cos\alpha_m, Z \sin i + R \sin\alpha_m \cos i)}, \tag{3.22}$$

and find ϕ_{n+1} at all points of the R, Z-space grid, which completes the iteration step. Here $\alpha_m = 2\pi m/N_\alpha$.

3.5.2 Boundary effects, artefacts, and regularisation

There is, however, a problem. Assume that L_z corresponds to the height of the box shown in Fig. 3.1, and that the area covered by the map of ψ corresponds to its top surface. To calculate ψ_{n+1} there, I have to know ϕ_{n+1} everywhere in the box. But for finding ϕ_{n+1} close to the corners of the box, one has to evaluate Eq. (3.22) along ellipses that do not fit into the top surface of the box. This means that some of the points one has to sum over lie outside the map of ψ and ψ_n. As suggested by [101], I replace ψ/ψ_n for those points by its value at the closest point at the perimeter of the map. This leads to some artefacts in the reconstruction of ϕ for large R and Z, but yields very good results in the central region, which I am most interested in.

To start the iteration, I have to choose a guess or prior ϕ_0. I adopt the simplest choice of a flat or constant prior and set its value so as to reproduce the average value $\langle\psi\rangle$ of the map ψ, namely $\phi_0 = \langle\psi\rangle/L_z$.

The algorithm described above can be used to reconstruct axisymmetric three-dimensional distributions from two-dimensional maps of its projection along the line-of-sight. However, it runs into problems for strongly peaked distributions such as the X-ray emissivity of a galaxy cluster. In order to illustrate that, I reconstructed the X-ray emissivity from an X-ray surface brightness map, which I obtained by projecting the emissivity of an analytically modelled, axisymmetric cluster halo. The halo model is discussed in Sect. 3.5.4. For the projection, I chose an inclination angle of $i = 70°$ and performed a reconstruction with a rather large number of $n = 30$ iterations. In the left panel of Fig. 3.2, the ratio between the reconstructed and the original X-ray emissivity is shown. One can clearly see spike-shaped artefacts of the reconstruction. The angle between these spikes and the symmetry axis is equal to the inclination angle i. This means that the ellipses corresponding to R and Z values of points in the spikes pass directly through the halo centre in the map of ψ.

Richardson-Lucy deconvolution reproduces large scale structures quickly, while it converges slowly to small scale structures such as the peak at the halo centre (see [59, 60] or Appendix A). This means that, when starting with a flat prior, ψ/ψ_n can be quite large close to the centre even after several iterations. Thus, when I evaluate (3.22) for points further out whose ellipses pass through the halo centre, I find ratios of $\phi_{n+1}(R,Z)/\phi_n(R,Z)$ which are too high, and the spike-shaped artefacts form. They appear already after the first few iterations and are very stable. In the left panel of Fig. 3.2, I show them after 30 iterations, and it would take several hundred more iterations until they slowly disappear.

To prevent the formation of such artefacts, I use a regularisation scheme. First, I calculate an average $\langle\psi/\psi_n\rangle$ for the points used in the sum in Eq. (3.22), which is defined by

$$\langle\psi/\psi_n\rangle(R,Z) \equiv \frac{1}{N_\alpha}\sum_{m=1}^{N_\alpha} \min\left(\frac{\psi\,(R\cos\alpha_m,\; Z\sin i + R\sin\alpha_m\cos i)}{\psi_n(R\cos\alpha_m,\; Z\sin i + R\sin\alpha_m\cos i)}, 10\right). \tag{3.23}$$

Then I set

$$c_n(R,Z) \equiv \frac{1}{N_\alpha}\sum_{m=1}^{N_\alpha} \min\left(\frac{\psi\,(R\cos\alpha_m,\; Z\sin i + R\sin\alpha_m\cos i)}{\psi_n(R\cos\alpha_m,\; Z\sin i + R\sin\alpha_m\cos i)}, 1.2\,\langle\psi/\psi_n\rangle(R,Z)\right), \tag{3.24}$$

and use

$$\frac{\phi_{n+1}(R,Z)}{\phi_n(R,Z)} = \max\left(\,c_n(R,Z),\; 0.25\,\right), \tag{3.25}$$

to calculate $\phi_{n+1}(R,Z)$. This regularisation of the iteration scheme suppresses the formation of spike-shaped artefacts. It limits the impact of sharp peaks in ψ on points that are far away from the corresponding peaks in ϕ by using an upper limit for ψ/ψ_n in Eqs. (3.23) and (3.24). The effectiveness of the regularisation scheme is not very sensitive to the exact numerical values of the upper limits, which I chose by trial and error, as long as it suppresses sharp peaks and is not too restrictive to allow convergence in a reasonable number of iterations. The lower limit for the correction factor in Eq. (3.25) is introduced just to make sure that ϕ_{n+1} does not change its sign or become very small in the first few iteration steps, which could potentially cause problems later.

I repeated the reconstruction of the X-ray emissivity using this regularisation. In the right panel of Fig. 3.2, the ratio of the reconstructed to the original emissivity after 30 iterations is shown. The spikes that are present in the left panel have almost disappeared. The ratio is close to unity everywhere in the region shown, except very near the halo centre where grid resolution and the slow convergence to small-scale structures becomes a problem. Apart from that, the deprojection works very well. The errors are usually smaller than 1%.

So far, I have assumed that the orientation of the symmetry axis is known beforehand. In reality, when applying this algorithm to observations, this will not be the case. However, the orientation of the symmetry axis in the plane of the sky can be directly inferred from the map ψ. Methods to find its inclination angle i are discussed in Sect. 3.5.8.

3.5.3 Reconstruction of ICM density and temperature from combined X-ray and thermal Sunyaev-Zel'dovich effect observations

So far, I have discussed how to reconstruct a single three-dimensional distribution of a physical quantity from a single two-dimensional map of its projection along the line-of-sight. However, one can obtain additional information by combining different data sets [102, 101]. Here, I propose to reconstruct several physical quantities at the same time by combining different observations that depend on these quantities. Specifically, I will show how to obtain three-dimensional distributions of the density and temperature of the ICM in axisymmetric cluster halos by combining X-ray and thermal Sunyaev-Zel'dovich effect observations.

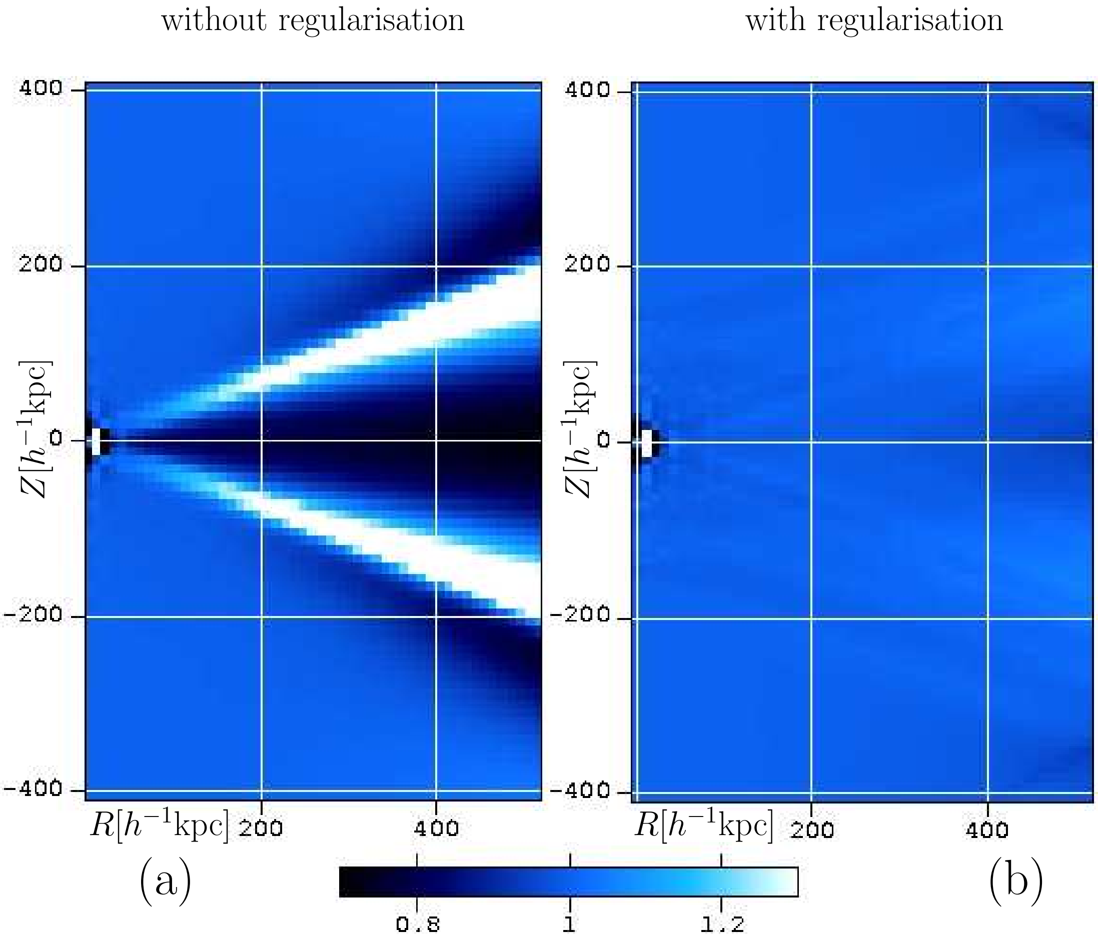

Figure 3.2: Ratio of the reconstructed to the original X-ray emissivity after $n = 30$ iteration steps, ϕ_n/ϕ. The halo centre is at the centre left of each plot. Panel (a) shows the ratio obtained without regularisation. One can clearly see the spike-shaped artefacts of the reconstruction. Panel (b) shows the ratio for the reconstruction including the regularisation. It is close to unity everywhere except very close to the centre, where the algorithm converges slowly and grid resolution becomes a problem.

The X-ray surface brightness is proportional to

$$\psi_{\text{X-ray}} \equiv \int dz\,\rho^2\,\lambda(T,\mathcal{Z}), \tag{3.26}$$

where ρ and T are the gas density and temperature, respectively. The integral extends along the line-of-sight. The cooling function $\lambda(T,\mathcal{Z})$ depends on the gas temperature and the metallicity $\mathcal{Z}$. Here $\mathcal{Z}$ is assumed to be constant. The thermal SZ temperature decrement or increment is proportional to the Compton y-parameter given in Eq. (1.36). For fully ionised gas with constant metallicity, this is also proportional to ψ_{SZ} defined by

$$\psi_{\text{SZ}} \equiv \int dz\,\rho\,T. \tag{3.27}$$

Both $\psi_{\text{X-ray}}$ and ψ_{SZ} can be obtained from observations.

For reconstructing the ICM temperature and density, I start from some initial guess $\rho_0(R,Z)$ and $T_0(R,Z)$. In analogy to Eq. (3.21), I use discrete approximations of Eqs. (3.26) and (3.27),

$$\begin{aligned}\psi_{\text{X-ray},\,n}(x_j,y_k) &= \frac{L_z}{N_z}\sum_{l=1}^{N_z}\rho_n^2(R(x_j,y_k,z_l),Z(x_j,y_k,z_l))\\ &\quad\times\ \lambda(T(R(x_j,y_k,z_l),Z(x_j,y_k,z_l)),\mathcal{Z}), \qquad (3.28)\\ \psi_{\text{SZ},\,n}(x_j,y_k) &= \frac{L_z}{N_z}\sum_{l=1}^{N_z}\rho_n(R(x_j,y_k,z_l),Z(x_j,y_k,z_l))\\ &\quad\times\ T(R(x_j,y_k,z_l),Z(x_j,y_k,z_l)), \qquad (3.29)\end{aligned}$$

to obtain $\psi_{\text{X-ray},\,0}$ and $\psi_{\text{SZ},\,0}$. In analogy to Eq. (3.22), I define

$$c_{\text{X-ray},n}(R,Z) = \frac{1}{N_\alpha}\sum_{m=1}^{N_\alpha}\frac{\psi_{\text{X-ray}}(R\cos\alpha_m, Z\sin i + R\sin\alpha_m\cos i)}{\psi_{\text{X-ray},n}(R\cos\alpha_m, Z\sin i + R\sin\alpha_m\cos i)}, \tag{3.30}$$

$$c_{\text{SZ},\,n}(R,Z) = \frac{1}{N_\alpha}\sum_{m=1}^{N_\alpha}\frac{\psi_{\text{SZ}}(R\cos\alpha_m, Z\sin i + R\sin\alpha_m\cos i)}{\psi_{\text{SZ},\,n}(R\cos\alpha_m, Z\sin i + R\sin\alpha_m\cos i)}, \tag{3.31}$$

and propose the iteration scheme

$$\frac{\rho_{n+1}^2\,\lambda(T_{n+1},\mathcal{Z})}{\rho_n^2\,\lambda(T_n,\mathcal{Z})} = c_{\text{X-ray},\,n}, \tag{3.32}$$

$$\frac{\rho_{n+1}T_{n+1}}{\rho_n T_n} = c_{\text{SZ},\,n}. \tag{3.33}$$

In order to find the next iterative approximation of density and temperature, Eqs. (3.32) and (3.33) need to be solved for ρ_{n+1} and T_{n+1}. To include line emission in the cooling function, one can tabulate $\lambda(T_n,\mathcal{Z})$, e.g. using the software package XSPEC [4] for a specific emission model and metallicity, and solve the equations above numerically. A simple analytic solution can be found if continuous thermal bremsstrahlung is assumed. Then

$$\lambda(T,\mathcal{Z}) \propto \sqrt{T}, \tag{3.34}$$

so that one obtains

$$\rho_{n+1} = \frac{c_{\text{X-ray},\,n}^{2/3}}{c_{\text{SZ},\,n}^{1/3}}\rho_n, \tag{3.35}$$

$$T_{n+1} = \frac{c_{\text{SZ},\,n}^{4/3}}{c_{\text{X-ray},\,n}^{2/3}}T_n. \tag{3.36}$$

from Eqs. (3.32) and (3.33). In fact these relations can be used even when including line emission as small errors introduced by using them are corrected in subsequent iteration steps as long as the correct cooling function is used in Eq. (3.28). The number of iterations needed to achieve a good reconstructions is also not significantly affected.

Note that for evaluating Eq. (3.30) and (3.31), the regularisation introduced in Sect. 3.5.2 is used. Its effectiveness, even when applied to different kinds of data, depends only weakly on the exact values of the numerical constants in Eqs. (3.23) to (3.25). Thus I use these equations with the numerical values given there for both the X-ray and SZ data. Again, for points that lie outside the map of $\psi_{\text{X-ray}}$ and ψ_{SZ}, the ratios $\psi_{\text{X-ray}}/\psi_{\text{X-ray},\,n}$ and $\psi_{\text{SZ}}/\psi_{\text{SZ},\,n}$ are approximated by their values at the closest point at the perimeter of the map. In the next sections, I shall apply this deprojection algorithm to axisymmetric analytic halos and to numerically simulated cluster halos, and discuss its performance.

3.5.4 Deprojection of analytic halos based on noise-free synthetic observations

In this section and in Sect. 3.5.5, I use a NFW-like gas density profile to test the deprojection algorithm for axisymmetric, analytic halos. However, for the deprojection to be non-trivial, I prefer to have ellipsoidal iso-density surfaces. It is thus assumed that the density of the ICM is a function of

$$r \equiv \sqrt{\frac{R^2}{R_s^2} + \frac{Z^2}{Z_s^2}}, \tag{3.37}$$

where R_s is a scaling radius perpendicular to the symmetry axis, and Z_s is a scaling distance along the axis. The density of the hot cluster gas is then taken to be

$$\rho = \frac{4\rho_s}{(\epsilon_r + r)(1+r)^2}, \tag{3.38}$$

which differs from the NFW form not only by its ellipsoidal shape but also by the small constant $\epsilon_r = 0.001$ introduced to ensure that the density does not diverge for $r \to 0$. Such a divergence would cause problems in numerical calculations. For the gas temperature I use a phenomenological description that roughly corresponds to the temperature profiles found in the simulated cluster sample described in Sect. 2.3. Namely, I set

$$T = T_{\max} r^{-0.2\gamma(r)}, \tag{3.39}$$

where $\gamma(r) = \tanh(3(r-1))$ is -1 for $r \ll 1$ and $+1$ for $r \gg 1$. The values of the parameters $\rho_s = 7.5 \times 10^4 h^{-1} M_\odot/(h^{-1}\text{kpc})^3$, $Z_s = 500 h^{-1}\text{kpc}$, $R_s = 300 h^{-1}\text{kpc}$, and

$T_{\max} = 12$keV, which I use correspond to the gas component of a massive galaxy cluster. Here, h is the reduced Hubble constant, which is set to 0.7.

Having chosen an inclination angle i, I project the analytic halo described above on a 128×128 grid with a sidelength of $1.5h^{-1}$Mpc and obtain the X-ray and Sunyaev-Zel'dovich effect maps, $\psi_{\text{X-ray}}$ and ψ_{SZ}. I use the algorithm discussed in Sect. 3.5.3 with these maps to reconstruct the gas density and temperature. For simplicity I consider here and in Sects. 3.5.5, 3.5.6, 3.5.7, and 3.5.8 only continuous thermal bremsstrahlung for the X-ray emission. More realistic synthetic X-ray observations that also include line emission are used in Sects. 3.7 and 3.8. In Fig. 3.3, the results of the deprojection are compared with the original density and temperature of the analytic halo. An inclination angle $i = 70°$ and $n = 20$ iterations were used. The inclination was assumed to be known in performing the deprojection. The left and right panels show the density and temperature ratios, ρ_n/ρ and T_n/T, respectively. The star-like pattern of the plots maps the ranges of R and Z coordinates occurring in the simulation box used for the reconstruction (see Fig. 3.1). In the central region of the cluster, the reconstruction works very well. Errors are of the order of 1%. Despite the regularisation, one can still see some remains of the spike-shaped artefacts discussed in Sect. 3.5.2. For large R or Z values, close to the star-shaped boundary of the plots, the quality of the reconstruction decreases. This is not at all surprising because the ellipses along which Eqs. (3.30) and (3.31) must be evaluated to reconstruct density and temperature at those points lie mostly outside of the maps of $\psi_{\text{X-ray}}$ and ψ_{SZ}.

Note that the quality of the reconstruction also depends on the inclination of the halo's symmetry axis. Of course, best results are achieved when the symmetry axis is perpendicular to the line-of-sight. Then the assumption of axial symmetry contains the most information. If, on the other hand, the symmetry axis is parallel to the line-of-sight, the axial symmetry just corresponds to the circular symmetry

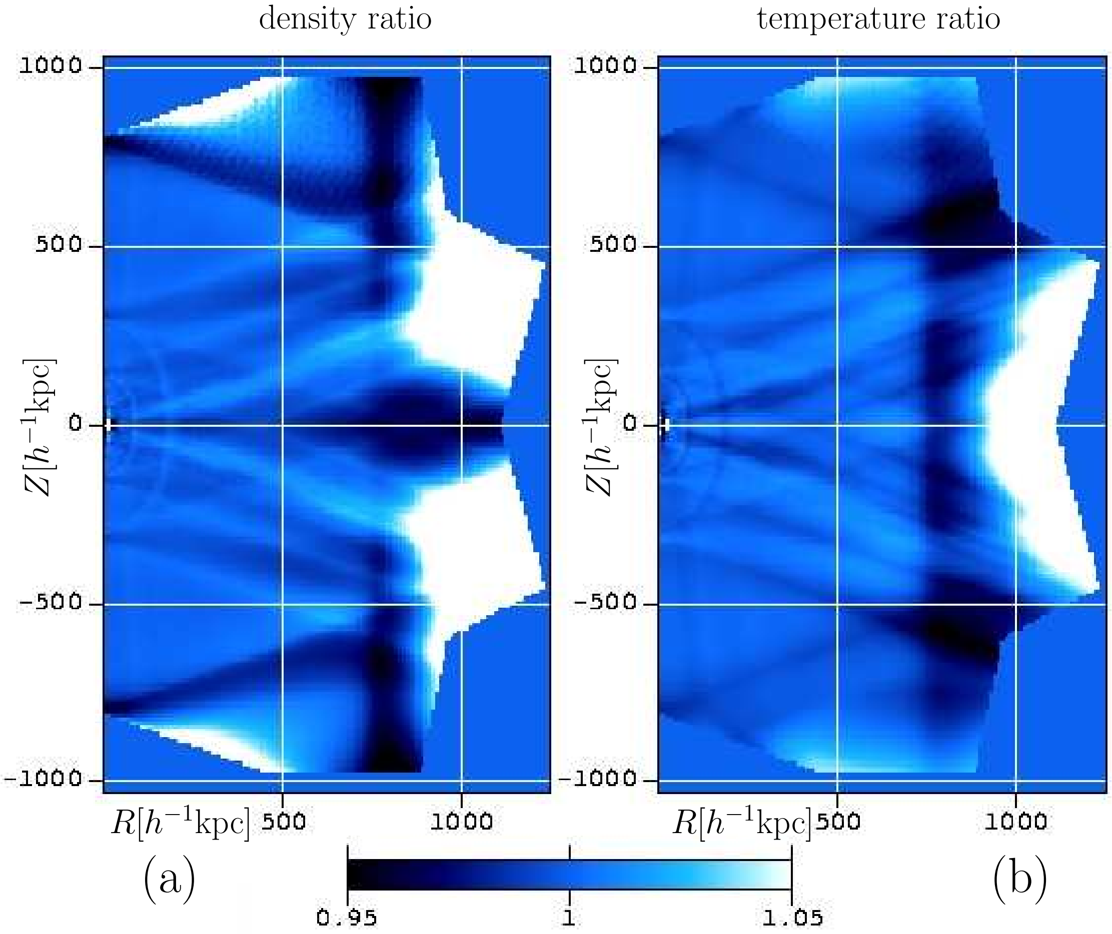

Figure 3.3: Ratio of the reconstructed to the original density and temperature for the analytic halo after $n = 20$ iterations. An inclination angle of $i = 70°$ was chosen and assumed to be known in performing the reconstruction. Panel (a) shows the density ratio ρ_n/ρ and panel (b) the temperature ratio T_n/T. In the central region, the errors are of the order of 1%. I plot the ratios for all R and Z values possible within the box used for the reconstruction (see Fig. 3.1). This causes the star-like shape of the perimeter of the plot in the R, Z plane. Close to that boundary, at large R or Z values, the ratios can significantly differ from unity. This is, however, expected because the ellipses used in the reconstruction of ρ and T at those points lie mostly outside the maps of $\psi_{\text{X-ray}}$ and ψ_{SZ}.

of the maps $\psi_{\text{X-ray}}$ and ψ_{SZ} and does not yield any useful additional information. Figure 3.4 illustrates this inclination dependence. It shows the volume-weighted root mean square (RMS) relative errors of the reconstructed gas density and temperature, computed within a sphere of radius $500h^{-1}$kpc around the halo centre. Again, the knowledge of the inclination angle i was used in the deprojection. An accuracy of 1% or better is achieved for about two thirds of the analytic halos in a randomly oriented sample. However, halos that happen to have a very small inclination angle are necessarily poorly reconstructed.

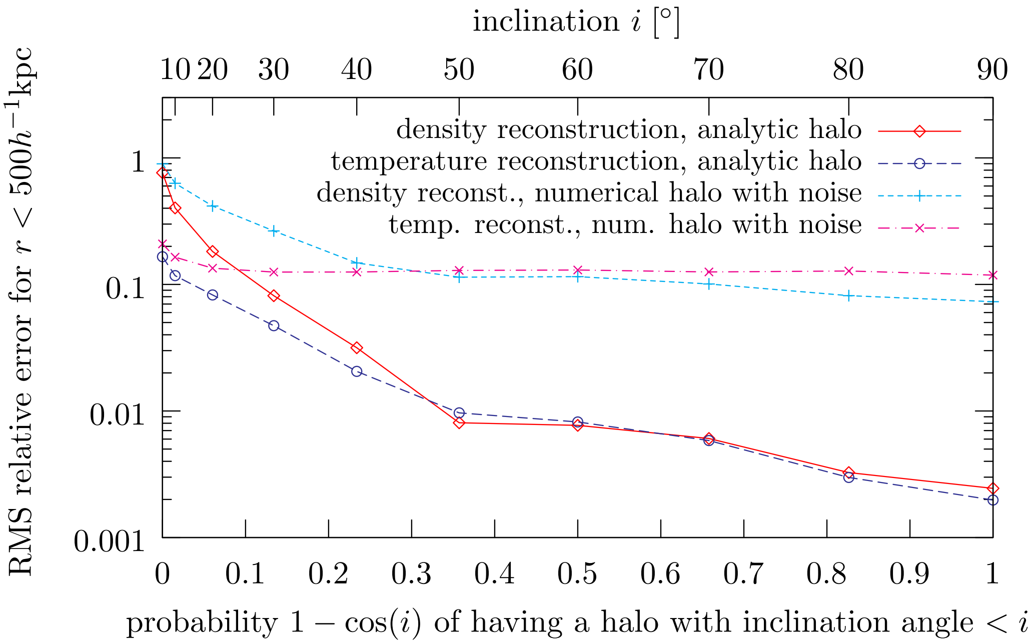

Figure 3.4: Dependence of the quality of the deprojection on the inclination of the symmetry axis. For the analytic halo, which was deprojected as described above, I show the volume-weighted RMS relative errors $(\rho_n - \rho)/\rho$ and $(T_n - T)/T$ as functions of the inclination angle i after $n = 20$ iterations. I also show the same errors after $n = 5$ iterations for reconstructions of a numerical halo from maps with observational noise. A detailed description of these reconstructions is given in Sects. 3.5.6 and 3.5.7. The averages of the errors were computed within a sphere of radius $500h^{-1}$kpc around the halo centre. The quantity $1 - \cos(i)$ shown on the abscissa is chosen such as to have a flat number-density distribution for randomly oriented halos. The inclination angle i was assumed to be known in performing the deprojection.

3.5.5 Deprojection of analytic halos based on noisy synthetic observations

So far I have not considered noise that will be present in any real X-ray or Sunyaev-Zel'dovich effect observation. I will now discuss the impact it has on the reconstruction of ICM densities and temperatures.

The noise in X-ray observations is modelled as follows. First, I calculate for each pixel (j,k) of the halo's X-ray map $\psi_{\text{X-ray}}$ the number of photons $\langle N_{\gamma\, j,k}\rangle$ expected from bremsstrahlung, which is proportional to $\langle N_{\gamma\, j,k}\rangle \sim \sum_{l=1}^{N_Z} \mathrm{E}_1(\frac{E_{\min}}{k_B T})\frac{\rho^2}{\sqrt{T}}$, where the sum extends along the line-of-sight represented by the pixel (j,k), and E_1 is the exponential integral function. $E_{\min}$ is a lower energy cutoff which is necessary because the number of photons emitted is infrared divergent. I choose $E_{\min} = 0.23\,\mathrm{keV}$, which is a reasonable lower limit for the photons from galaxy clusters observed in current X-ray experiments. Next, I normalise the numbers of expected photons such that they sum up to $\sum_{j,k}\langle N_{\gamma\, j,k}\rangle = 10^4$ on the entire map. For each pixel (j,k), I then set the actual number of photon counts $N_{\gamma\, j,k}$ to a value drawn from a Poisson distribution with expectation value $\langle N_{\gamma\, j,k}\rangle$. Then noise is added to the map $\psi_{\text{X-ray}}$ by multiplying $\psi_{\text{X-ray}\, j,k}$ with $N_{\gamma\, j,k}/\langle N_{\gamma\, j,k}\rangle$ for all pixels.

For the Sunyaev-Zel'dovich effect, I add noise corresponding to future ALMA Band 3 observations [19]. In Band 3 (84 to 116 GHz) and in its compact configuration, ALMA will be able to achieve a temperature sensitivity of 50μK at a spatial resolution of ~ 3 arcsec in about four hours of observation. At an assumed halo redshift of 0.3, this resolution corresponds to the angular size chosen for the pixels of the map ψ_{SZ}. I convert the temperature sensitivity cited above to an error $\sigma_{\psi_{\text{SZ}}}$ of ψ_{SZ}. Then, for each pixel, I add noise obtained from a normal distribution with standard deviation $\sigma_{\psi_{\text{SZ}}}$ to ψ_{SZ}.

Richardson-Lucy deconvolution has the nice property of approximating large-scale features quickly and small-scale noise slowly. Yet, it turns out that smoothing the noisy maps $\psi_{\text{X-ray}}$ and ψ_{SZ} before using them in the deprojection improves the results considerably. I use the following smoothing scheme. For the X-ray observations, I assume that in addition to the map $\psi_{\text{X-ray}}$ I also know the photon counts $N_{\gamma\, j,k}$ for all pixels. I then calculate for each pixel (j,k) a radius $h_{\text{SML}j,k}$ so that I have a fixed number of 100 photons inside a circle with radius $h_{\text{SML}j,k}$ around that pixel. After that I redistribute the value $\psi_{\text{X-ray}\, j,k}$ of each pixel on the grid with a smoothing kernel of width $h_{\text{SML}j,k}$ centred on that pixel. This greatly reduces the fluctuations in the map $\psi_{\text{X-ray}}$ caused by photon noise. In the following I will call this first step of the smoothing scheme "photon-noise smoothing".

For the smoothing kernel, I take the line-of-sight projection of the cubic spline SPH kernel $W(r, h_{\text{SML}})$ defined in Appendix A of [123]. It is well suited for this purpose and allows using the same routine for smoothing here and for projecting the numerical SPH halos used in this work. For axisymmetric halos, the projection should be symmetric about the projected axis. However, the symmetry is broken here by noise. I restore it before performing the deprojection. Since the grid is oriented such that it is parallel to and centred on the projected symmetry axis, I can do that by replacing $\psi_{\text{X-ray}\, j,k}$ and $\psi_{\text{X-ray}\, N_{\text{grid}}-j,k}$ by their arithmetic mean. Here, $N_{\text{grid}} = 128$ is the dimension of the grid. ψ_{SZ} is symmetrised in the same way.

In some of the reconstructions I use one more smoothing operation on $\psi_{\text{X-ray}}$ and ψ_{SZ} to further reduce fluctuations caused by noise. In numerically simulated halos, which I will discuss later, this will also suppress the effect of subclumps. Since I do not want to smooth out the peaks in the halo core, I choose a smoothing length h_{SML} that depends on the distance r from the halo (or map) centre, namely $h_{\text{SML}} = h_{\text{SML, max}}(1 - W(r, r_{\max})/W(0, r_{\max}))$. It is zero in the centre of the map and continually increases to $h_{\text{SML}} = 375h^{-1}$kpc at a radius equal to $r_{\max} = 750h^{-1}$kpc or larger. A comparison of reconstructions for which different smoothing lengths were used showed that this yields smallest RMS errors. Once I have calculated h_{SML} for each pixel, I smooth the maps of $\psi_{\text{X-ray}}$ and ψ_{SZ} with the projection of the SPH smoothing kernel mentioned above and with the position-dependent smoothing length h_{SML}. Note that roughly 80% of a pixel's value is redistributed within a circle of radius $h_{\text{SML}}/2$. I refer to this second step of the smoothing scheme as "radius-dependent smoothing".

After degrading the analytic halo with noise and applying the smoothing scheme described above, I perform the iterative deprojection. The results after $n = 5$ iterations are shown in Fig. 3.5. An inclination of $i = 70°$ was chosen and assumed to be known in the deprojection. Both "photon-noise" and "radius-dependent" smoothing were applied. Again, the left panel shows the ratio of the reconstructed to the original density, and the right panel the corresponding temperature ratio. Average errors in the central region are of the order of 5% to 10%. As expected, further outside, where the signal-to-noise ratio becomes small and the ellipses used for the reconstruction lie mostly outside the maps of $\psi_{\text{X-ray}}$ and ψ_{SZ}, the errors are substantially larger. Note that at locations where I obtain a too low density, I usually find a too high temperature and vice versa. This happens because the algorithm minimises the deviations of the reconstructed from the original X-ray and thermal SZ effect maps.

In Fig. 3.6, I show density and temperature profiles of the original analytic halo, of the halo reconstructed from maps without observational noise, and of the halo reconstructed from smoothed maps which contain observational noise. The reconstructed halos are the same as shown in Figs. 3.3 and 3.5. Without noise, both the temperature and the density profiles are reproduced very well. With noise, I can still reproduce density profiles with an accuracy of a few percent. The errors in the temperature profile are somewhat larger. Deviations are mainly caused by the noise,

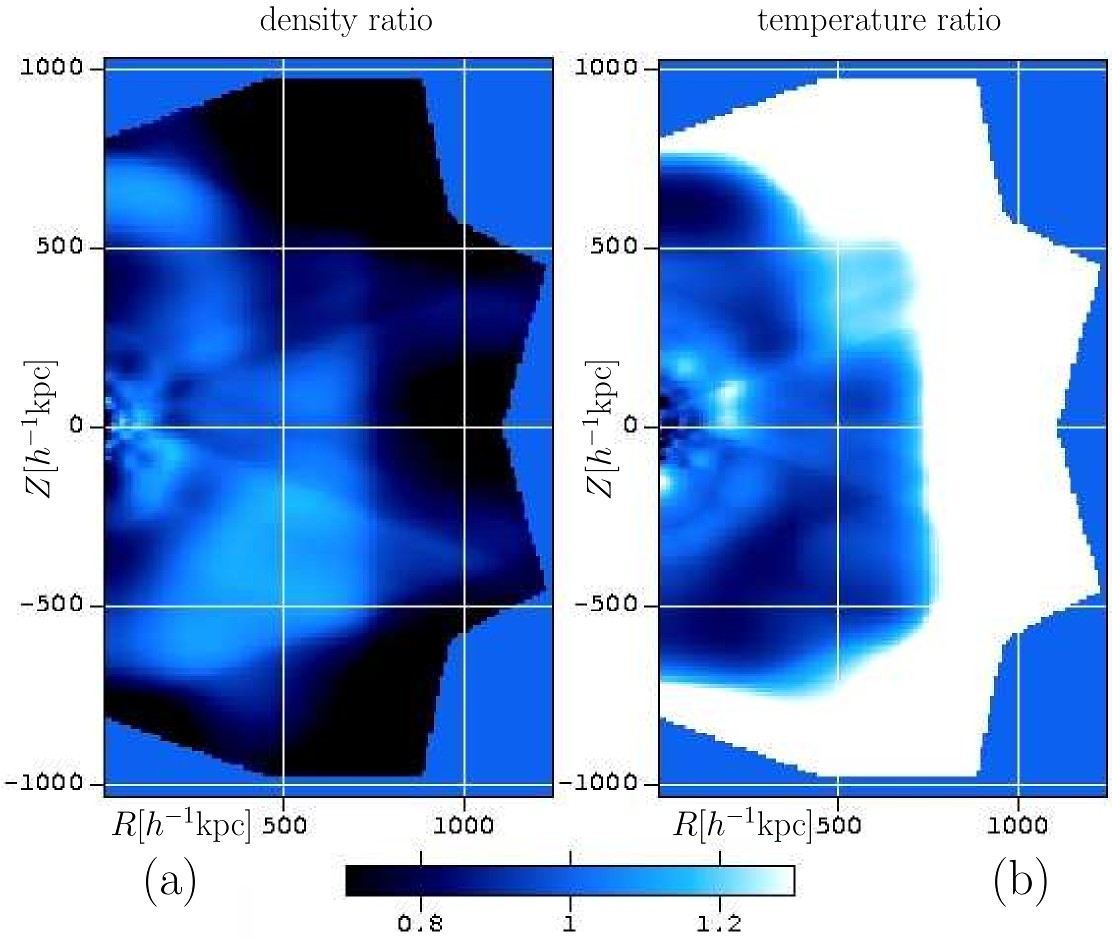

Figure 3.5: Ratio of the reconstructed to the original density and temperature for the analytic halo with observational noise after $n = 5$ iterations. An inclination of $i = 70°$ was chosen and assumed to be known in performing the reconstruction. “Photon-noise” and “radius-dependent” smoothing were applied. Panel (a) shows the density ratio ρ_n/ρ, and panel (b) the temperature ratio T_n/T. In the central region, the errors are of the order of 5% to 10%.

but some are also artefacts of the smoothing scheme I applied. Especially the too high temperature near $\sim 200\,h^{-1}$ kpc and the too low temperature near $\sim 400\,h^{-1}$ kpc are a consequence of "radius-dependent smoothing". On the other hand, without such smoothing the errors in the density and temperature reconstructions would approximately double.

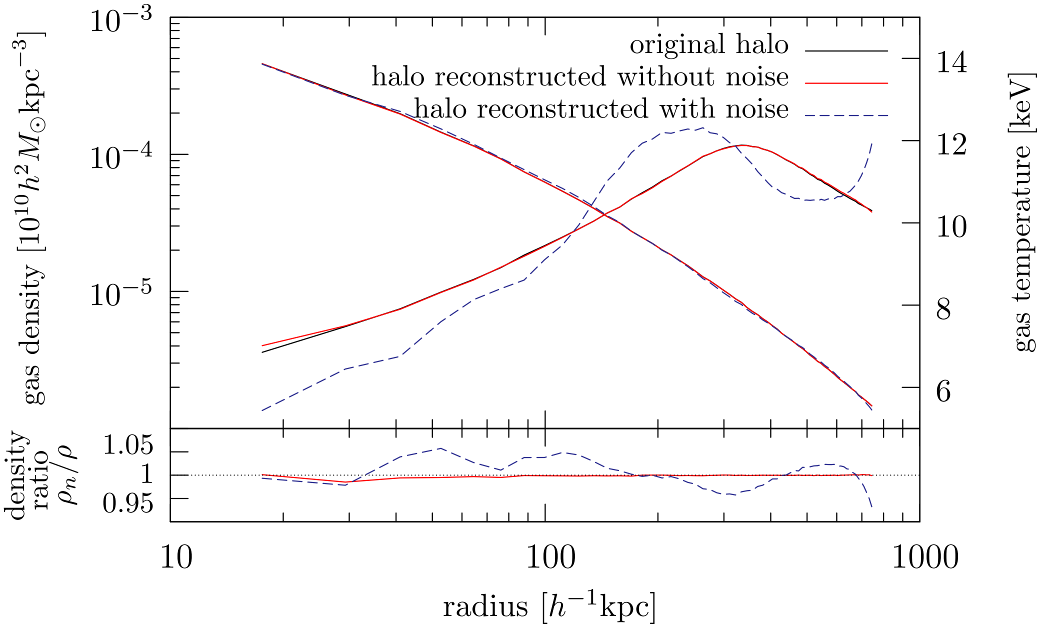

Figure 3.6: Density and temperature profiles of the original and the reconstructed analytic halos. The upper panel shows the density (falling curves, left axis) and the temperature profiles (rising curves, right axis) of the original analytic halo, the halo reconstructed without observational noise (and without any smoothing), and the halo reconstructed from maps with observational noise to which the complete smoothing scheme was applied. The lower panel shows the profile of the ratio of the reconstructed density ρ_n to the original density ρ. The number of iterations used was $n = 20$ in the case without noise and $n = 5$ in the case with noise. An inclination of $i = 70°$ was chosen and assumed to be known in the reconstruction.

3.5.6 Deprojection of numerical clusters based on noise-free synthetic observations

So far, I have demonstrated the performance of the algorithm with axisymmetric analytic halos. I was able to reconstruct their three-dimensional density and temperature distributions from synthetic X-ray and thermal SZ effect observations. Real galaxy clusters, however, are hardly perfectly axisymmetric. I will study in this section whether they nonetheless allow accurate density and temperature reconstructions with the deprojection algorithm proposed in Sect. 3.5.3. I use a sample of four numerically simulated galaxy clusters to investigate into this question, namely the GAS runs of clusters *g1*, *g8*, *g51* and *g72*. As described in Sect. 2.3, these simulations follow the dynamics of dark matter as well as the adiabatic evolution of the ICM, but they ignore radiative cooling.

My deprojection algorithm requires a symmetry axis, which real and numerically simulated clusters do not generally have. I thus need to choose an axis around which the numerical clusters have at least a high degree of symmetry. I do this by calculating the inertial tensor of the cluster gas inside a sphere of radius $500h^{-1}$ kpc around the cluster centre and finding its eigenvectors $\vec{v}_1, \vec{v}_2, \vec{v}_3$ and eigenvalues $e_1 \geq e_2 \geq e_3$. I choose the symmetry axis through the cluster centre and parallel to the eigenvector $\vec{v}_3$ with the smallest eigenvalue if $e_1/e_2 \leq e_2/e_3$, or parallel to the eigenvector $\vec{v}_1$ with the largest eigenvalue otherwise. This means that, if two eigenvalues are very similar, I choose the axis parallel to the eigenvector corresponding to the third eigenvalue.

Having chosen a fiducial "symmetry" axis and a line-of-sight, I can produce synthetic maps of X-ray and Sunyaev-Zel'dovich effect observations. For that purpose, I use the simulated clusters at a redshift of $z = 0.3$ and project them along the line-of-sight. At $z = 0.3$, the cluster sample spans a mass range between 8×10^{14}

and $1.8 \times 10^{15}\, h^{-1} M_{\odot}$. Only continuous thermal bremsstrahlung is considered for the X-ray emission in this and the next section.

For now, I do not add any observational noise to the maps. However, the clusters contain substructures which break axial symmetry and lead to artefacts in the density and temperature reconstructions. Thus, depending on the amount of substructure present in a cluster, it may still be favourable to use "radius-dependent smoothing" on the X-ray and Sunyaev-Zel'dovich effect maps prior to reconstruction. In Figs. 3.7 and 3.8, I show the results of the deprojection without any smoothing, and using "radius-dependent smoothing".

The density reconstruction in the central region reaches an accuracy of about 10% in both cases. For the temperature reconstruction and the density reconstruction at large r, I obtain somewhat better results without smoothing for this rather symmetric cluster. Note, however, the hyperbolically shaped artefacts in Fig. 3.7 which are produced by substructure clumps in absence of smoothing. They appear at those R and Z values which correspond to the line-of-sight passing through such a clump. The spike-shaped artefacts discussed in Sect. 3.5.2 were a special case of the artefacts found here. For most of the hyperbolae in the left panel of Fig. 3.7, one can also see the position of the clump that produced it in darker colours. The hyperbolae pass right through them.

As one can see in Fig. 3.8, "radius-dependent smoothing" removes the hyperbolic artefacts. The subclumps, however, still appear in darker colours in the density ratio map, which means that the reconstructed density there is too low. However, this is entirely expected and inevitable, because they violate axial symmetry and thus cannot be faithfully reconstructed with this deprojection technique. By smoothing, I essentially remove the subclumps from the maps and reconstruct the density and temperature of the main halo without them.

Unfortunately, “radius-dependent smoothing” also affects the density and temperature profiles. This can be seen in the “rings” around the halo centre in the right panel of Fig. 3.8. It is further illustrated in Fig. 3.10, which shows the density and temperature profiles of the original cluster *g51*, after deprojection without noise but with “radius-dependent smoothing”, and after deprojection without noise and without smoothing. For $r > 300h^{-1}$kpc, the reconstruction without smoothing yields more accurate density and temperature profiles. In addition, the profiles for deprojections from maps including observational noise are shown. They will be discussed in the next section.

Reconstructions along different lines-of-sight and of the three other clusters in the sample gave similar results. For the most asymmetric halo, the errors were larger by factors of 1.5 to 2 compared to the reconstruction of *g51* presented above. One can thus conclude that, although clusters are not strictly axisymmetric and contain substructure, it is possible to apply the deprojection method proposed in Sect. 3.5.3 and successfully reconstruct three-dimensional density and temperature distributions of the cluster gas.

3.5.7 Deprojection of numerical clusters based on noisy synthetic observations

In Sect. 3.5.5, I studied the impact of observational noise in the X-ray and Sunyaev-Zel’dovich effect maps on the quality of the density and temperature reconstruction. I will now do the same for the numerically simulated cluster halos using the same noise model, namely Poisson noise corresponding to 10^4 observed source photons for the X-ray maps and a noise level expected for a four-hour ALMA Band 3 observation for the Sunyaev-Zel’dovich effect maps. I also use the smoothing scheme described

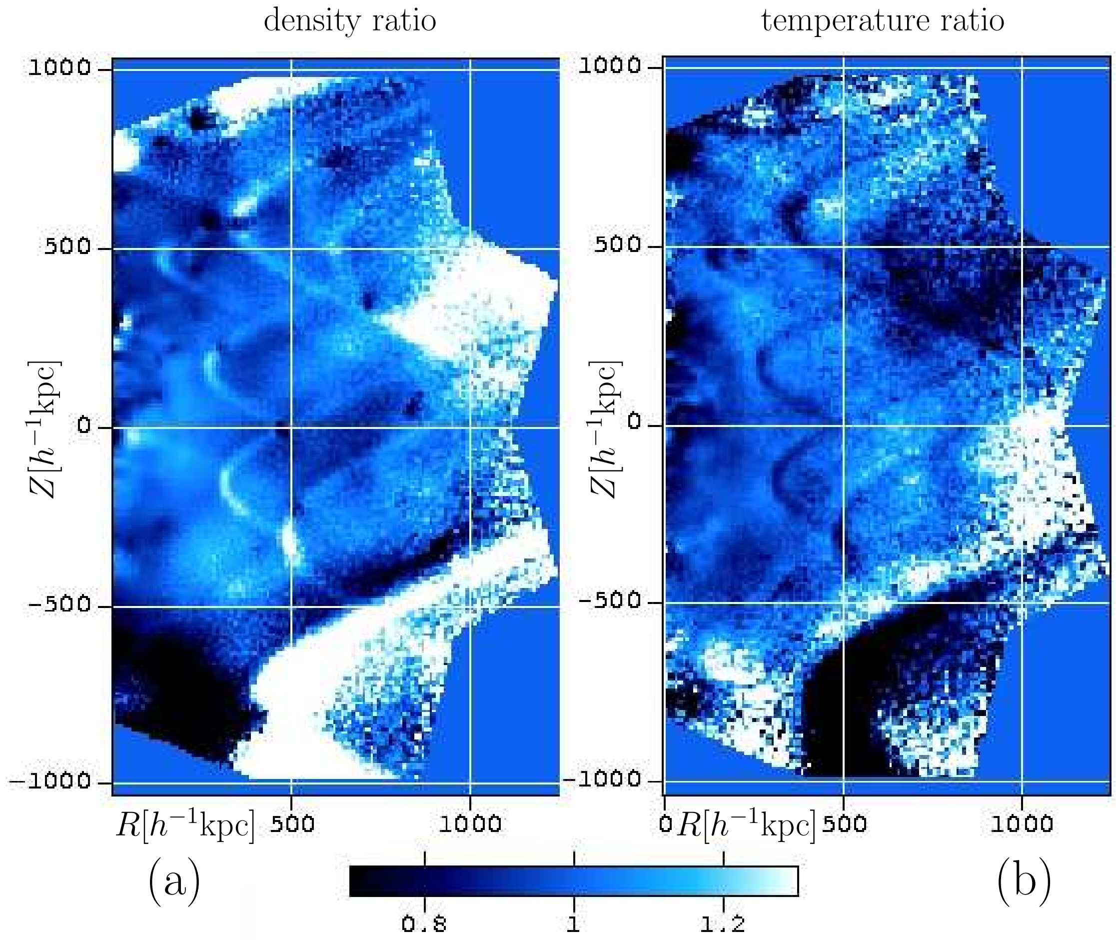

Figure 3.7: Reconstruction of the simulated cluster *g51* without noise and smoothing. The ratios of the reconstructed to the original density and temperature are shown. The deprojection was done with $n = 5$ iterations. An inclination angle of $i = 68°$ between the line-of-sight and the principal inertial axis of the cluster gas was chosen and assumed to be known in the reconstruction. Panel (a) shows the density ratio ρ_n/ρ and panel (b) the temperature ratio T_n/T. In the central region, the errors are of the order of 10%.

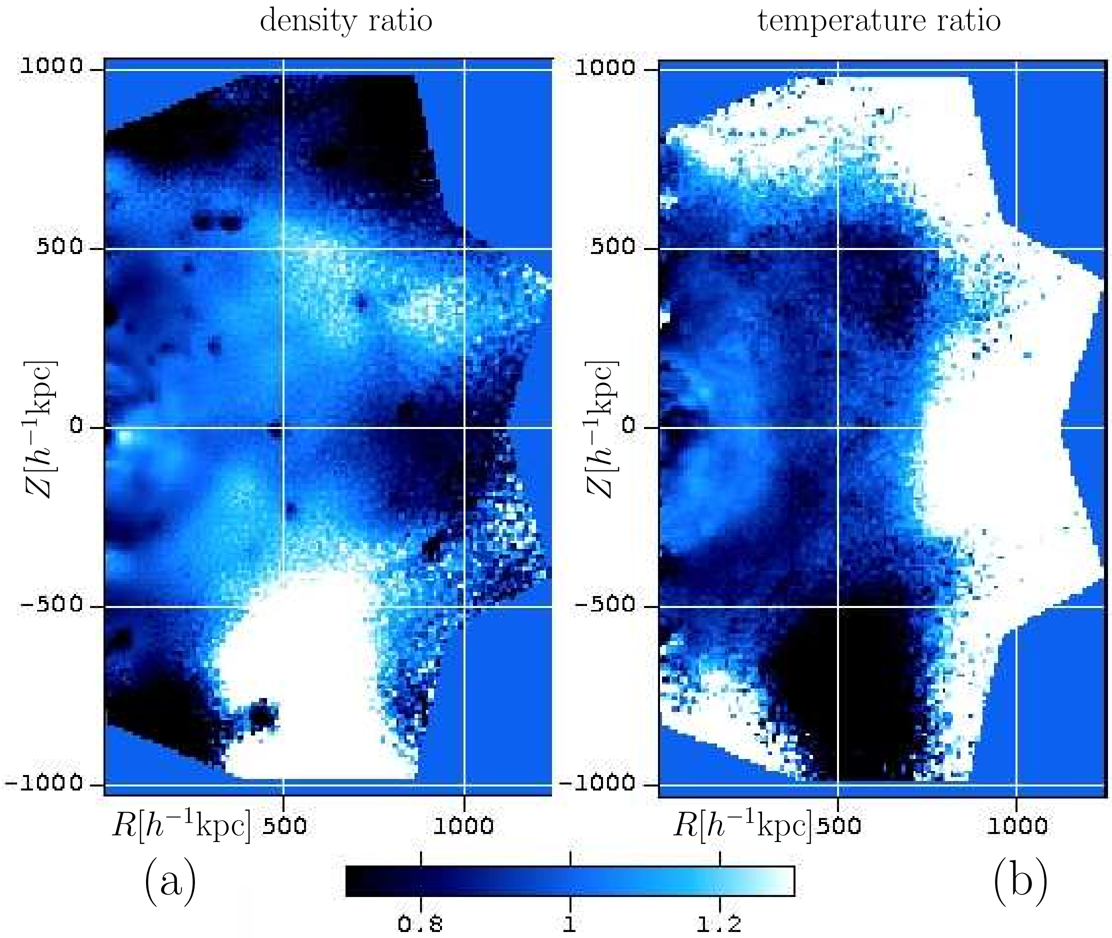

Figure 3.8: Reconstruction of the simulated cluster *g51* without noise but with "radius-dependent smoothing". The ratios of the reconstructed to the original density and temperature are shown. The deprojection was done with $n = 5$ iterations. An inclination angle of $i = 68°$ between the line-of-sight and the principal inertial axis of the cluster gas was chosen and assumed to be known in the reconstruction. Panel (a) shows the density ratio ρ_n/ρ and panel (b) the temperature ratio T_n/T. In the central region, the errors are of the order of 10%.

there.

I show the results of the reconstruction in Fig. 3.9. Again, the left panel shows the ratio of the reconstructed to the original density, and the right panel the corresponding temperature ratio. In the central region an accuracy of about 15% is achieved. Without "radius-dependent smoothing", errors would be larger by roughly a factor of 1.5 or even more next to the halo centre. However, if one is mainly interested in density and temperature profiles it may still be favourable to leave the "radius-dependent smoothing" step away. Although the errors are larger without "radius-dependent smoothing", they are less biased with respect to the distance from the halo centre and cancel better when averaging over spherical shells around it, especially at large radii. Thus depending on the quantity one is finally interested in or the context in which the reconstructions are used, different amounts of smoothing may yield best results. Figure 3.10 shows the profiles obtained with and without "radius-dependent smoothing".

I still need to discuss when the iteration used in the density and temperature reconstructions should best be stopped. Figure 3.11 illustrates the dependence of the quality of the reconstruction on the number of iterations used. More precisely, it shows the relative volume-weighted RMS error of the density reconstruction within $r = 500\,h^{-1}$ kpc as a function of the number of iterations and for different deprojection schemes, namely for the deprojections of the analytic halo and the numerically simulated cluster *g51* discussed above and shown in Figs. 3.3, 3.5, 3.8, and 3.9 after $n = 20$ or $n = 5$ iterations. The quality of the reconstruction improves quickly during the first roughly five iterations (first ten for the analytic halo without noise) and then levels off. In addition, I show the quality of the reconstruction of *g51* from maps with noise but without using "radius-dependent smoothing". In this case, small-scale noise in the maps is not sufficiently suppressed. The best reconstruction is found after five

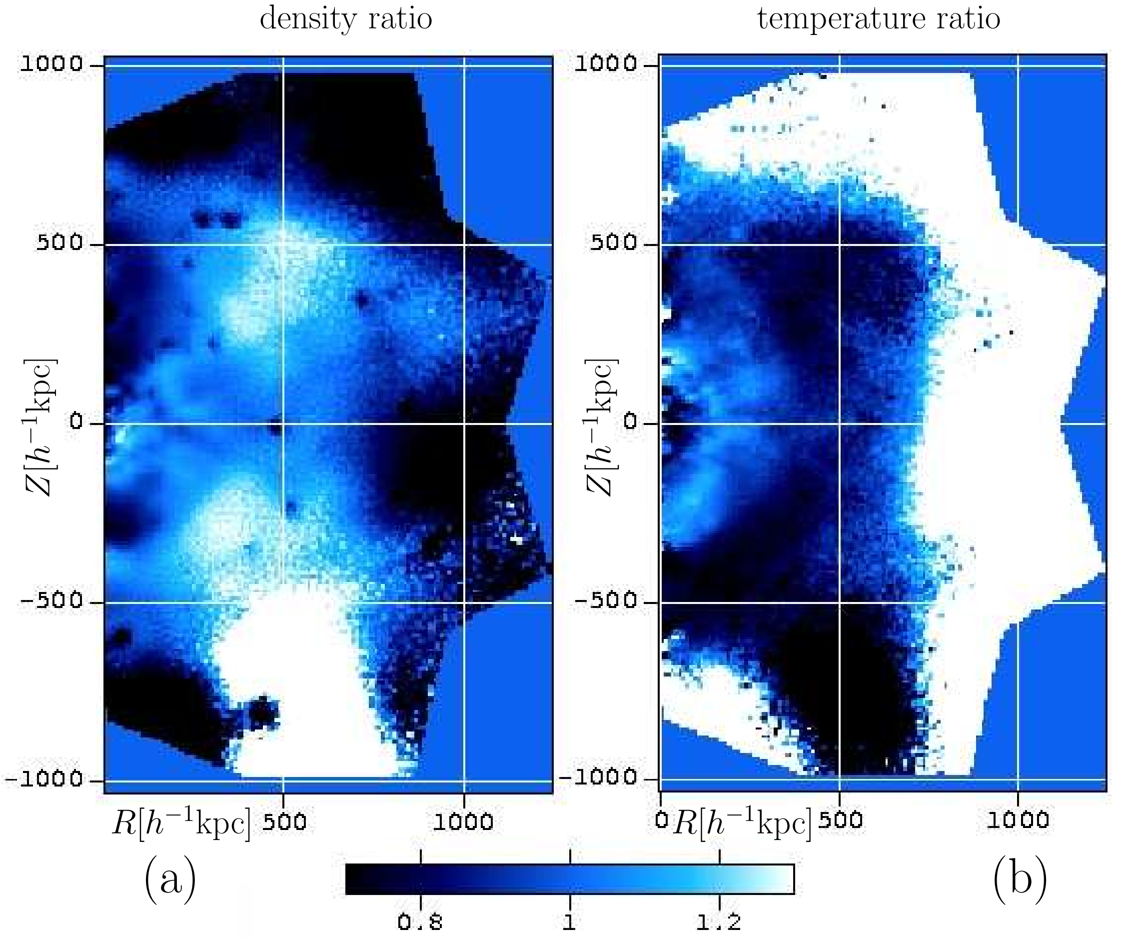

Figure 3.9: Reconstruction of the simulated cluster *g51* with noise and and the complete smoothing scheme applied. The ratios of the reconstructed to the original density and temperature are shown. The deprojection was done with $n = 5$ iterations. An inclination angle of $i \approx 68°$ between the line-of-sight and the principal inertial axis of the cluster gas was chosen and assumed to be known in the reconstruction. Panel (a) shows the density ratio ρ_n/ρ and panel (b) the temperature ratio T_n/T. In the central region, the errors are of the order of 15%.

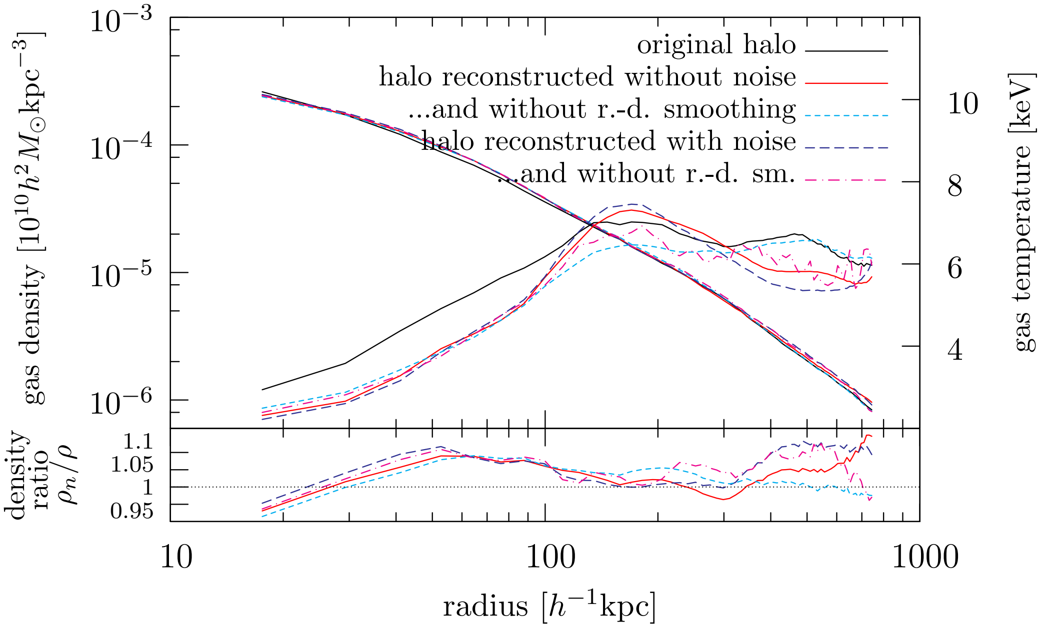

Figure 3.10: Gas density and temperature profiles of the original and the reconstructed cluster *g51*. The upper panel shows the density profiles (falling curves, left axis) and the temperature profiles (rising curves, right axis) of the original cluster, the cluster reconstructed without observational noise but with "radius-dependent smoothing", reconstructed without observational noise and without any smoothing, reconstructed from maps with observational noise and the complete smoothing scheme applied, and reconstructed from maps with observational noise but without "radius-dependent smoothing". The lower panel shows the profile of the ratio of the reconstructed density ρ_n to the original density ρ. The number of iterations used was $n = 5$ in all cases. An inclination angle of $i \approx 68°$ was chosen and assumed to be known in the reconstruction.

iterations. Then, the quality decreases again because the algorithm starts to approximate small-scale noise. Thus, unless a halo is very smooth and axisymmetric, such as the analytic halo without noise, I find that the quality of the reconstruction does not significantly increase after $n = 5$ iterations and may even decrease if small scale fluctuations due to noise are not efficiently suppressed. Thus, I conclude that it is favourable to use this number of iterations for the deprojection of simulated and real galaxy clusters. Alternatively, one could control the reproduction of small-scale fluctuations with a formal regularisation scheme, such as provided by maximum-entropy methods.

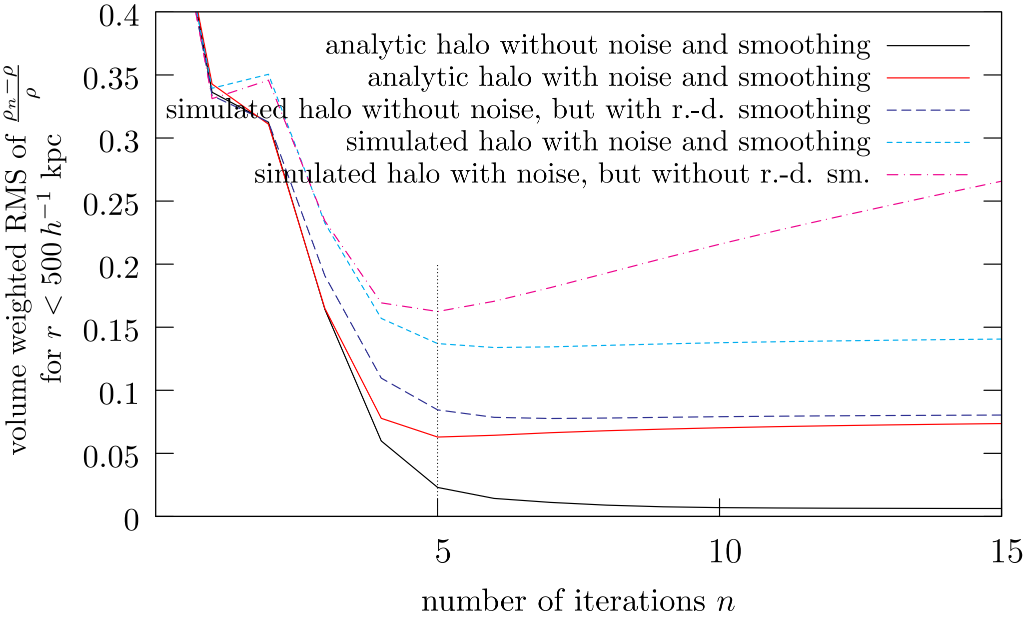

Figure 3.11: Dependence of the quality of the density reconstruction on the number of iterations used. The volume-weighted relative RMS error $\frac{\rho_n-\rho}{\rho}$ within a sphere with $r = 500\,h^{-1}$ kpc radius is shown for different deprojections of the analytic halo model and of the numerically simulated cluster *g51*. The figure legend explains which halo, whether or not noise, and what kind of smoothing were used for the different reconstructions shown. Note that "photon-noise smoothing" of the X-ray maps is always and only used for maps with noise.

3.5.8 Finding inclination angles

In all deprojections of analytic and numerical clusters presented above, I have assumed that the orientation of the "symmetry" axis is known beforehand. In reality, when applying this algorithm to observations, this will typically not be the case. However, its orientation in the plane of the sky can be directly inferred from the observations. So the problem reduces to finding the axis' inclination angle.

In principle one could reconstruct a cluster using a fixed number N_{it} of iterations and assuming different values for the inclination angle i. Then, one would compare the X-ray and SZ maps corresponding to the cluster reconstructions, namely $\psi_{\text{X-ray},N_{\text{it}}}$ and $\psi_{\text{SZ},N_{\text{it}}}$, to the original observed maps $\psi_{\text{X-ray}}$ and ψ_{SZ} and find the value of i for which they fit best. This value could for example be found by minimising

$$\sum_{j,k} \frac{(\psi(x_j, y_k) - \psi_{N_{\text{it}}}(x_j, y_k))^2}{\psi^2(x_j, y_k)}, \tag{3.40}$$

where ψ is either $\psi_{\text{X-ray}}$ or ψ_{SZ}, or one uses a linear combination of both sums. Depending on the shape of the distribution one wants to reconstruct, it may be favourable to sum only over points in the central region of the map.

I did this for the analytic halo model and for the sample of numerically simulated clusters and used different inclination angles i' for projecting these halos to obtain the original maps on which the reconstructions are based on. However, the minima in the penalty function are not well defined. They are very broad and not always centred on $i = i'$. Even for the analytic halo without observational noise, it is hardly possible to find the correct axis inclination in this way. As one can see from Eqs. (3.30) and (3.31), the iterative corrections of the deprojection algorithm are determined from the deviations of the X-ray and Sunyaev-Zel'dovich effect maps, and the deviations are thereby minimised. Unfortunately, this still works remarkably well when choosing a wrong inclination angle $i \neq i'$ for the deprojection. Thus the X-ray and Sunyaev-Zel'dovich effect maps are still reproduced well in this case, although the errors of the density and temperature reconstructions increase significantly.

I tried to limit the ability of the deprojection algorithm to reproduce observations well even when the inclination angle is wrong by reducing its degrees of freedom. For doing so, I used a variant of the algorithm that only reconstructs the density and uses a constant but adjustable temperature. This of course also limits the accuracy of the reconstruction for the correct inclination angle. Thus, the results of comparing the reconstructed X-ray and Sunyaev-Zel'dovich effect maps to the original ones for finding the inclination angle were not significantly better.

On the other hand, leaving the deprojection algorithm as described in Sect. 3.5.3, but using additional independent information for finding the inclination angle of the halo, seems to be more promising. For the deprojection, I use maps of the X-ray surface brightness of clusters, but so far I do not use any spectral information from the X-ray observations. In Figs. 3.12 and 3.13, I assume that in addition to the X-ray surface brightness maps I also have maps of the emission-weighted temperature T_{ew}. I reconstruct the analytic halo and the numerically simulated cluster *g51* from X-ray flux and Sunyaev-Zel'dovich effect maps as above, but then compare the original emission-weighted temperature map to the one obtained by reprojecting the reconstructed halos. I repeated this for different inclination angles i', chosen for projecting the original maps, and i, chosen in the reconstruction.

Note, however, when applying this method to real galaxy clusters and projected temperature maps obtained by X-ray spectral fitting of single temperature emission models to observations, it may be favourable to use a more sophisticated projected temperature definition, such as the spectroscopic-like temperature, instead of the emission-weighted temperature [67].

Figure 3.12 shows the RMS relative error of the reconstructed emission-weighted temperature maps for the analytic halo without and with noise. $N_{\mathrm{it}} = 20$ and no smoothing were used without noise, and $N_{\mathrm{it}} = 5$ and the complete smoothing scheme were used with noise. The RMS error was computed within a radius of $500\,h^{-1}$ kpc around the map centre and is shown for inclinations of $i' = 40^\circ$ and $i' = 70^\circ$ of the original halo. As desired, the minima of the error curves are at the correct locations $i \approx i'$.

Note that the curves are only shown for i between 0° and 90° because $\psi_{\text{X-ray}}$ and ψ_{SZ} and hence the whole deprojection algorithm is insensitive to what is the front and what is the back side of the cluster. One thus gets the same reconstruction and the same errors for deprojections which adopt inclination angles i and $180° - i$. There is no way to distinguish these cases from the X-ray, thermal Sunyaev-Zel'dovich effect and temperature maps alone. The error curves are thus symmetric about $i = 90°$. Also note that for the halo with noise, I added observational noise only to the X-ray flux maps and Sunyaev-Zel'dovich effect maps that were used for the reconstruction, but not to the T_{ew} maps which I use for finding the inclination angle. I do not mimic observational noise in the temperature maps because it can only be realistically modelled when considering instrument response and line emission. In addition to the error curves of the temperature maps, I also show the volume-weighted, relative RMS errors of the density reconstructions in the central $500\,h^{-1}$ kpc in Fig. 3.12. As expected, the reconstruction works best for $i \approx i'$.

Figure 3.13 shows similar quantities as Fig. 3.12, but for the numerically simulated cluster halo *g51*. Original halo inclinations were set to $i' = 40°$ and $i' = 68°$, and $N_{\mathrm{it}} = 5$ iterations were used. The error curves are shown for the simulated halo without observational noise and using "radius-dependent smoothing", and including observational noise and using the complete smoothing scheme. No noise was added to the emission-weighted temperature maps. The relative RMS T_{ew} error was computed within a circle of radius $200\,h^{-1}$ kpc around the map centre, while the density reconstruction errors were again determined within the central $500\,h^{-1}$ kpc. Also for this numerical halo the errors are smallest for $i \approx i'$.

For halos with an original inclination $i' \ll 90°$ or $i' \gg 90°$ and for the analytic halos without noise, the minima of the error curves for the emission-weighted temperature and the density reconstructions are well defined. Thus the quality of the reconstruction of such halos depends strongly on using the correct inclination $i = i'$ assumed in the deprojection. However, in such cases, the inclination angle is better constrained by the emission-weighted temperature maps. On the other hand, if the "symmetry" axis of the original halo is almost perpendicular to the line-of-sight, the minima of the error curves are usually broad, and finding the precise inclination $i = i'$ for the reconstruction becomes less important. This can also be understood from the fact that deviations are symmetric around $i = 90^\circ$. For example, the halo with an inclination of $i' = 68^\circ$ shown in Fig. 3.13 should exhibit minima at $i = i' = 68^\circ$ and at $i = 180^\circ - i' = 112^\circ$ and a maximum in between. However, because these three extremal points are close to each other, they start merging into one broad minimum. Note that the emission-weighted temperature maps can constrain the inclination angle in both cases to values where the errors of the reconstruction are close to their minima.

The accuracy of inclination-angle estimates could most likely be further improved by using other independent information in addition to the temperature maps, such as data from weak and strong-lensing observations.

3.5.9 The cluster gas as a probe of the gravitational potential

To find the gravitational potential of a cluster from the distribution of the cluster gas I assume that the gas is in hydrostatic equilibrium. Then the gas density ρ, the gas pressure p and the gravitational potential ϕ satisfy

$$\vec{\nabla}\phi = -\frac{\vec{\nabla}p}{\rho}. \tag{3.41}$$

In principle this equation can be used to find the gravitational potential of relaxed clusters from three-dimensional reconstructions of their intra-cluster medium. However due to deviations from hydrostatic equilibrium, and the presence of observational noise and cluster substructure violating axial symmetry, the curl of $-\vec{\nabla}p/\rho$ will not vanish exactly for the reconstructed gas distributions. Thus one cannot obtain a

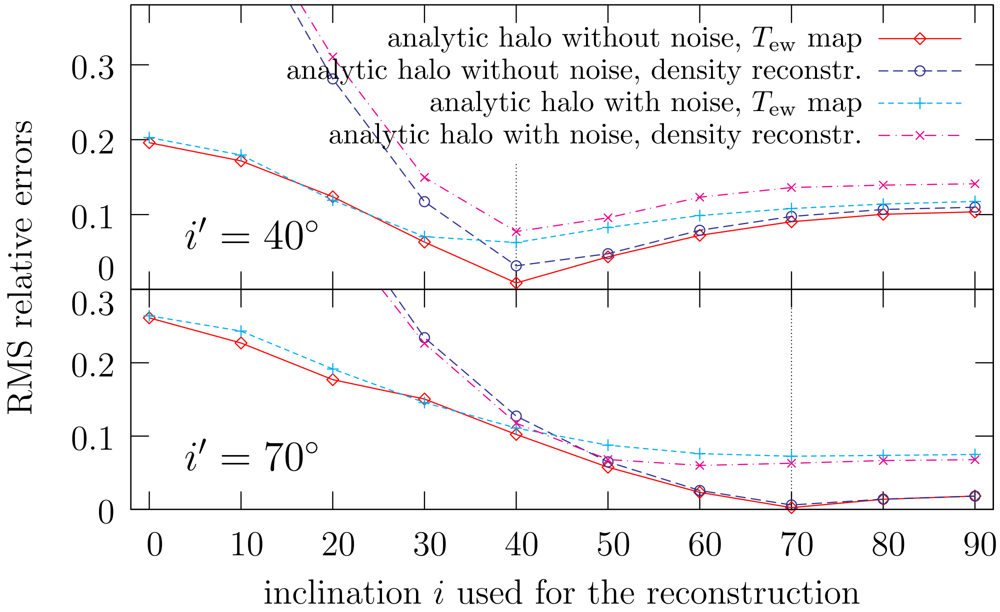

Figure 3.12: Accuracy of emission-weighted temperature $T_{\rm ew}$ maps and densities of reconstructed analytic halos. The deprojections started from maps obtained by projecting the analytic halo along a line-of-sight with inclination angles of $i' = 40°$ and $i' = 70°$. Inclination angles i between 0° and 90° were used for the reconstruction. As expected, the best reconstructions are obtained for $i \approx i'$. The errors are shown for deprojections from maps without observational noise and from smoothed maps with observational noise, and were averaged within a region of radius $500\,h^{-1}$ kpc around the map or halo centre.

unique solution for ϕ directly from Eq. (3.41).

To get a unique solution I first derive $-\vec{\nabla} p/\rho$ on the grid in R and Z space on which the gas reconstruction was calculated. Then I aim to determine the potential ϕ for which $\vec{\nabla}\phi$ is closest to $-\vec{\nabla} p/\rho$. I do that by finding the values of the potential ϕ at all grid points which minimise the deviation

$$\sum_{\text{neighbours } i,j} \Big(\phi_j - \phi_i + \frac{p_j - p_i}{\frac{1}{2}(\rho_j + \rho_i)}\Big)^2, \tag{3.42}$$

between these two vector fields. Here p_i, p_j are the gas pressures, ρ_i, ρ_j the gas densities and ϕ_i, ϕ_j the gravitational potentials at the R and Z coordinates of grid points i and j. The sum extends only over such pairs of grid points i and j that are nearest

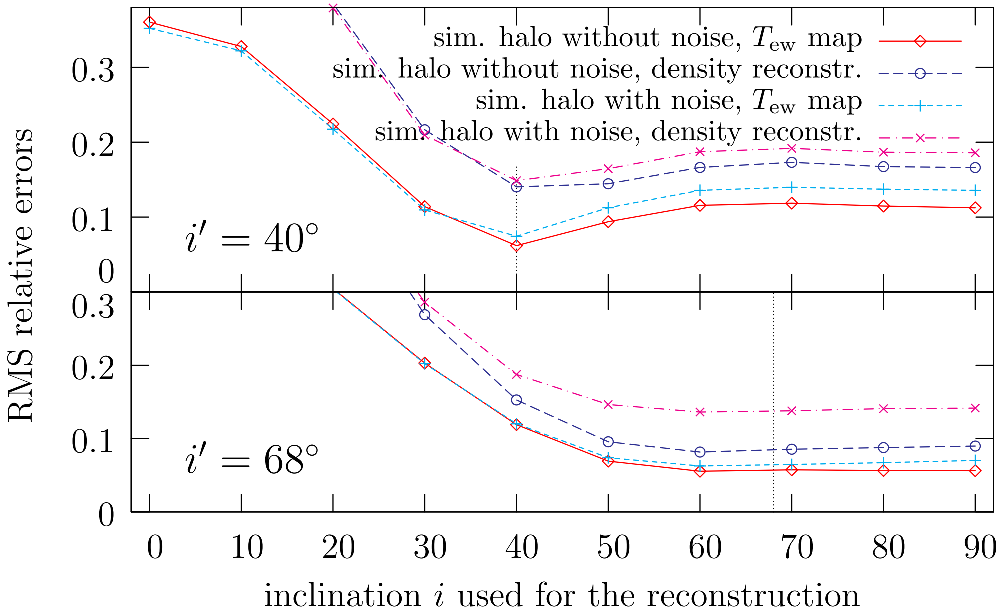

Figure 3.13: Accuracy of emission weighted temperature $T_{\rm ew}$ maps and densities for the reconstructed simulated halo *g51*. Maps obtained by projecting *g51* along a line-of-sight with inclination angles of $i' = 40°$ and $i' = 68°$ were used. The reconstruction assumed inclination angles i between 0° and 90°. Best reconstructions are obtained for $i \approx i'$. The errors are shown for deprojections from maps without observational noise but using "radius-dependent smoothing", and from maps with observational noise on which the complete smoothing scheme was applied. The RMS relative errors were obtained within a circle of radius $200\,h^{-1}$ kpc around the map centre for the T_{ew} maps and inside a sphere of radius $500\,h^{-1}$ kpc around the halo centre for the density reconstructions.

neighbours. Conjugate gradient minimisation starting with a guess $\phi_i = 0$ is used to find the solution for the ϕ_i.

However, to reduce noise in the potential it turned out to be favourable to add a penalty function to Eq. (3.42) that requires the second derivatives of the potential to be small. I also multiply each term in the sum in Eq. (3.42) and the penalty function by a weight factor. So the function I end up minimising is,

$$\begin{aligned} &\sum_{\text{neighbours } i,j} w(r_{i,j}) \big(\phi_j - \phi_i + \frac{p_j - p_i}{\frac{1}{2}(\rho_j + \rho_i)}\big)^2 + \\ &\quad w_p \sum_i \big((\phi_{iR_>} + \phi_{iR_<} - 2\phi_i)^2 + (\phi_{iZ_>} + \phi_{iZ_<} - 2\phi_i)^2\big), \end{aligned} \tag{3.43}$$

where $r_{i,j}$ is the distance from the cluster centre to the midpoint of the line connecting grid points i and j. $iR_>, iR_<$ and $iZ_>, iZ_<$ are the indices of the neighbouring grid points of point i in the R and Z directions, respectively. The weighting function $w(r)$ is chosen equal to one in the central region of the cluster, for $r < 0.3l$, then it smoothly goes to zero, and vanishes for $r > 0.4l$, close to the perimeter of the box with side length l that is used for the gas reconstruction (see Fig. 3.1). This is necessary because there are significant artefacts in the gas reconstruction close to the perimeter. When using the potential reconstruction algorithm proposed here they would have a non-local effect on the potential reconstruction and would thereby reduce its quality also near the cluster centre. The weight factor $w_p = 3$ for the penalty function was chosen by trial and error and proved to be effective. This algorithm is tested with synthetic data in Sect. 3.7.4.

One can then use the reconstructed three-dimensional gravitational potential to find the total mass distribution of the galaxy cluster.

3.5.10 The mass of the cluster halo

A simpler alternative way to get mass estimates from the gas reconstruction under the assumption of hydrostatic equilibrium, that does not require reconstructing the gravitational potential, is to apply Gauss's law to the gravitational field and use the hydrostatic equilibrium condition, given by Eq. (3.41), to express the gravitational field as $\vec{\nabla}p/\rho$. This allows one to define a cumulative mass $M_{<r,\,\mathrm{XSZ}}$ as a function of radius r from the cluster centre by

$$M_{<r,\,\mathrm{XSZ}} \equiv \frac{1}{4\pi G} \int -\frac{\vec{\nabla}p}{\rho} d\vec{A}, \tag{3.44}$$

where G is Newton's constant and the integral extends over the surface of a sphere with radius r around the cluster centre. The numerical evaluation of the integral is done using 128 sampling points which are equally spaced in the angular coordinate $\theta \equiv \arctan(Z/R)$. For each point the component of $\vec{\nabla}p/\rho$ perpendicular to the surface is calculated from the gas reconstruction and multiplied by the area of the corresponding ring. This method is applied to analytically modelled and numerically simulated clusters in Sects. 3.7 and 3.8.

3.6 A novel method to reconstruct clusters in three-dimensions from lensing data

A complementary way to study galaxy clusters is to observe gravitational lensing of background galaxies. The advantage of this approach is, that it does not rely on assumptions about the cluster's dynamical state, like the assumption of hydrostatic equilibrium, which is widely used in X-ray and thermal SZ based cluster studies.

3.6.1 The three-dimensional gravitational potential

Lensing observations allow reconstructions of the lensing potential (see Sect. 3.3 and e.g. [20]), which is simply the suitably rescaled projection of the lens gravitational potential along the line-of-sight. Once the lensing potential is found, Richardson-Lucy deconvolution can thus be applied to deproject it in order to obtain the three-dimensional gravitational potential. Again axial symmetry with respect to an arbitrarily inclined axis needs to be assumed.

I employ the deprojection algorithm discussed in Sects. 3.5.1 and 3.5.2 to obtain such three-dimensional reconstructions of the gravitational potential.

In Sect. 3.5.7 the optimal number of iterations for three-dimensional gas reconstructions was studied. Richardson-Lucy deconvolution reproduces large scale structure quickly, while it converges slowly to small scale structure. It turned out that for gas reconstructions based on X-ray and SZ data it is best to use about five iterations. For a smaller number of iterations the cluster structure is not recovered sufficiently well, while for a larger number of iterations the reconstruction algorithm tries to reproduce small-scale observational noise which can reduce the reconstruction quality again. However as the lensing potential is a much smoother quantity than the X-ray surface brightness or the SZ temperature decrement it is favourable to use a larger number of iterations for deprojections of the lensing potential.

However even when using a large number of iterations, problems with the gravitational potential reconstruction arise for small inclination angles i between the line-of-sight and the symmetry axis, because then the assumption of axial symmetry contains least information (see Sect. 3.5.4) and a reconstruction that, compared to the original halo, is stretched along the symmetry axis can still reproduce the lensing observations rather well. For a cluster with a roughly spherical gravitational potential and for a small inclination angle one gets too large correction factors close to the symmetry axis during the first few iteration steps when starting from a flat guess and thus the reconstruction after a few iterations is overly extended along that axis. As the power to determine the halo elongation along the symmetry axis is limited for small inclination angles the reconstruction algorithm takes very long to recover from this. To avoid this problem, it is thus favourable to start with a guess that has already more or less the right shape. I can get such a guess by doing a gravitational potential reconstruction from a flat guess with a small number of iterations and by then making the obtained potential spherically symmetric while preserving its profile. This spherically symmetrised potential can then be used as a first guess for the actual reconstruction with a larger number of iterations. 10 iterations were used to produce spherically symmetrised guesses for reconstructions from synthetic lensing data in Sects. 3.7 and 3.8. The actual reconstructions use 30 iterations and start either from such a spherically symmetrised guess or from a flat guess as specified there.

3.6.2 The mass of the cluster halo

The lensing three-dimensional gravitational potential reconstructions can then be used to find the total mass distribution and can be compared to reconstructions from X-ray and SZ data. In order to have a quantity that can be directly compared to $M_{<r,\,\mathrm{XSZ}}$, I define in analogy to Eq. (3.44) a lensing cumulative mass

$$M_{<r,\,\mathrm{lensing}} \equiv \frac{1}{4\pi G} \int \vec{\nabla}\phi d\vec{A}, \tag{3.45}$$

where ϕ is the three-dimensional gravitational potential obtained by deprojecting the lensing potential. The numerical evaluation of the integral is done in the same way as for $M_{<r,\,\mathrm{XSZ}}$.

3.7 Testing mass and three-dimensional gravitational potential reconstruction methods with analytic halos

In this section I will test the X-ray and SZ based (also abbreviated by XSZ) as well as the lensing based mass and three-dimensional gravitational potential reconstruction algorithms that were introduced in Sects. 3.5.9, 3.5.10, 3.6.1 and 3.6.2.

3.7.1 The halo model

For this purpose I use an analytic halo model with a NFW total (gas+DM) density profile. Thus the total matter density ρ_m and the gravitational potential are given by

$$\rho_m = \frac{4\rho_s}{\frac{r}{r_s}(1+\frac{r}{r_s})^2}, \tag{3.46}$$

$$\phi = \frac{16\pi G\rho_s r_s^3}{r}\ln\big(\frac{r_s}{r+r_s}\big), \tag{3.47}$$

where r_s is the NFW scaling radius and ρ_s is the density there. For the cluster gas I assume in this toy model that the ratio f of $\vec{\nabla}p/\rho$ to $-\vec{\nabla}\phi$ is constant but can be different from 1. So Eq. (3.41) generalises to

$$f\,\vec{\nabla}\phi = -\frac{\vec{\nabla}p}{\rho}. \tag{3.48}$$

I further assume a polytropic equation of state $T \propto \rho^{\gamma-1}$ for the cluster gas, where T is the gas temperature and γ the polytropic index. Then the gas density ρ and temperature T satisfy

$$\rho \propto \left[\frac{(1-\gamma)\phi}{\gamma}\right]^{\frac{1}{\gamma-1}}, \tag{3.49}$$

$$k_B T = f\frac{(1-\gamma)\phi}{\gamma}\bar{m}, \tag{3.50}$$

where $\bar{m}$ is the mean gas particle mass. In the following, I adopt $\gamma = 1.2$, which is consistent with X-ray temperature profiles of nearby clusters [65], and fix the normalisation of ρ by requiring a baryon fraction of 0.12 at the scale radius, which I set to $r_s = 300h^{-1}$kpc. Note that the lengths here and below are given in comoving units. A reduced Hubble parameter of $h = 0.7$ is used and ρ_s is chosen to be $4.75 \times 10^5 h^{-1} M_\odot / (h^{-1}\text{kpc})^3$. These choices for r_s and ρ_s correspond to a massive galaxy cluster. To test the reconstruction methods I put this analytically modelled cluster at a redshift of $z = 0.3$ and produce synthetic X-ray, thermal SZ and lensing observations.

3.7.2 Synthetic observations

Here in Sect. 3.7 as well as in Sect. 3.8, I use a more realistic model for the X-ray emission of the intra-cluster medium that now also includes line emission. The synthetic X-ray observations the reconstructions are based on as well as those that are performed during the iterative deprojection are now calculated with the MEKAL emission model (see [58, 45]) which includes line emission from several elements and the WABS model for galactic absorption [79]. More precisely I use the X-ray spectral fitting software package XSPEC [4] to create a table of the cooling function with the models mentioned above, assuming a constant metallicity of 0.3 times the Solar value and an equivalent hydrogen column density of 5×10^{20} atoms cm^{-2}. This table and a $128 \times 128 \times 128$ grid with $1.5h^{-1}$Mpc side length is then used to project gas distributions and get maps of the X-ray surface brightness in a 0.25-7.0 keV band. As discussed in Sect. 3.5.3, Eqs. (3.35) and (3.36) for the iterative corrections of the gas density and temperature can still be used. Except for reconstructions I specifically characterise as done without observational noise, I add photon noise corresponding to 10^4 observed source photons to the synthetic X-ray maps on which the reconstructions are based, using the method described in Sect. 3.5.5. “Photon-noise smoothing” is applied as described there, but no “radius-dependent” smoothing is used on the X-ray maps here and in Sect. 3.8.

The thermal SZ maps are generated exactly as discussed in Sects. 3.5.4 and 3.5.5. However in order to not bias the derived cumulative masses “radius-dependent” smoothing is strongly reduced. The maximum smoothing length here and in Sect. 3.8 is $h_{\mathrm{SML}} \approx 59h^{-1}$kpc. This does not introduce a significant bias but ensures that there are no points in the SZ map with a vanishing or negative Compton y-parameter which would cause numerical problems during the iterative gas reconstruction.

To produce maps of the lensing potential I project the mass inside a cube of $6\,h^{-1}$Mpc side length which is centred on the cluster along the line-of-sight and calculate the convergence. The grid I use for this purpose is chosen such that each pixel corresponds to roughly 1/3 square arcminute on the sky, so that it contains about 10 galaxies, if an average density of background galaxies useable for a weak lensing analysis of $n_g = 30/\mathrm{arcmin}^2$ is assumed. For instance for a cluster at redshift $z = 0.3$ a 44×44 convergence map covers the projection of the $6\,h^{-1}$Mpc cube on the sky.

For lensing reconstructions with observational noise, normally distributed noise with variance

$$\sigma_\kappa^2 = \frac{\sigma^2\sigma_\epsilon^2}{\pi n_g a^4}\Big(1 - \exp\big(-\frac{a^2}{2\sigma^2}\big) - \sqrt{\frac{\pi}{2}}\frac{a}{\sigma}\,\mathrm{erf}\big(\frac{a}{\sqrt{2}\sigma}\big)\Big)^2, \tag{3.51}$$

is added to each pixel of the convergence map. Here σ_κ^2 is the variance expected for a weak lensing reconstruction of the convergence for a density n_g of background galaxies with an intrinsic ellipticity dispersion σ_ϵ, and for an angular pixel size a of the convergence map [129]. It is assumed that the galaxy ellipticities are smoothed with a Gaussian of angular standard deviation σ before the reconstruction. I choose $\sigma = a$ and $\sigma_\epsilon = 0.3$.

Then the convergence map is used to calculate the lensing potential in Fourier space. A source redshift of 1.5 is assumed. To reduce errors introduced by the implicit assumption of a periodic convergence field of such Fourier methods (see Sect. 5.3.1), I first zero-pad the convergence map to 2048×2048 pixels. Once the map of the lensing potential is calculated, I crop it to its original size before using it for reconstructions.

3.7.3 Cumulative mass profiles

I applied these methods to produce synthetic X-ray, SZ and lensing observations for the analytic halo described in Sect. 3.7.1. I then generated three-dimensional reconstructions of the cluster gas based on X-ray and SZ data and reconstructions of the gravitational potential based on lensing data using the methods detailed above.

Figure 3.14 shows the cumulative mass profiles $M_{<r,\,\mathrm{XSZ}}(r)$, obtained from the X-ray, SZ (XSZ) reconstructions, and $M_{<r,\,\mathrm{lensing}}(r)$, obtained from the lensing reconstructions, and compares them to the original analytic profile. The profiles are shown for reconstructions based on data without observational noise and for reconstructions based on noisy data and for inclination angles $i = 30°$ and $i = 70°$ between the symmetry axis and the line-of-sight. The inclination angles were assumed to be known for the reconstructions. See Sect. 3.5.8 for methods to determine them from the observations. For the gas reconstructions ratios f of $\vec{\nabla} p/\rho$ to $-\vec{\nabla}\phi$ of $f = 1.0$ and $f = 0.8$ were used. The lensing reconstructions were done using both flat priors and spherically symmetrised priors.

The XSZ and the lensing mass profiles agree very well for a halo in hydrostatic equilibrium ($f = 1.0$) and when using data without noise and an inclination $i = 70°$ (see upper right panel of Fig. 3.14). They also excellently match the original analytic profile. The only significant difference between the profiles is that the lensing mass is too small very close to the cluster centre. However, this is completely expected because the lensing observations lack the resolution required to accurately resolve this region. When perturbing the hydrostatic equilibrium by 20%, in other words when assuming $f = 0.8$, the XSZ reconstructed mass profile is essentially 0.8 times the original analytic profile as theoretically expected. For such a halo one can easily see a significant ($\sim$ 20%) difference between the lensing and XSZ mass profiles. It directly reflects the deviation from the hydrostatic equilibrium condition. Also when adding noise to the synthetic observations (see lower right panel) such a deviation from hydrostatic equilibrium can be faithfully reproduced. For smaller inclination angles of $i = 30°$ (left panels) the accuracy of the reconstructions is somewhat lower and one can also see significant differences between the lensing reconstructions based on a flat prior and a spherically symmetrised prior. The latter reproduce the original profiles much better. Thus, for such small inclinations deviations from hydrostatic equilibrium can be detected by comparing lensing reconstructions based on a spherically symmetrised prior to XSZ reconstructions. Also note that for a randomly oriented cluster sample only about 13% of the clusters have inclination angles smaller than 30°.

Above I used spherically symmetrised priors in the lensing reconstruction of spherically symmetric halos. It is reassuring, but not really surprising that this works well. I thus need to check whether or not a spherically symmetrised prior also improves the lensing reconstruction quality of elliptical halos for small inclination angles. In Figure 3.15 I show lensing reconstructions of the cumulative mass profile of an elliptic analytic halo with an NFW density profile but isodensity surfaces that are prolate spheroids with a major to minor axis ratio of 2 to 1. The lensing reconstructions with a spherically symmetrised prior reproduce the original analytic profile well, both for small and for large inclination angles. On the other hand when using a flat prior I again obtain too small lensing masses for small inclination angles. It is thus favourable to use spherically symmetrised priors for iterative deprojections of lensing potentials.

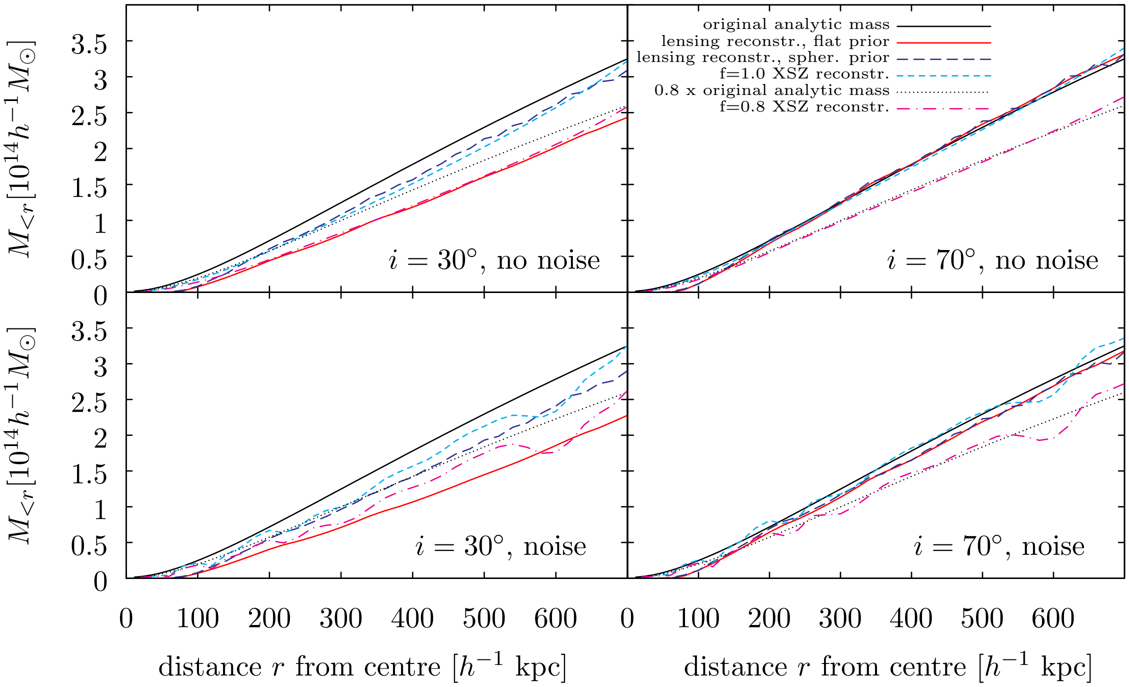

Figure 3.14: Cumulative mass profiles $M_{<r}(r)$ of an analytic halo and its reconstructions from X-ray and SZ maps with and without observational noise as well as from lensing maps with and without noise. The upper panels show the results obtained from maps without noise, while the lower panels show the profiles found from noisy maps. For the reconstructions shown in the left panels an inclination angle of 30° was used and assumed to be known, while the right panels show the corresponding results for an inclination angle of 70°. Lensing reconstructions are shown for a flat and for the spherically symmetrised prior. The XSZ reconstructions were done for halos with ratios f of $\vec{\nabla} p/\rho$ to $-\vec{\nabla}\phi$ of 1.0 and 0.8. For comparison I also show the original analytic cumulative mass multiplied by 0.8.

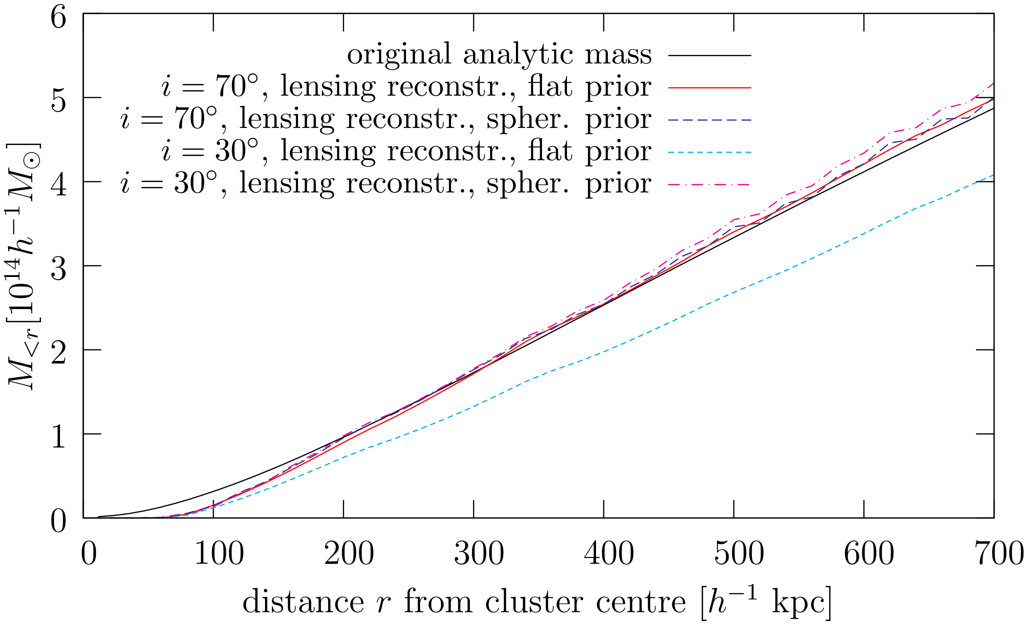

Figure 3.15: Cumulative mass profiles $M_{<r}(r)$ of an ellipsoidal analytic halo and its reconstructions from lensing maps without noise. Inclination angles of $i = 30°$ and $i = 70°$ were used for the synthetic observations and assumed to be known for the reconstructions. Lensing reconstructions are shown for a flat and for the spherically symmetrised prior.

3.7.4 Gravitational potential reconstructions

In Figure 3.16 I show three-dimensional reconstructions of the gravitational potential of the analytic halo from X-ray and SZ data and from lensing data as well as the original analytic gravitational potential described by Eq. (3.47). Reconstructions that are based on idealised observations without noise and on more realistic noisy observations are shown. The XSZ potential reconstructions were obtained from the X-ray, SZ cluster gas reconstructions by assuming hydrostatic equilibrium and by using the minimisation method described in Sect. 3.5.9. The lensing reconstructions were obtained directly by deprojecting the lensing potential. The XSZ reconstructions reproduce the inner region of the cluster well, while the lensing reconstructions lack the resolution to accurately resolve this innermost part. Between distances r from the cluster centre of $150h^{-1}$kpc and $450h^{-1}$kpc both reconstruction methods yield very good results. Farther outside the lensing reconstruction is still accurate, while the XSZ reconstruction becomes more and more unrealistic. This is partly due to different noise properties. But in the example shown in Figure 3.16 it is also due to the smaller box size used for the XSZ reconstructions and reconstruction artefacts that develop close to the perimeter of this box. The weighting function $w(r)$, which was introduced in Sect. 3.5.9 to prevent non-local effects of these artefacts, was chosen to decrease from unity to zero between $r = 450h^{-1}$kpc and $r = 600h^{-1}$kpc in these XSZ reconstructions. Thus they become unrealistic farther outside.

3.8 Probing the dynamical state of galaxy clusters

Hydrostatic equilibrium in galaxy clusters can be probed by comparing cluster reconstructions based on X-ray and SZ data to lensing reconstructions. In principle this could be done by comparing the gravitational potential obtained from the

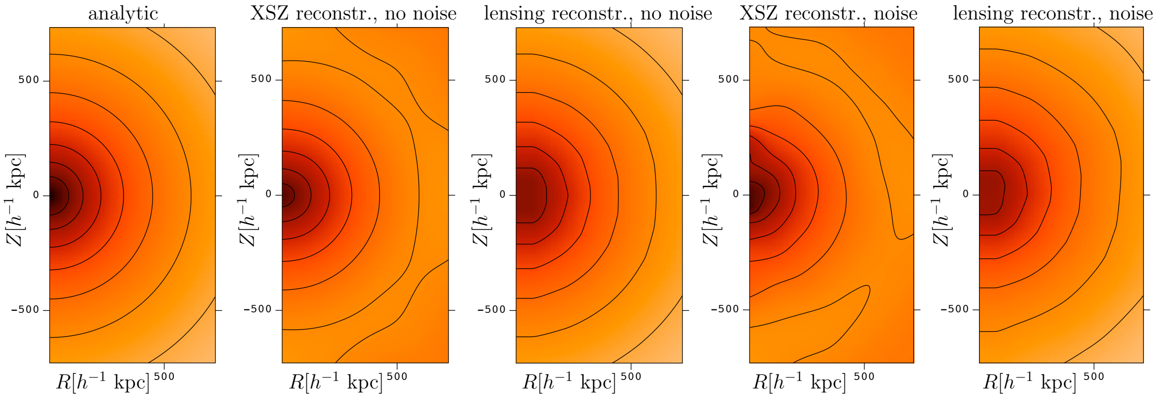

Figure 3.16: Gravitational potential of an analytic halo and its reconstructions from synthetic X-ray and SZ observations and from synthetic lensing observations each with and without observational noise. The XSZ reconstructions work well even close to the cluster centre, where lensing observations lack the resolution to accurately resolve the central peak. However, farther outside the lensing reconstructions perform better, due to the different noise properties, but in the example shown here also because of the smaller box size used for the XSZ reconstructions.

ICM reconstruction by minimising Eq. (3.43) to the one found by deprojecting the lensing potential. However as the gravitational potential is not uniquely defined it is more favourable to compare the cumulative masses $M_{<r,\,\mathrm{XSZ}}$ and $M_{<r,\,\mathrm{lensing}}$ defined in Eqs. (3.44) and (3.45). If the cluster is exactly in hydrostatic equilibrium, so that the hydrostatic equilibrium condition Eq. (3.41) is satisfied, the masses should be identical for all distances r from the cluster centre except for small deviations caused by reconstruction errors and non-thermal pressure components. Otherwise differences between the masses directly reflect the differences between the gravitational field and $\vec{\nabla}p/\rho$.

In Sect. 3.7.3, I found for analytic halos, that such deviations can be recovered by a comparison of XSZ and lensing cumulative mass profile reconstructions. Here I test this method to probe hydrostatic equilibrium in galaxy clusters by performing such a comparison using synthetic observations of numerically simulated clusters.

3.8.1 Probing hydrostatic equilibrium in simulated clusters

For such a more realistic test I now apply these methods to a sample of four numerically simulated galaxy clusters. I again use the GAS runs of clusters *g1*, *g8*, *g51* and *g72*. They are described in Sect. 2.3.

I produced synthetic X-ray, thermal SZ and lensing observations of these four simulated clusters for 28 simulation snapshots between redshifts 0.58 and 0.1 and three lines-of-sight using essentially the same methods as in Sect. 3.7.2 for the analytic halo. The only difference is that I did not use a three-dimensional grid for projections along the line-of-sight. For the X-ray and SZ maps the X-ray luminosities and integrated Compton y-parameters of the gas particles are projected directly onto a two-dimensional 128×128 grid by using the particles' projected SPH smoothing kernels. The convergence of the simulated clusters is found in a similar way by projecting the masses of both gas and dark matter particles onto a two-dimensional grid, whose dimensions are again chosen such that one pixel corresponds to roughly 1/3 square arcminute on the sky. Observational noise is added in exactly the same way as in Sect. 3.7.2.

Based on these synthetic observations I perform three-dimensional XSZ reconstructions of the cluster gas distribution and lensing reconstructions of the gravitational potential. The inclination angle is assumed to be known for the reconstructions. Methods to determine it from data are discussed in Sect. 3.5.8. A symmetry axis is chosen for the simulated clusters in the same way as in Sect. 3.5.6. Spherically symmetrised priors are used for the lensing reconstructions. The reconstructions are then used to probe hydrostatic equilibrium by calculating and comparing their cumulative mass profiles $M_{<r,\,\mathrm{XSZ}}(r)$ and $M_{<r,\,\mathrm{lensing}}(r)$.

In Figure 3.17, I show these profiles for two clusters that did not experience a major merger recently. For comparison I also show the original simulated mass profile and the profile that would be expected from the original simulated gas distribution by assuming hydrostatic equilibrium. The latter is calculated like $M_{<r,\,\mathrm{XSZ}}(r)$, however directly from the simulated gas distribution rather than the reconstructed one. I again use 128 rings which are equally spaced in the polar angle θ to numerically evaluate the surface integral in Eq. (3.44), but as the simulated gas distribution is not perfectly axisymmetric I use 128 sampling points equally spaced in the longitude angle for each of these rings. The gas density ρ and the pressure gradient $\vec{\nabla}p$ are calculated at each sampling point using the SPH formalism, i.e. by summing up the contributions from all nearby particles using their SPH smoothing kernels and the gradients thereof, namely Eq. (2.8) is used for calculating pressure gradients. For these relaxed clusters the XSZ reconstructed profiles and the lensing reconstructed profiles agree well with each other, with the original mass profile and the profile obtained from the original gas distribution. This shows that for such relaxed clusters this method allows accurate and consistent lensing and XSZ mass estimates. The results also confirm that these clusters are close to hydrostatic equilibrium.

It is reassuring that this novel method to probe hydrostatic equilibrium works well for clusters that do not have a record of recent mergers. However clusters that do experience such violent events may be even more interesting to study. In Figure 3.18 I show a cluster at four different times during a merger. For each of these snapshots I show reconstructions of the cumulative mass profile from synthetic X-ray, SZ and lensing observations, as well as the original mass profile and the profile obtained from the simulated gas distribution. Again observational noise was added to the synthetic maps used for the reconstruction. X-ray maps of the cluster are also shown for each of the four snapshots. These are however idealised noise-free versions and just meant to illustrate what is going on in the cluster. To facilitate following the merger I show the approximate trajectory of the relevant infalling subhalo in the X-ray maps.

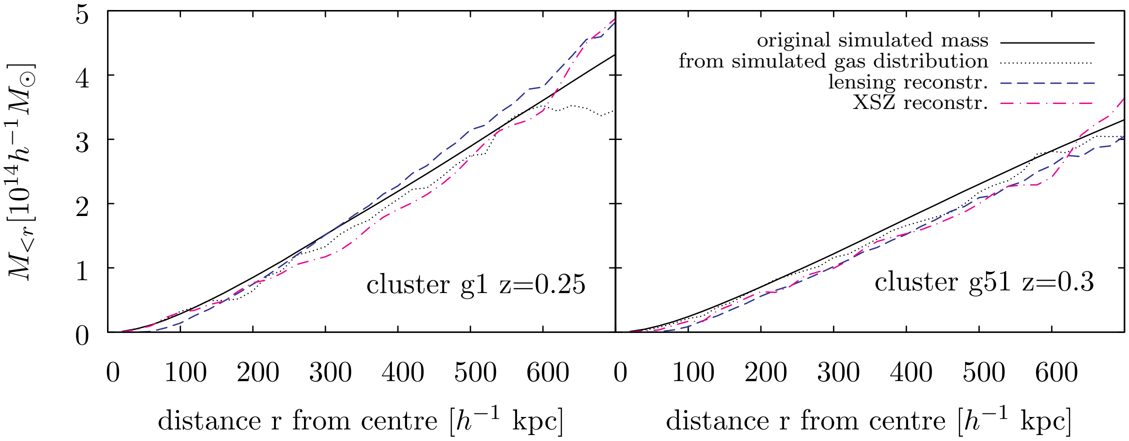

Figure 3.17: Cumulative mass profiles $M_{<r}(r)$ of relaxed simulated clusters *g1* at redshift $z = 0.25$ and *g51* at redshift $z = 0.3$. Profiles of the original simulated mass distribution, of the lensing and of the XSZ reconstructions are shown, as well as the profile obtained directly from the simulated gas distribution by assuming hydrostatic equilibrium. The lensing and XSZ reconstructions are based on synthetic observation that contain observational noise. For such relaxed clusters both the lensing and the XSZ reconstructions agree very well with the original mass profile.

In the first snapshot (upper left panel) the main cluster halo is still close to hydrostatic equilibrium. The lensing and XSZ mass estimates still agree well for radii r smaller than the distance to the infalling subhalo. In the second snapshot (upper right panel), after the subhalo has passed the main halo, shocked gas causes a too large XSZ mass estimate from roughly the subhalo distance outwards. The mass profile obtained directly from the simulated gas distribution shows the same behaviour and thus confirms that this is not an artefact of the reconstruction but a real, significant deviation from hydrostatic equilibrium, which is recovered by the reconstruction or in this example even somewhat overestimated. The lensing reconstruction still reproduces the original simulated mass profile well. Thus by comparing lensing and XSZ cumulative mass profiles one can directly see the deviations from hydrostatic equilibrium. The third snapshot (lower left panel) shows that when the bow shock moves outward one can also obtain too low cluster masses by assuming hydrostatic equilibrium during a merger. Again the effect can be seen in both the mass profiles obtained directly from the simulated gas distribution and obtained from the three-dimensional XSZ gas reconstruction. In the fourth snapshot (lower right panel) hydrostatic equilibrium is already largely restored, even if one can still see the pronounced bow shock in the X-ray map.

These simulations show that deviations from hydrostatic equilibrium during mergers can be faithfully recovered by the cluster reconstruction methods introduced above.

3.8.2 Accuracy and reliability of cumulative mass profile reconstructions

To determine the typical scatter in cumulative mass profile reconstructions and quantify the significance of detections of deviations from hydrostatic equilibrium I repeated the reconstruction of the merging simulated cluster shown in the upper right panel of Fig. 3.18 with different noise realisations and for different lines-of-sight.

For the left panel of Fig. 3.19 I used the same line-of-sight as in Fig. 3.18 but 50 different noise realisations for the synthetic X-ray, thermal SZ and lensing observations. The noise realisations were obtained by using different seeds for the random number generator employed for adding noise to the synthetic observations. The mean XSZ and lensing reconstructed profiles and the 1-σ errors are shown as well as the profile of the original simulated mass distribution and the profile obtained directly from the simulated gas distribution by assuming hydrostatic equilibrium. The deviations from hydrostatic equilibrium are reliably detected. As expected for a cluster that contains substructure that violates axial symmetry there are also some systematic deviations such that the mean profiles are not centred exactly on the simulated

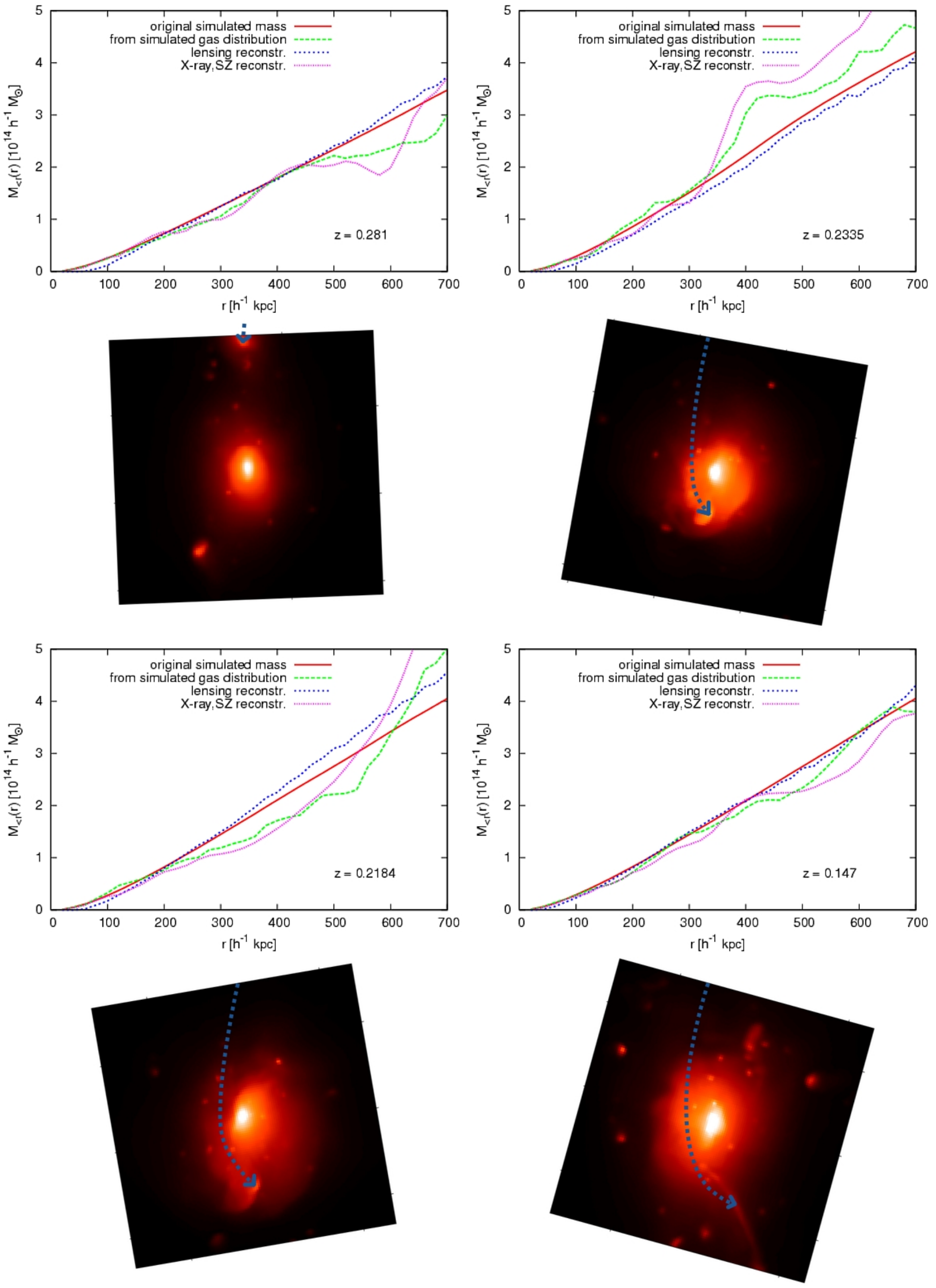

Figure 3.18: Cumulative mass profiles $M_{<r}(r)$ and X-ray surface brightness maps of simulated cluster *g51* at four different redshifts during a merger. The approximate trajectory of the infalling subhalo is illustrated in the X-ray maps. Profiles of the original simulated mass distribution, of the lensing and of the XSZ reconstructions are shown, as well as the profile obtained directly from the simulated gas distribution by assuming hydrostatic equilibrium. The lensing and XSZ reconstructions are based on synthetic observation that contain observational noise. The X-ray maps shown above are however idealised noise-free versions and were rotated such as to all have the same orientation in space.

profiles.

For the right panel I started with a sample of synthetic lensing, X-ray and SZ observations along 50 different randomly oriented lines-of-sight. All contain realistic observational noise. It turned out that for projections for which the merging subhalo responsible for perturbing hydrostatic equilibrium is almost directly in front of or behind the main halo detecting deviations from hydrostatic equilibrium is less reliable. This is not surprising as the signal from the region where hydrostatic equilibrium is strongly perturbed is superimposed with a larger signal from the main halo, so that the contributions to such projections are difficult to separate. For the right panel of Fig. 3.19 I thus decided to reject all 16 lines-of-sight for which the projected distance of the relevant subhalo from the main halo centre is less than $200\,h^{-1}$ kpc, as well as one line-of-sight which happened to be inclined by only 2° with respect to the cluster's symmetry axis which is to small for a faithful reconstruction. The mean and the 1-σ errors of the reconstructions that were based on the 33 remaining lines-of-sight are shown. Again deviations from hydrostatic equilibrium can be reliably detected.

As discussed in Sect. 3.5.2 reconstruction artefacts can appear close to the perimeter of the box used for the reconstructions. As one can see in the right panel of Fig. 3.19 they can dominate the XSZ reconstructed cumulative mass profiles' errors from roughly $r = 600h^{-1}$ kpc outwards for some lines-of-sight, when using a $1.5h^{-1}$ Mpc sidelength box for the XSZ reconstruction. Thus when the quality of the observations allows studying a larger region one should also use an appropriately larger box for the XSZ reconstruction to avoid this problem.

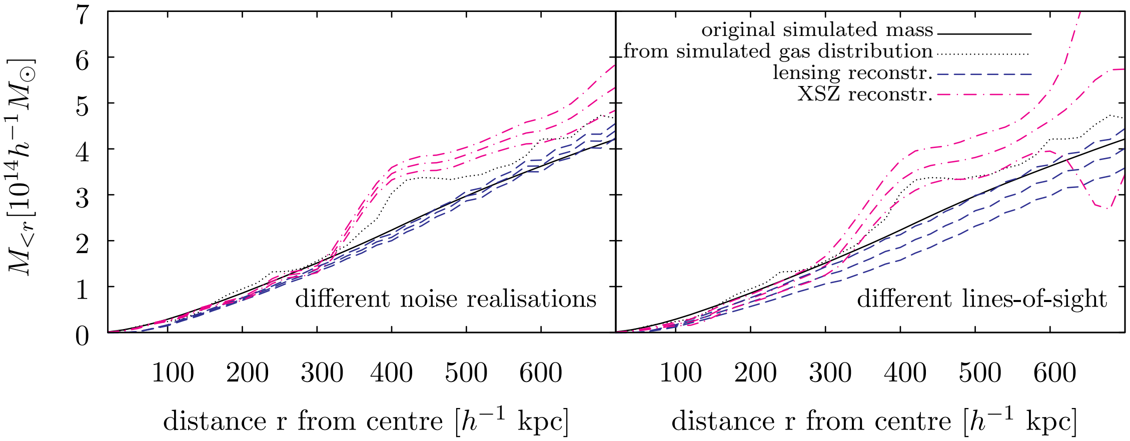

Figure 3.19: Mean XSZ and lensing reconstructed cumulative mass profiles $M_{<r}(r)$ and their 1-σ errors of merging simulated cluster *g51* obtained for different noise realisations (left panel) and different lines-of-sight (right panel). Profiles of the original simulated mass distribution and the profiles obtained directly from the simulated gas distribution by assuming hydrostatic equilibrium are shown for reference. X-ray, SZ and lensing observations along one line-of-sight but with 50 different noise realisations were used for the reconstructions whose mean and 1-σ errors are shown in the left panel. For the right panel I started with a sample of noisy synthetic observations along 50 different randomly oriented lines-of-sight. However I rejected projections for which the merging subhalo is almost directly behind or in front of the main halo (projected distance $< 200\,h^{-1}$ kpc) as well as one line-of-sight with an inclination of only 2° with respect to the clusters symmetry axis which is to small for a faithful reconstruction. The mean and the 1-σ errors of the profiles reconstructed from the observations along the remaining 33 lines-of-sight are shown. For both the different noise realisations and the different lines-of-sight deviations from hydrostatic equilibrium can be reliably detected.

Chapter 4

Cluster abundance and cosmology

The abundance of galaxy clusters is very sensitive to cosmology. One can thus constrain cosmological parameters by measuring it as a function of cluster mass and redshift (see e.g. [130] for a pedagogical review). I will discuss to which parameters cluster abundance studies are sensitive, what degeneracies arise and how some of them can be broken. In addition the effects of scatter and evolution in mass-observable relations are considered.

4.1 Constraining cosmology by local measurements of the cluster mass function

As one can see from the Press-Schechter mass function given in Eq. (1.25), the number density of halos depends mostly on the amplitude of fluctuations σ_R and the matter density $\rho_b = \Omega_m \rho_{\rm crit}$, where the critical density of the universe $\rho_{\rm crit}$ is related to the Hubble parameter by $\rho_{\rm crit} \propto H^2$. Thus, in terms of the typically used cosmological parameters, the abundance of clusters at the present epoch is essentially given by the normalisation of the matter power spectrum σ_8, the matter density parameter Ω_m, and the Hubble constant H_0. However, redshifts are used to determine the distance of galaxy clusters, and cluster surveys primarily yield cluster numbers. Hence, the number densities inferred from local cluster mass function studies are proportional to the assumed H_0^3. The first term on the right hand side of Eq. (1.25), namely ρ_b/M is also proportional to H_0^3 when considering a mass scale corresponding to $R = 8h^{-1}\mathrm{Mpc}$, as $\rho_b = \Omega_m \rho_{\mathrm{crit}} \propto \Omega_m H_0^2$ and $M(8h^{-1}\mathrm{Mpc}) \propto \rho_b R^3 \propto \Omega_m H_0^{-1}$. Thus the dependence on the Hubble constant drops out and one is left with a degeneracy of σ_8 and Ω_m only. Around $\sigma_R \approx 1$, the Press-Schechter mass function is roughly proportional to $\Omega_m \sigma_R^2$, so that essentially the combination of parameters $\sim \Omega_m \sigma_8^2$ is probed by measuring local cluster abundance. Qualitatively the same result is found when considering more accurate CDM mass functions.

A simple determination of σ_8, assuming some fixed value of Ω_m, could be achieved by measuring the number density of clusters in logarithmic bins of some mass-tracing observable X, namely $dn/d\ln X$. To then convert this data to a mass function one needs to know at least the effective power-law index of the mass-observable relation $\alpha_X \equiv d\ln X/d\ln M$ in the appropriate range as well as the effective power-law index of the mass fluctuations $\alpha_M \equiv d\ln\sigma^{-1}/d\ln M$. This allows fitting an analytic expression like Eq. (1.25) (or preferably a more accurate Sheth-Tormen [113] or Jenkins [42] mass function) to the observed number density at some mass scale M_{fit}, which yields $\sigma_{\mathrm{fit}} = \sigma_R(M_{\mathrm{fit}})$. σ_8 is then obtained by $\sigma_8 \approx (M_{\mathrm{fit}}/M_8)^{\alpha_M}\sigma_{\mathrm{fit}}$. From this one finds that a systematic error $\Delta M/M$ in the mass-observable relation causes a relative error in the measured σ_8 given by (see also [130])

$$\frac{\Delta\sigma_8}{\sigma_8} = \left(\alpha_M + \frac{d\ln\sigma_{\mathrm{fit}}}{d\ln M_{\mathrm{fit}}}\right)\frac{\Delta M}{M}. \tag{4.1}$$

Using numerical simulations in different cosmologies it was shown that the factor in parenthesis typically asymptotes to ~ 0.4 above $\sim 5\times10^{14}h^{-1}M_{\odot}$, while it is larger at lower cluster masses [32], reaching unity at about $10^{14}h^{-1}M_{\odot}$. Thus, the most massive systems allow the strongest constraints on σ_8, as long as one is not limited by statistics due to their smaller number. A systematic 25% error in their mass determination implies only a 10% error in σ_8.

It is also important to consider scatter in the mass-observable relation. Due to the steep cluster mass function, the number of lower-mass clusters scattering to higher values of the observable far exceeds the number of higher-mass clusters scattering to lower observable values. This biases the observed abundance of clusters high, when an observable threshold is used as selection criterion, and can lead to an overestimate of σ_8. This effect is particularly strong when the scatter has a long tail towards large values of the observable. For example merger boosting of X-ray luminosities and temperatures can cause such a tail in the scatter of X-ray scaling relations [100]. However, when calibrating the mass-observable relation from observations ignoring scatter, a resulting bias in the calibration can dominate and lead to an underestimate of σ_8 [63].

The most commonly used mass-observable relations in cluster abundance studies are the X-ray mass-temperature and mass-luminosity scaling relations (see also Sect. 1.3.4). However, also mass-velocity dispersion [36] and mass-richness relations [6] have been used. For upcoming submillimeter surveys SZ scaling relations will be very important.

In principle there are several ways how the degeneracy of Ω_m and σ_8 can be broken. One could determine one of the parameters using a different method or measure the mass function over a wide range of masses to break the degeneracy by precisely determining the mass function's shape. The latter approach was applied to X-ray data in [103]. However, the obtained $\Omega_M = 0.12^{+0.06}_{-0.04}$ is very small compared to other measurements, while their Ω_M-σ_8 relation, namely $\sigma_8 = 0.43\Omega_M^{-0.38}$, agrees much better with, e.g., recent WMAP data [116]. Alternatively, one can measure the cluster mass function's evolution. This approach is discussed in more detail below.

4.2 Constrains from the evolution of the cluster mass function

Analysing how the abundance of galaxy clusters depends on redshift can yield valuable information (see [130] for a review). A quantity that is observationally accessible is the number of clusters dN within a given solid angle $d\Omega$, a redshift interval $[z, z{+}dz]$, and a range $[X, X{+}dX]$ of the observable. Assuming that the mass-observable relation and its dependence on redshift is known, one could determine the distribution $dN/(dM dz\, d\Omega)$ of clusters, which is related to the cluster mass function by

$$\frac{dN}{dMdzd\Omega} = \frac{dn}{dM} \cdot \frac{dV_{\mathrm{com}}}{dzd\Omega}, \tag{4.2}$$

where dn/dM is the cluster mass function at redshift z and dV_{com} is the comoving volume in $d\Omega$ and $[z, z{+}dz]$. Thus, by measuring the abundance of clusters at different redshifts cosmology is probed through both the evolution of the mass function and the evolution of this volume factor. In practice, however, one is often limited by incomplete knowledge of the evolution of the mass-observable relation.

The evolution of the mass function is strongly affected by cosmology because the growth rate of structure is very sensitive to the matter density. For $\Omega_M \approx 1$, one finds $\sigma_R \propto (1+z)^{-1}$, while the growth of linear perturbations stops for $\Omega_M \ll 1$. Hence, for fixed $\sigma_R(0)$, $\sigma_R(z)$ will be significantly smaller in a high matter density cosmology, even for moderate redshifts z. Due to the exponential dependence of the mass function on σ_R, the abundance of massive clusters with $\sigma_{R(M)}(0) < 1$ is strongly suppressed at moderate and high redshifts in such cosmologies. This property allows breaking the Ω_M-σ_8 degeneracy. For example, applying this technique to ROSAT Deep Cluster survey data yielded $\Omega_M = 0.35^{+0.13}_{-0.10}$ and $\sigma_8 = 0.66^{+0.06}_{-0.05}$ [18].

The redshift distribution of clusters is also sensitive to dark energy. For fixed Ω_M, growth of structures is suppressed in open models compared to a flat ΛCDM cosmology, resulting in flatter cluster number density redshift distributions. Dark energy models with an equation of state $w > -1$ also suppress the growth of structure compared to the $w = 1$ case, which again flattens the redshift distributions. Although the volume factor in Eq. (4.2) is smaller in open and $w > -1$ cosmologies than in a ΛCDM model, the growth factor dominates at $z \gtrsim 0.7$ resulting in a larger numbers of high-redshift clusters in the former models (see e.g. [38]). Thus assuming flatness, measuring the cluster redshift distribution to high redshift can constrain the dark energy equation of state. There are only mild degeneracies with Ω_M and H_0 [38]. However when dropping the flatness assumption, the effects of increasing w and "opening" the universe are very similar (see also [22]). Current cluster abundance studies do not allow strong constraints on the dark energy equation of state, but upcoming surveys are promising (see e.g. [62] for the accuracies expected to be achieved with SPT, PLANCK and DUET).

Mass-observable relations, including all the scaling relations derived in Sect. 1.3.4, evolve with redshift. One of the reasons for that is the fact that the virial density of clusters is linked to the critical density ρ_{crit} of the universe. Instead of $M \propto R^3$, one should thus rather use $M \propto \rho_{crit} R^3 \propto H^2(z) R^3$ in the derivation of these scaling relations. This leads to a mass-temperature relation of the form $T \propto M^{2/3} H^{2/3}(z)$. Unfortunately, there is additional more complicated redshift evolution in mass-observable relations due to astrophysical processes like cooling, galaxy formation and feedback. Scatter in the relations may also be larger at higher redshift because the fraction of relaxed clusters may be smaller there. In addition, observations can cause spurious redshift dependence, mainly because high redshift clusters are harder to observe. SZ surveys may be less affected by this at high redshift because temperature decrements are independent of cluster redshift.

There are several ways to take evolution in mass-observable relations into account. One can assume a model for their evolution, e.g. based on numerical simulations, or parameterise their redshift dependence and try to calibrate the parameters from detailed observations of smaller cluster samples using methods like those described and introduced in Chapter 3, as well as by cross-comparing the relations of multiple mass-tracing observables. Another approach is to find such parameters by "self-calibration" techniques [53], which means that both the sought cosmological parameters and the parameters describing the mass-observable relation, which can include parameters describing its scatter, are found by fitting the observed distribution of clusters in redshift and observable. This, however, requires large surveys extending to high redshift. The accuracy is limited by the number of free parameters in the mass-observable relation. Thus a realistic model of the relation's evolution can increase the accuracy by keeping the number of free parameters small. This technique may be promising for large future cluster surveys and would allow constraining both cosmology and cluster physics at the same time. Also combinations of "self-calibration" techniques and observational calibration have been suggested as well as including information from redshift-averaged cluster power spectra [62].

Chapter 5

Strong lensing and cluster structure

The structure of cluster halos and their ability to produce giant arcs are closely related. Certainly, more massive and more concentrated clusters are more likely to produce giant arcs, but also ellipticity and substructures play an import role [13]. So far, the impact of baryonic physics has been neglected in most strong cluster lensing studies. I will study it in detail in Sect. 5.3.

The abundance of giant arcs is also very sensitive to cosmology [10]. Comparing predictions to observations could thus be a valuable cosmological probe. However, taking all effects that could affect the predicted number of giant arcs correctly into account is a very difficult task. An overview of comparisons that have been performed will be given in Sect. 5.2.

5.1 The impact of substructure, ellipticity and mergers on arc statistics

If a cluster lens is perfectly axisymmetric with respect to the line-of-sight, its tangential caustic is pointlike. It is therefore not surprising that such a cluster is not an efficient strong lens. Only galaxies that are almost directly behind the cluster centre are able to produce large tangential arcs. However, if ellipticity is introduced into the cluster mass distribution, the tangential caustic expands to a diamond shape with four cusps (see e.g [80] for a review), which already allows background galaxies on a much larger patch of the sky to get strongly lensed (e.g. [71]). Further asymmetries and substructures can increase the number of cusps. However, background galaxies close to cusps are particularly likely to form long arcs, as there three images can merge to form one giant arc. Thus substructures and tidal fields of the surrounding matter distribution make clusters considerably more efficient strong lenses [71].

During mergers, where large substructures approach the main halo centre, tangential caustics of clusters and infalling subhalos are stretched along the direction along which the merger proceeds. When the halos come close enough to each other their caustics merge. This stretching and merging of caustics as well as the higher projected mass density when the halos reach their minimal distance boost the efficiency of clusters to produce giant arcs [128, 69]. The cross section for long thin arcs can grow by an order of magnitude. There can also be several maxima in the cross section during a merger, i.e. when the critical curves (and caustics) reach their maximum extent and when the projected distance of the subhalo is minimal.

From the discussion above it is clear that the effects of cluster asymmetries, substructures and mergers need to be taken into account, when deriving predictions for giant arc abundance that shall be compared to observations.

5.2 The arc statistics problem

Different cosmological models yield different cluster mass functions (see Sec. 4.2), cluster concentrations, and merger rates as a function of redshift. In addition the volume per unit redshift depends on the considered cosmology. The abundance of giant arcs is sensitive to all these quantities in a highly non-linear way. It is thus not surprising that the arc abundance depends on cosmology.

Using clusters extracted from numerical simulations of different cosmologies and sources fixed at redshift $z = 1$, it was shown that there is indeed a huge difference in the abundance of arcs between different cosmological models [10]. All models in that study were normalised to reproduce the local number density of rich clusters. The expected number of arcs in an open CDM model was found to be almost an order of magnitude larger than in a ΛCDM universe, in which in turn by about the same factor more arcs than in a flat CDM universe were found. This can be understood by the earlier formation time of clusters in low-matter density universes, causing massive clusters to be more abundant at redshifts where they can be efficient lenses (see also Sec. 4.2). In addition clusters that form earlier are significantly more concentrated and thus more efficient lenses. Also the volume per unit redshift is larger in low-matter density universes. It was concluded that only the open CDM model can explain the large number (e.g. [139]) of observed arcs, which is problematic as virtually all other observations strongly favour a flat universe with a low matter density.

Subsequent studies showed that considering the effect of cluster galaxies [72] or dark energy models with an equation of state $w > -1$ [11] is unlikely to reconcile arc statistics with a flat low matter density universe. On the other hand taking cluster mergers into account is certainly important (see discussion in Sect. 5.1 and [128]).

It was further found that using a broader redshift distribution of sources can significantly increase the optical depth for long thin arcs [131]. Thus, when allowing sources at redshifts extending to or beyond $z = 1.5$ a ΛCDM universe with $\sigma_8 = 0.95$ can reproduce the observed arc abundance. However, some authors argued that by approximating length-to-width ratios by magnification, the arc abundance may be overestimated [24, 56].

It was also found that a ΛCDM universe populated with triaxial halo models with a steep inner slope $\rho \propto r^{-1.5}$ and axis ratios taken from numerical dark matter simulations can reproduce the observed arc numbers, while triaxial NFW halos fail in doing so in a ΛCDM cosmology [90]. This shows that the arc statistics problem is also closely related to the problem of constraining inner slopes of cluster density profiles. If one believes in shallow $\rho \propto r^{-1}$ inner slopes of CDM halos, baryon cooling could further steepen density profiles to values required by such analyses to reproduce observed abundances (see e.g. Fig. 2.1). However, it also makes clusters more spherical, which may make their axis ratios inconsistent with the values assumed in that study and would reduce the abundance of arcs.

Another study using numerically simulated clusters extracted from a ΛCDM universe with $\sigma_8 = 0.9$, using partly the same cluster sample as [10], found that observed arc numbers can be reproduced [24]. In that analysis arc widths are calculated by considering arcs as rectangles, which may be less realistic than considering them as ellipses. Compared to [10], a higher value for the source density and a larger lensing fraction of observed clusters was used for the comparison of predictions to simulations.

I short, it is still not completely clear whether or not a flat ΛCDM model with $\sigma_8 \approx 0.9$ and $\Omega_m \approx 0.3$ is able to reproduce the high observed giant arc abundances, and if not how much of a discrepancy there is. On the other hand, if one believes the cosmological parameters derived from the WMAP three-year data [116], the predicted arc abundance drops by about a factor ~ 6 [57] compared to the former model. In that case there clearly is a discrepancy between current theoretical predictions and observations.

Previous studies of the ability of clusters to form giant arcs neglected the impact of baryonic physics. It will be studied in detail in the next section.

5.3 The impact of baryonic physics on arc statistics

In this section I study the impact of baryonic physics on strong cluster lensing by comparing the lensing properties of numerical clusters, which were simulated using different gas physics models. The simulated cluster sample is described in detail in Sect. 2.3. All different simulations of a specific cluster were started from the same initial conditions, so as to allow a direct comparison.

I calculate deflection angle maps for the simulated clusters and perform a "ray-tracing" simulation to find and classify the images of background galaxies that I place on an adaptive grid behind the cluster. This allows me to calculate strong lensing cross sections, study their evolution and compare them for the different gasdynamical simulations.

5.3.1 Calculating deflection angle maps for simulated clusters

First, the centre of each cluster is found by using the halo-finder algorithm discussed in [127]. It estimates the dark-matter density at the position of each dark-matter particle by determining the distance to the tenth-closest neighbour d_{10} and by also assuming that the density at the particle position is proportional to d_{10}^{-3}. Starting at the particle with the highest density, the virial sphere of the particle distribution is found, in which the gravitational potential is then determined. The halo centre is taken to be at the potential minimum.

For studying the lensing properties of each cluster, I choose a sphere of comoving radius $3\,h^{-1}\,\mathrm{Mpc}$ around the cluster centre and project all cluster particles inside this region onto an equidistant grid with a resolution of 4096×4096 cells. For the projection I use the same cubic spline function which is used in the GADGET code as the SPH smoothing kernel [123]. I project by calculating the overlap between the projected spline function and the squares representing the pixels of the grid.

From the projected mass map, I calculate the convergence κ and its Fourier transform $\hat{\kappa}$, which as can be easily seen from Eq. (1.46) is related to the Fourier transform of the lensing potential $\hat{\psi}$ by

$$\hat{\psi} = -\frac{2}{k^2}\hat{\kappa}\ . \tag{5.1}$$

Employing fast-Fourier methods for deriving the lensing potential according to this equation is, however, problematic. Discrete Fourier transform algorithms assume that the function to be transformed is periodic on its support, which is not the case for isolated and finite cluster convergence fields. Equation (5.1), therefore, does not yield the lensing potential of a single cluster, but that of an infinite, two-dimensional *array of clusters* (see Fig. 5.1), in which the original cluster is repeated on a grid whose periodicity is set by the side length of a single cluster field (here $6\,h^{-1}\,\mathrm{Mpc}$ comoving).

Thus, a sufficiently accurate result is only achieved close to the centre of the cluster field. For reducing the error, I could surround the cluster by an even larger zero-padded field. However, doing so without losing resolution substantially increases the demands on computer memory and slows down the computation. I have therefore chosen to use a new method to correct for these errors. I place a point mass that concentrates the total projected mass of the cluster at the cluster's centre-of-mass. I then calculate the lensing potential for an array of these point masses with the Fourier method mentioned above. Next, I analytically subtract the lensing potential of the single point mass located at the cluster's centre-of-mass so as to obtain the lensing potential of an array of point masses with one mass missing at the position of the original cluster. Subtracting this from the potential obtained for the *array of clusters*, I correct for the *additional clusters* implicitly produced by the fast-Fourier algorithms, which assume a periodic convergence array. The remaining error comes only from the higher multipole moments of these *additional clusters* and can be neglected in the central sixteenth (1024×1024 points) of the grid which I use for doing arc statistics. From this corrected lensing potential, I calculate the deflection angle using Eq. (1.45).

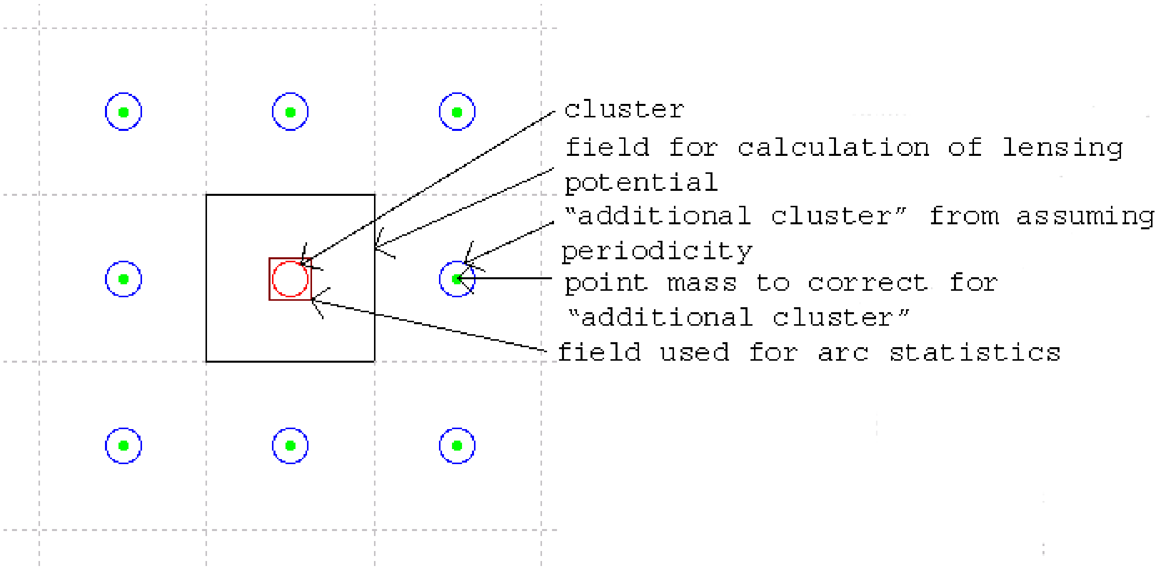

Figure 5.1: Illustration of my method for correcting the error caused by the implicit assumption of a periodic input function in fast-Fourier techniques.

5.3.2 Ray-tracing simulations and image classification

For finding the images of a number of sources large enough for statistical analysis, I follow the method introduced by [73, 74] and adapted to non-analytic models by

[14] and [13]. A previous version of the algorithm is also discussed in some detail in [72]. The algorithm used here places elliptical sources with an equivalent radius of 0.5 arc seconds on an adaptive grid in the source plane, which is fixed at redshift 1.5 (the lens redshift is taken to be the redshift of the simulation snapshot), such that the density of sources increases towards the caustics. A statistical weight is assigned to each source, which is given by the area represented by the source.

Next, the deflection angles are used to trace light rays backwards and map each grid point from the lens plane to the source plane. The images of a source are found by checking which grid points, when mapped back to the source plane, are enclosed by the ellipse corresponding to the source considered. To determine the image properties (e.g. length L, width W, and curvature radius R), the algorithm finds the image point (a) which, when mapped to the source plane, falls closest to the source centre, the image point (b) which is the farthest from (a), and the image point (c), which is the farthest from (b) along the circumference of the image. The method is illustrated in Fig. 5.2.

I could fit a circle through these three points and use the arc length from (b) to (c) as the length of the image, as it was done in [72]. I would then determine the image perimeter by walking along the ordered boundary points and summing up their mutual distances. But since grid cells in the lens plane are only classified as belonging to the image if their centres fall within the source, the boundary points of the image (including (b) and (c)) will on average be about half a grid constant further inside the image than the true perimeter. Thus, I would systematically underestimate the length of the image by roughly one grid constant. I would also underestimate the perimeter of the image. I correct for this by adding one grid constant to the arc length from (b) to (c) to obtain the image length, and four grid constants to the sum of the distances of the boundary points to find the image perimeter. This is also shown in

Fig. 5.2. I found that these new corrections further reduce the weak dependence of the lensing cross section on the resolution of the grid used for its computation.

The image area is calculated directly from the number of image points. As discussed in [72], a simple geometric figure is searched (ellipse, circle, rectangle or ring) with equal area and length to determine the image width W, which is approximated by the minor axis of the ellipse, the diameter of the circle, the smaller side of the rectangle or the width of the ring, respectively. The type of the figure is chosen by comparing its circumference to the actual perimeter of the image, which I find using the method discussed above.

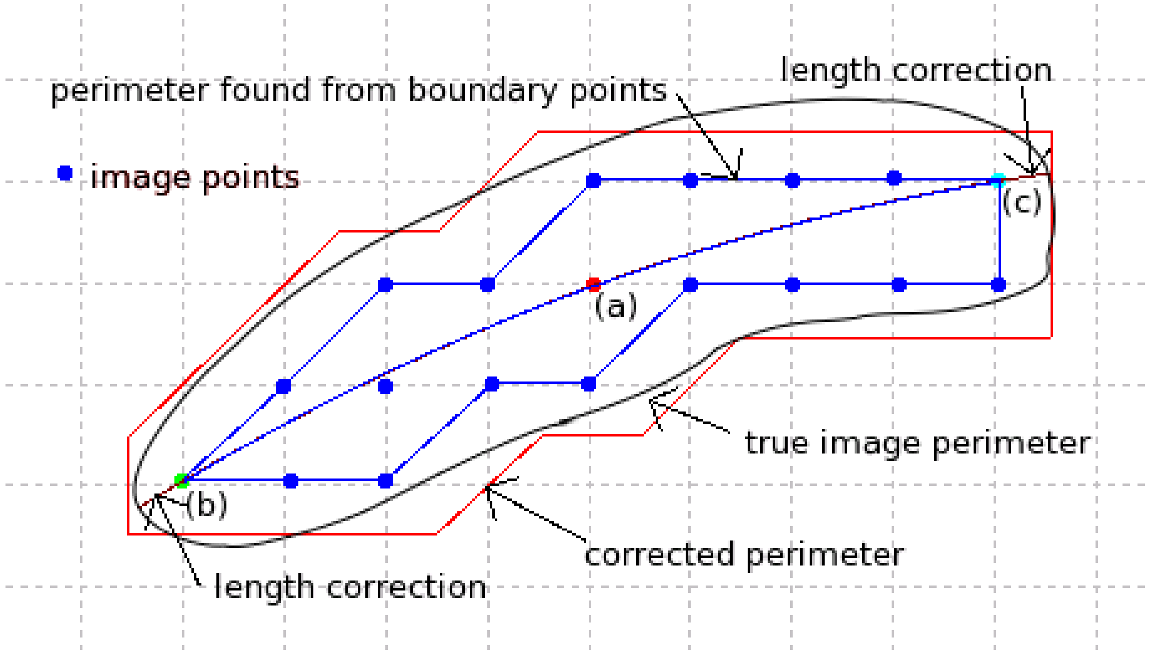

Figure 5.2: Correction of image length and perimeter.

I finally determine the lensing cross section $\sigma_{7.5}$ by summing up the statistical weights of the sources having images with a length-to-width ratio $L/W \geq 7.5$ and calculating the comoving area in the source plane corresponding to them. If there is more than one such image for a source, I multiply the statistical weight of this source by the number of these images.

5.3.3 A comparison of strong lensing cross sections

I used the method discussed above to find the strong-lensing cross sections of the clusters *g1*, *g8*, *g51*, *g72*, and of the three largest halos in the super-cluster simulation *g696*. I did this for 43 simulation snapshots with redshifts ranging between 0.1 and 1.05, and for the five different physical gas models discussed in Sect. 2.3, except for *g696*, for which only DM and GAS simulations were available. For each halo, I used three different projections, namely along the x, y and z axes of the simulation boxes in which the clusters are randomly oriented.

In Fig. 5.3, I plot the cross section as a function of redshift for one of the projections of *g51*. One can see that despite the gas pressure, adiabatic gas with the standard artificial viscosity does not reduce the strong lensing cross section compared to the dark-matter-only simulation. Using the new artificial viscosity scheme, however, leads to somewhat smaller cross sections due to the more extended gas distribution it implies. On the other hand, cooling, star formation and feedback make the simulated cluster a significantly more efficient lens. These three properties are typical for most of the clusters I have studied. There is generally no large difference between the DM and (adiabatic) GAS models, a somewhat smaller cross section in the GAS_NV model, and cross sections larger by a factor of 1.5 to 3 in the CSF and CSFC models. In some cases, however, even the adiabatic gas with standard artificial viscosity causes an *increase* in the cross section compared to the simulations containing only dark matter. This is illustrated in Fig. 5.4.

For determining the impact of cluster ellipticity and substructure on the strong lensing cross sections, I transform the maps of the surface mass density of the cluster halos to polar coordinates (centred on the cluster halo) and average over the polar

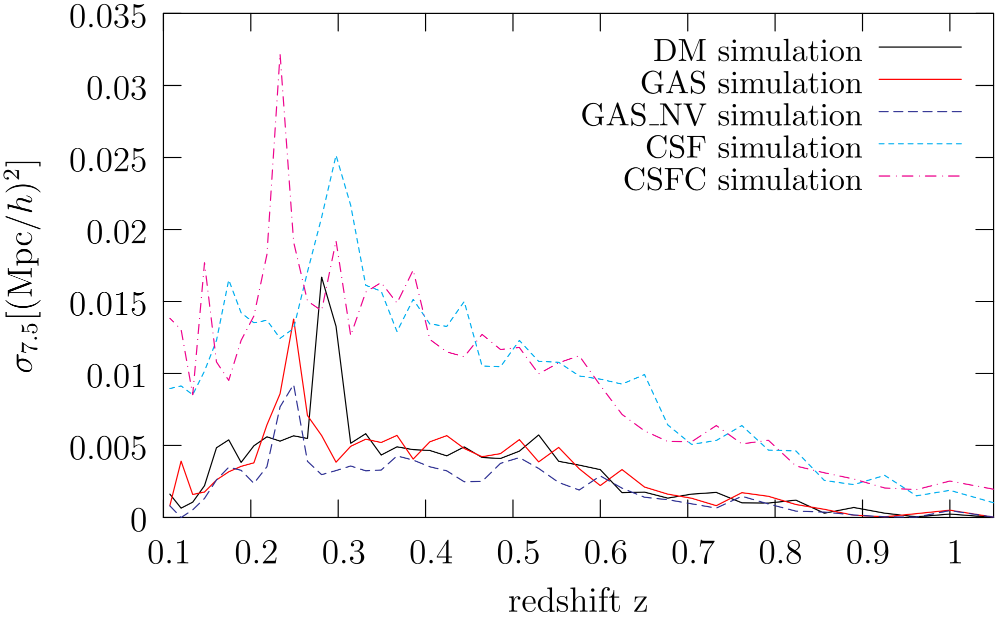

Figure 5.3: Strong lensing cross sections for the projection along the y axis of the DM, GAS, GAS_NV, CSF, and CSFC simulations of cluster *g51*, for an arc length-to-width ratio of 7.5 or more. The units are comoving $(\mathrm{Mpc}/h)^2$.

angle to obtain maps of an axially symmetrised cluster. Then, I use the same methods as before to compute strong-lensing cross sections.

Figure 5.5 shows the cross sections of the GAS and CSF versions of *g51* and of its axially-symmetrised GAS and CSF counterparts. One can clearly see that substructure and ellipticity significantly increase the strong-lensing cross sections (see also Sect. 5.1). Note also that the increase of the cross section in the CSF simulation, compared to the GAS simulation, is almost the same for the original cluster and its axially-symmetric variant. This can be interpreted such that this increase in the cross section in the cooling and star formation simulations is caused mainly by the steeper density profile (see Fig. 2.1) and not by any changes of the ellipticity or the substructure.

There is also no qualitative difference between the lensing properties of the simu-

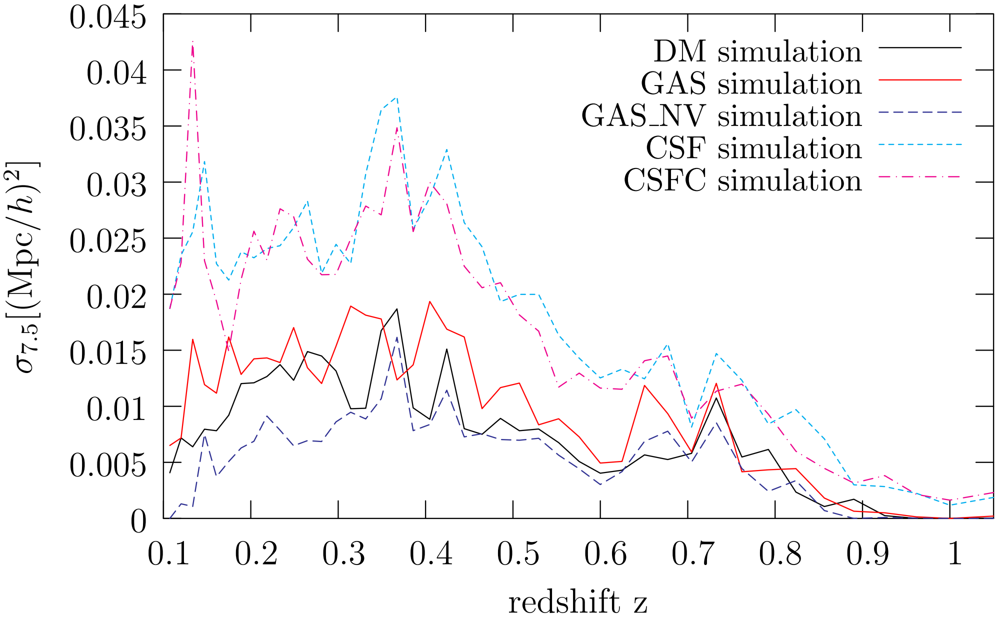

Figure 5.4: Strong lensing cross section for the DM, GAS, GAS_NV, CSF, and CSFC simulation of cluster *g1* and an arc length-to-width ratio of ≥ 7.5.

lated clusters and the largest halos of the simulated super cluster region.

The different physics in the simulations with only dark matter particles compared to simulations including gas directs sub-halos passing close to the main halo during a merger into different orbits. Compared to the dissipation-less simulation with only dark matter, the sub-halo loses angular momentum and energy in the gas-dynamical simulations and is directed into a less elliptical orbit. It therefore returns earlier for the next passage of the main halo's centre. This is illustrated in Fig. 5.6, which shows the position of a sub-halo in the rest frame of the main halo of the cluster *g72*. Note that the x and y axes are scaled differently for clarity. The sub-halos in the DM and GAS simulations initially move approximately synchronously and approach the main halo with almost the same velocity. Later, however, the different dynamics makes the GAS sub-halo's orbit substantially less elliptical, hence it returns earlier for the next core passage.

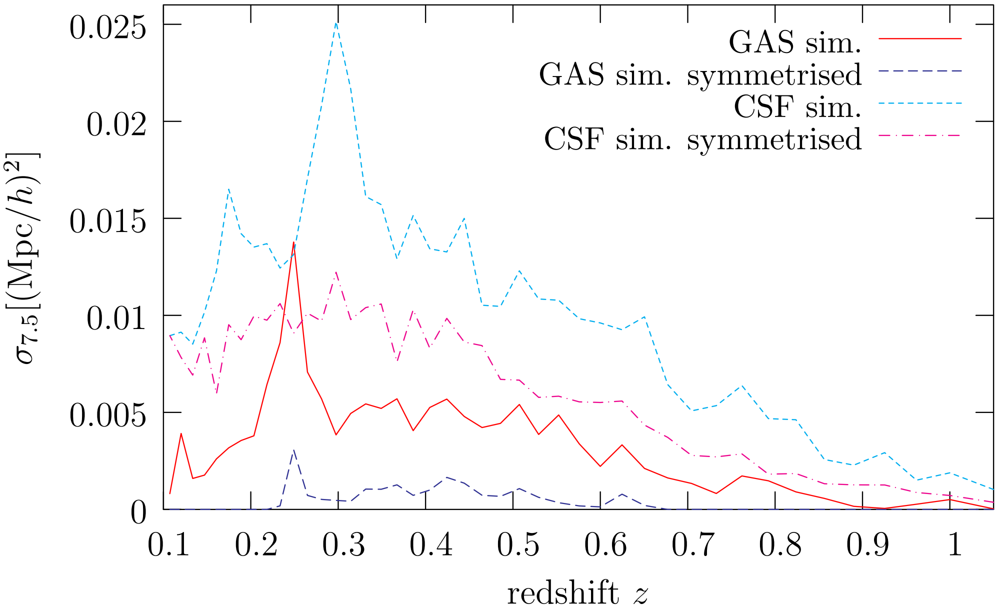

Figure 5.5: Strong lensing cross sections for the GAS, CSF, and axially-symmetrised GAS and CSF versions of cluster *g51*.

This effect also has an impact on the strong lensing cross section, because the cross section of a halo increases when a sub-halo crosses the cluster core during a merger (see discussion in Sect. 5.1). In Fig. 5.7, the peaks in the cross section corresponding to the three successive passages, illustrated in Fig. 5.6, are marked by arrows for both the DM and the GAS simulations. The first peak happens in both cases at a redshift $z \approx 0.62$. The second and the third peaks, however, occur at significantly earlier times in the GAS simulation. The peak positions for the GAS_NV, CSF, and CSFC simulations are typically very similar to the GAS case. Note that the different heights of the first peak in the different simulations do not imply a fundamental difference, because the amplitude of sharp peaks depends strongly on the exact time when the snapshot was taken (the time resolution is just a few snapshots for the passage). Thus, a slight deviation in the timing may result in peaks with apparently very different heights.

Since this analysis was published [99], there were two subsequent studies of the impact of baryon cooling on strong cluster lensing. My result that cooling can significantly increase strong lensing cross sections was confirmed [104]. The cluster sample used there extends to lower mass systems, whose lensing efficiencies were shown to be also boosted by cooling. Using a semi-analytic technique to model the effects of baryon cooling in dark matter N-body simulations, it was shown that the number of giant arcs and lensed quasars increases and that multiple image systems are $\sim 25\%$ more abundant when including the effects of baryon cooling [132].

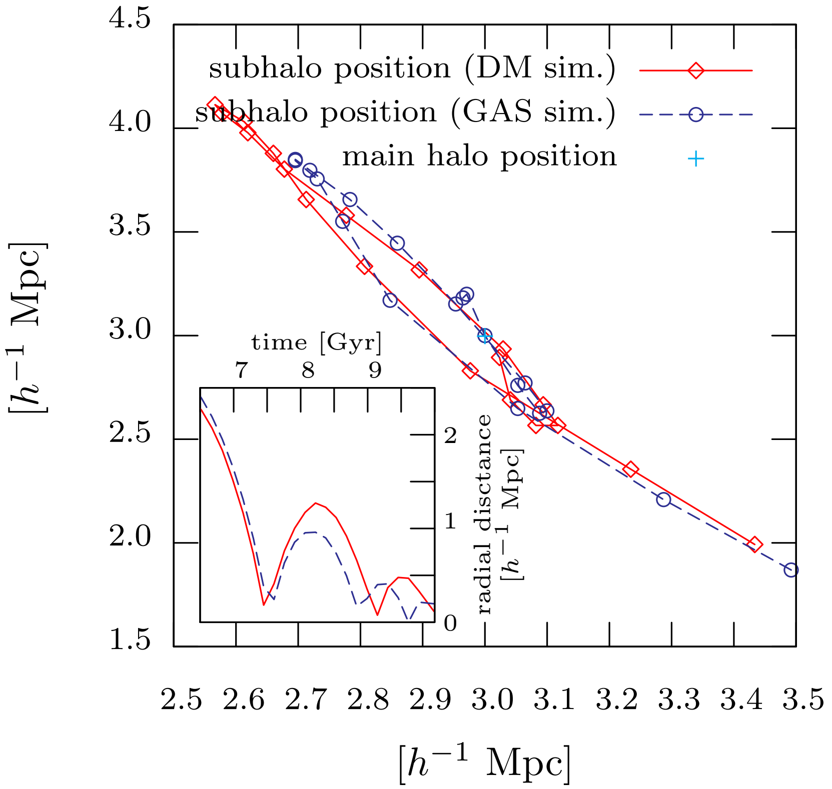

Figure 5.6: Position (in the main halo's rest frame and in comoving coordinates) and radial distance from the main halo of the sub-halo whose passage produces the peaks in cluster *g72*'s lensing cross section for the DM and GAS case.

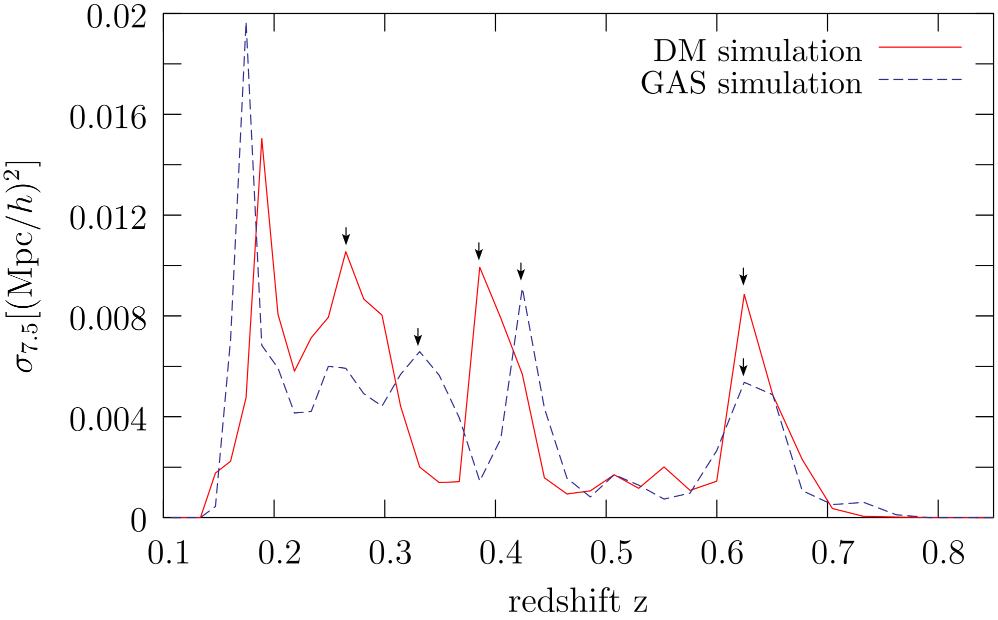

Figure 5.7: Strong-lensing cross section for the DM and GAS simulations of cluster *g72* and a length-to-width ratio of 7.5 or more. The arrows mark the three successive passages of the same sub-halo for both models.

Chapter 6

Summary and Conclusions

I summarised the state of the scientific exploration of the structure of galaxy clusters and presented two new studies, namely, I proposed and tested a novel method to model galaxy clusters by a joint analysis of X-ray, thermal Sunyaev-Zel'dovich (SZ) effect and lensing observations (Sects. 3.5 - 3.8), and I investigated and quantified the impact of baryonic physics on strong cluster lensing (Sect. 5.3) and cluster structure (Sects. 2.3 - 2.4). The main results of these studies are discussed in the next two sections.

6.1 Modelling clusters based on X-ray, thermal Sunyaev-Zel'dovich and lensing observations

I proposed a novel method for three-dimensional cluster modelling by a joint analysis of X-ray, thermal SZ and lensing data. It is based on iterative Richardson-Lucy deconvolution and assumes only axial, rather than spherical symmetry of the cluster halo. The symmetry axis can be arbitrarily inclined with respect to the line-of-sight. Using X-ray surface brightness and thermal SZ data it allows simultaneously reconstructing the three-dimensional cluster gas density and temperature distributions, requiring no equilibrium assumption other than local thermal equilibrium.

From these cluster gas reconstructions, either cumulative total mass profiles and reconstructions of the three-dimensional gravitational potential can be obtained by then assuming hydrostatic equilibrium, or alternatively, hydrostatic equilibrium can be quantitatively probed by comparing cumulative mass profiles obtained in this way to profiles found by an analysis of lensing data.

In the lensing analysis, Richardson-Lucy deconvolution is used to deproject the lensing potential, which can be obtained from weak lensing or a combination of weak and strong lensing observations. This yields an independent reconstruction of the three-dimensional gravitational potential, from which I then derive cumulative mass profiles. Differences between lensing and combined X-ray and SZ (abbreviated by XSZ) cumulative mass profiles directly reflect deviations from the hydrostatic equilibrium condition.

Thus, if only X-ray and thermal SZ data are available accurate reconstructions of relaxed clusters can be obtained. If, however, lensing data is available as well, hydrostatic equilibrium can be probed, also in dynamically active clusters, by comparing these independent reconstructions.

These methods were tested with synthetic observations of analytically modelled and numerically simulated clusters. I studied the impact of realistic observational noise, deviations from axial symmetry and cluster substructure on reconstruction accuracy.

6.1.1 Numerical tests of the gas reconstruction algorithm

For numerically simulated clusters which are of course not strictly axisymmetric, I use one of the principal inertial axes as the "symmetry" axis for the deprojection. Assuming that the inclination angle between the symmetry axis and the line-of-sight is known, my main findings from applying the cluster gas reconstruction algorithm to synthetic data are:

- Spike-shaped artefacts of the deprojection, which can appear when using Richardson-Lucy deconvolution to deproject strongly peaked axisymmetric distributions, are efficiently suppressed by the regularisation scheme that I apply to the iterative corrections.
- Densities and temperatures of the ICM of axisymmetric analytic clusters can be reconstructed very accurately from X-ray surface brightness and Sunyaev-Zel'dovich temperature decrement maps. Errors are of the order of 1% when using idealised noise-free synthetic observation, unless the angle between the symmetry axis and the line-of-sight is very small. When using maps that contain realistic observational noise, relative errors are still only about 5% to 10%.
- The three-dimensional density and temperature distributions of hot gas in numerically simulated clusters, although not strictly axisymmetric, can be reliably reconstructed. Relative errors reach about 10% when using noise-free data and roughly 15% when including realistic noise.
- Smoothing of the X-ray surface brightness and the Sunyaev-Zel'dovich temperature decrement maps can suppress artefacts caused by subclumps and noise.
- Accurate gas density and temperature profiles can be obtained from the reconstructions.

- Five iterations are sufficient for the ICM deprojection. Using a larger number does not increase the quality of the reconstructions under realistic conditions.

For these deprojections I assumed that the inclination angle between the symmetry axis and the line-of-sight is known beforehand. This will typically not be the case when applying these methods to real observations. I showed that the symmetry axis' inclination can be best constrained by additional data which are independent of the X-ray surface brightness and the SZ maps that the gas reconstructions are based on, like high-quality X-ray temperature maps. The inclination angle is found by deprojecting the cluster gas assuming different values of the inclination angle, then reprojecting the reconstructed gas distributions to get temperature maps of the reconstructed clusters and finding the value of the inclination angle for which this map best matches the observed temperature map. This allows constraining the inclination angle of a cluster's symmetry axis to values for which the quality of the reconstruction is close to its optimum.

6.1.2 Numerical tests of mass and potential reconstructions and of methods to probe hydrostatic equilibrium

I proposed a novel method to obtain three-dimensional reconstructions of a galaxy cluster's gravitational potential and cumulative mass profile from X-ray and thermal SZ observations under the assumption of hydrostatic equilibrium, and independently and dropping this assumption from lensing data.

These methods were tested with synthetic X-ray, thermal SZ and lensing observations of analytically modelled and numerically simulated galaxy clusters. The impact of realistic observational noise was studied.

For analytically modelled clusters in hydrostatic equilibrium I found:

- Consistent and accurate lensing and XSZ based cumulative mass profiles $M_{<r,\,\mathrm{lensing}}(r)$ and $M_{<r,\,\mathrm{XSZ}}(r)$ can be obtained.

- The accuracy somewhat decreases for very small inclination angles between the line-of-sight and the cluster's symmetry axis.

- Higher accuracy for the iterative deprojection of the lensing potential for small inclination angles is achieved by starting the iteration from spherically symmetrised priors for the three-dimensional gravitational potential.

- Faithful three-dimensional reconstructions of the gravitational potential can be obtained from both lensing observations and from an XSZ analysis.

For analytically modelled clusters that are not in hydrostatic equilibrium, I showed that the deviations from equilibrium can be effectively probed by a comparison of lensing and XSZ reconstructions even when realistic observational noise is present.

From reconstructions based on synthetic observations of a sample of numerically simulated galaxy clusters I conclude:

- For clusters that did not experience recent mergers, consistent and accurate lensing and XSZ cumulative mass profiles are found.

- Although these clusters are not perfectly axisymmetric and noise is added to the synthetic data, the accuracy of reconstructed cumulative mass profiles is typically better than 10 to 15% for both the X-ray, SZ and the lensing reconstructions.

- On the other hand in clusters in the process of merging deviations from hydrostatic equilibrium can be accurately probed, except for cases where the relevant merging subhalo appears directly in front of or behind the main halo's centre.

6.2 How does cluster gas affect strong lensing and halo structure?

I compared the density profiles, shapes, and strong lensing properties of numerically simulated galaxy clusters. Simulations that were started from the same initial conditions, but employed different gas physics models were used. The simulations were performed by Klaus Dolag (MPA Garching) with the GADGET-2 code. Five different physical gas-models were employed. They contain:

- DM model: dark matter only;
- GAS model: dark matter and adiabatic gas;
- GAS_NV model: dark matter, adiabatic gas, and a new implementation of the artificial viscosity, reducing the viscosity where it is not numerically needed;
- CSF model: dark matter, cooling gas, a star formation model, and feedback;
- CSFC model: dark matter, cooling gas, a star formation model, feedback, and thermal conductivity;

The cluster sample consisted of four simulated galaxy clusters and the three largest halos of a simulation of a super-cluster region. I used 43 snapshots of these halos between redshifts 1.05 and 0.1. For studying strong lensing, I used the three different projections along the coordinate axes of the simulation volume, and sources fixed at redshift 1.5.

I find significantly steeper inner slopes for the density profiles of halos simulated with cooling and star formation. On the other hand, adiabatic gas with a standard artificial viscosity, in spite of its isotropic thermal pressure, does not make density profiles shallower compared to the dissipation-less dark-matter simulations. This can be understood from the fact that gas can reduce its specific angular momentum by collisions. The orbits of gas clumps in a cluster halo are essentially randomly oriented. Collisions tend to average out these differences and thereby reduce the specific angular momentum of the gas, which helps the gas to move towards the cluster centre. On the other hand, the additional pressure caused by strong turbulence in the GAS_NV simulation can somewhat reduce the density close to the cluster centre.

I then performed ray-tracing simulations for the numerically simulated galaxy clusters to study their strong lensing properties. I calculated cross sections for long thin arcs with a length-to-width ratio equal to or larger than 7.5. For the simulations with cooling and star formation, I found significantly larger cross sections. They typically increased by a factor of 1.5 to 3 compared to dark-matter-only simulations or simulations with adiabatic gas. Thermal conductivity has no big impact on strong lensing. Despite its pressure, adiabatic gas with standard artificial viscosity does not reduce the cross section for long thin arcs. In some cases, it even makes the cluster a more efficient lens. On the other hand, simulating adiabatic gas with the new scheme for reduced artificial viscosity leads to somewhat smaller strong lensing cross sections compared to the DM and GAS runs.

Note that despite the used state-of-the-art model for cooling, star formation, and feedback, the simulated clusters suffer from some over-cooling. Therefore, the density close to the centre and the increase of the strong lensing cross section may be over-predicted in the simulations with cooling and star formation compared to real clusters. Also, the impact of turbulence on galaxy clusters needs further investigation. In real clusters, the physical viscosity of the cluster gas, which is not yet included in simulations, will regulate turbulence and may lead to a smaller amount of turbulence than in the GAS_NV simulations. It will also be interesting to investigate the effect of this new scheme of artificial viscosity on simulations including cooling, star formation, and feedback.

To study the impact of ellipticity and substructure on the lensing properties I transformed maps of the surface mass density of the cluster halos to polar coordinates and averaged over the angle, so that I obtained maps of an azimuthally symmetrised halo. I compared the cross sections of these axially symmetrised clusters to those of the numerically simulated ones and found that ellipticity and substructure are important for strong lensing in all of the five gas physical models. However, their impact on the cross section turns out to be very similar in the simulations without and with cooling and star formation. Thus, the larger cross sections I obtained for simulations with cooling and star formation are mainly caused by the steeper density profile and not by changes in ellipticity and substructure.

Sub-halos passing close to the main halo lose angular momentum and energy and are directed into less elliptical orbits in simulations with gas compared to dark-matter-only simulations. During a merger, such a sub-halo will return at an earlier time for the next passage. Thus, mergers proceed faster in simulations with gas. This can also be seen in the strong lensing cross sections: typically, the peak corresponding to the first passage of a sub-halo happens at the same time in the dissipation-less and the gas-dynamical simulations, but the peaks corresponding to the next passages are shifted to earlier times in the simulations with gas.

The work presented here clearly shows that baryons can have a significant impact on strong lensing cross sections and halo structure. However, the importance of the different effects (turbulence, cooling, star formation, mergers) is different for each individual cluster and changes during the cluster's evolution. To infer cluster properties from observations and for studying the importance of these effects in real clusters, it is thus more promising to model observed clusters individually than to do statistical analyses of large cluster samples.

Acknowledgments

First and foremost, I would like to thank Matthias for suggesting my thesis projects and for supervising them in a very friendly, competent and motivating way. I am also deeply indebted to him for countless hours of illuminating discussion and for always trying hard to find time for them, even when his appointment schedule was completely full. Furthermore, I am very grateful to him for his efforts to create a good working atmosphere, for his advice on many things not related to my thesis, and especially for his help with my postdoc applications.

I am also very grateful to Klaus Dolag for providing me access to the numerical cluster simulations that were used throughout this work as well as for many interesting discussions about them.

Next, I would like to thank Massimo for generously allowing me to use and modify his ray-tracing code as well as for many useful discussions about gravitational lensing and galaxy clusters. Also, thanks for writing the letter of recommendation for me!

I am, further, very grateful to Prof. Dr. Grebel for refereeing my thesis and agreeing to participate in my Ph.D. exam. For the latter reason, I would also like to thank Prof. Dr. Wambsganß and Prof. Dr. Camenzind.

I am also indebted to Elena Rasia for giving me access to the X-ray map simulator XMAS and an introduction to using it, as well as to Robert Schmidt for an introduction to Chandra data analysis.

I acknowledge support by the German Science Foundation under grant number BA 1369/6-1 within the framework program SPP 1177.

Then, I would like to thank all my colleagues for many interesting and amusing discussions about cosmology, galaxy clusters, gravitational lensing, SPH, Gadget, lots of other astrophysical topics, C++ (mostly Emanuel and Gregor), Linux, Latex, Fortran (Francesco and Massimo), science and computers in general, politics, food and eating (mostly with or about Ciccio, ...), cycling (Francesco, Irina, Massimo, Matthias, ...), photography (Jean-Claude and Peter), movies, skiing (Matteo, Peter, ...), other sports (Irina, Francesco, Julian, Peter, Emanuel, Martin, Christian, ...), university bureaucracy, career, weather, Italian lifestyle (Francesco, Cosimo, Claudia, Massimo, Matteo, Marcello + everybody else), where to have lunch, Ph.D. comics, time of day (with a special colleague, “So long, and thanks for all the bread!”), ...

Further, I want to thank Francesco for not using his powers on my computer too often and Emanuel for fixing it, if he did.

I also greatly enjoyed the barbecues, bike tours (Francesco, Irina, Massimo, Emanuel, Gregor, Svetlana, ...), swimming (Francesco (trying hard), Irina, Massimo, Ana), skiing (Matteo), pub tours, going to the movies, travelling to and participating in schools and conferences (Francesco, Cosimo, Irina, Matteo, Matthias), and lots of other activities with my colleagues. Thanks a lot to all of you!

It is my utmost pleasure to thank Janna for her love and affection, for her support, for cheering me up when things went not so smooth, and for the wonderful time I have with her.

And last but definitely not least, I am very grateful to my parents and my family for their love and support during all my studies.

Bibliography

[1] B. Allgood, R. A. Flores, J. R. Primack, A. V. Kravtsov, R. H. Wechsler, A. Faltenbacher, and J. S. Bullock. The shape of dark matter haloes: dependence on mass, redshift, radius and formation. MNRAS, 367:1781–1796, April 2006.

[2] S. Ameglio, S. Borgani, E. Pierpaoli, and K. Dolag. Joint deprojection of Sunyaev-Zeldovich and X-ray images of galaxy clusters . *in preparation*, 2007.

[3] J. S. Arabadjis, M. W. Bautz, and G. P. Garmire. Chandra Observations of the Lensing Cluster EMSS 1358+6245: Implications for Self-interacting Dark Matter. ApJ, 572:66–78, June 2002.

[4] K. A. Arnaud. XSPEC: The First Ten Years. In G. H. Jacoby and J. Barnes, editors, *Astronomical Data Analysis Software and Systems V*, volume 101 of *Astronomical Society of the Pacific Conference Series*, pages 17–+, 1996.

[5] J. S. Bagla. TreePM: A Code for Cosmological N-Body Simulations. *Journal of Astrophysics and Astronomy*, 23:185–196, December 2002.

[6] N. A. Bahcall, T. A. McKay, J. Annis, R. S. J. Kim, F. Dong, S. Hansen, T. Goto, J. E. Gunn, C. Miller, R. C. Nichol, M. Postman, D. Schneider, J. Schroeder, W. Voges, J. Brinkmann, and M. Fukugita. A Merged Catalog of Clusters of Galaxies from Early Sloan Digital Sky Survey Data. ApJS, 148:243–274, October 2003.

[7] D. S. Balsara. von Neumann Stability Analysis of Smoothed Particle Hydrodynamics - Suggestions for Optimal Algorithms. *J. Comp. Phys.*, 121:357–372, 1995.

[8] J. Barnes and P. Hut. A Hierarchical O(NlogN) Force-Calculation Algorithm. Nature, 324:446–449, December 1986.

[9] M. Bartelmann. *Cosmology, lecture notes.* ZAH, Heidelberg, http://www.ita.uni-heidelberg.de/∼msb/Lectures/cosmology/cosmology.pdf.

[10] M. Bartelmann, A. Huss, J. M. Colberg, A. Jenkins, and F. R. Pearce. Arc statistics with realistic cluster potentials. IV. Clusters in different cosmologies. A&A, 330:1–9, February 1998.

[11] M. Bartelmann, M. Meneghetti, F. Perrotta, C. Baccigalupi, and L. Moscardini. Arc statistics in cosmological models with dark energy. A&A, 409:449–457, October 2003.

[12] M. Bartelmann and M. Steinmetz. A Comparison of X-ray and Strong Lensing Properties of Simulated X-ray Clusters. MNRAS, 283:431–446, November 1996.

[13] M. Bartelmann, M. Steinmetz, and A. Weiss. Arc statistics with realistic cluster potentials. 2: Influence of cluster asymmetry and substructure. A&A, 297:1–12, May 1995.

[14] M. Bartelmann and A. Weiss. Arc statistics with realistic cluster potentials. 1: Method and first results. A&A, 287:1–14, July 1994.

[15] J. J. Binney, R. L. Davies, and G. D. Illingworth. Velocity mapping and models of the elliptical galaxies NGC 720, NGC 1052, and NGC 4697. ApJ, 361:78–97, September 1990.

[16] M. Birkinshaw, S. F. Gull, and H. Hardebeck. The Sunyaev-Zeldovich effect towards three clusters of galaxies. Nature, 309:34–35, May 1984.

[17] J. R. Bond, S. Cole, G. Efstathiou, and N. Kaiser. Excursion set mass functions for hierarchical Gaussian fluctuations. ApJ, 379:440–460, October 1991.

[18] S. Borgani, P. Rosati, P. Tozzi, S. A. Stanford, P. R. Eisenhardt, C. Lidman, B. Holden, R. Della Ceca, C. Norman, and G. Squires. Measuring Omega_m with the ROSAT Deep Cluster Survey. ApJ, 561:13–21, November 2001.

[19] B. Butler and A. Wootten. ALMA Sensitivity, Supra-THz Windows and 20 km baselines. *ALMA Memo 276, http://www.alma.nrao.edu/memos/html-memos/abstracts/abs276.html*, October 1999.

[20] M. Cacciato, M. Bartelmann, M. Meneghetti, and L. Moscardini. Combining weak and strong lensing in cluster potential reconstruction. A&A, 458:349–356, November 2006.

[21] A. Cavaliere and R. Fusco-Femiano. X-rays from hot plasma in clusters of galaxies. A&A, 49:137–144, May 1976.

[22] C. Clarkson, M. Cortes, and B. A. Bassett. Dynamical Dark Energy or Simply Cosmic Curvature? *ArXiv Astrophysics e-prints*, astro-ph/0702670, February 2007.

[23] S. Cole and C. Lacey. The structure of dark matter haloes in hierarchical clustering models. MNRAS, 281:716–+, July 1996.

[24] N. Dalal, G. Holder, and J. F. Hennawi. Statistics of Giant Arcs in Galaxy Clusters. ApJ, 609:50–60, July 2004.

[25] E. De Filippis, M. Sereno, M. W. Bautz, and G. Longo. Measuring the Three-dimensional Structure of Galaxy Clusters. I. Application to a Sample of 25 Clusters. ApJ, 625:108–120, May 2005.

[26] K. Dolag, F. Vazza, G. Brunetti, and G. Tormen. Turbulent gas motions in galaxy cluster simulations: the role of smoothed particle hydrodynamics viscosity. MNRAS, 364:753–772, December 2005.

[27] O. Doré, F. R. Bouchet, Y. Mellier, and R. Teyssier. Cluster physics from joint weak gravitational lensing and Sunyaev-Zel'dovich data. A&A, 375:14–24, August 2001.

[28] G. Efstathiou, M. Davis, S. D. M. White, and C. S. Frenk. Numerical techniques for large cosmological N-body simulations. ApJS, 57:241–260, February 1985.

[29] S. Ettori. Are we missing baryons in galaxy clusters? MNRAS, 344:L13–L16, September 2003.

[30] S. Ettori, S. De Grandi, and S. Molendi. Gravitating mass profiles of nearby galaxy clusters and relations with X-ray gas temperature, luminosity and mass. A&A, 391:841–855, September 2002.

[31] A. E. Evrard. The intracluster gas fraction in X-ray clusters - Constraints on the clustered mass density. MNRAS, 292:289–+, December 1997.

[32] A. E. Evrard, T. J. MacFarland, H. M. P. Couchman, J. M. Colberg, N. Yoshida, S. D. M. White, A. Jenkins, C. S. Frenk, F. R. Pearce, J. A. Peacock, and P. A. Thomas. Galaxy Clusters in Hubble Volume Simulations: Cosmological Constraints from Sky Survey Populations. ApJ, 573:7–36, July 2002.

[33] Y. Fukazawa, K. Makishima, T. Tamura, H. Ezawa, H. Xu, Y. Ikebe, K. Kikuchi, and T. Ohashi. ASCA Measurements of Silicon and Iron Abundances in the Intracluster Medium. PASJ, 50:187–193, February 1998.

[34] T. Fukushige and J. Makino. Structure of Dark Matter Halos from Hierarchical Clustering. ApJ, 557:533–545, August 2001.

[35] R. A. Gingold and J. J. Monaghan. Smoothed particle hydrodynamics - Theory and application to non-spherical stars. MNRAS, 181:375–389, November 1977.

[36] M. Girardi, S. Borgani, G. Giuricin, F. Mardirossian, and M. Mezzetti. The Observational Mass Function of Nearby Galaxy Clusters. ApJ, 506:45–52, October 1998.

[37] H. Gursky, E. Kellogg, S. Murray, C. Leong, H. Tananbaum, and R. Giacconi. A Strong X-Ray Source in the Coma Cluster Observed by UHURU. ApJ, 167:L81–+, August 1971.

[38] Z. Haiman, J. J. Mohr, and G. P. Holder. Constraints on Cosmological Parameters from Future Galaxy Cluster Surveys. ApJ, 553:545–561, June 2001.

[39] E. J. Hallman, P. M. Motl, J. O. Burns, and M. L. Norman. Challenges for Precision Cosmology with X-Ray and Sunyaev-Zeldovich Effect Gas Mass Measurements of Galaxy Clusters. ApJ, 648:852–867, September 2006.

[40] E. Holmberg. On the Clustering Tendencies among the Nebulae. II. a Study of Encounters Between Laboratory Models of Stellar Systems by a New Integration Procedure. ApJ, 94:385–+, November 1941.

[41] N. Itoh, S. Kusano, T. Sakamoto, and S. Nozawa. Relativistic Thermal Bremsstrahlung Gaunt Factor for the Intracluster Plasma. III. Frequency Integrated Emissivity. *ArXiv Astrophysics e-prints*, astro-ph/0011044, November 2000.

[42] A. Jenkins, C. S. Frenk, S. D. M. White, J. M. Colberg, S. Cole, A. E. Evrard, H. M. P. Couchman, and N. Yoshida. The mass function of dark matter haloes. MNRAS, 321:372–384, February 2001.

[43] Y. P. Jing and Y. Suto. Triaxial Modeling of Halo Density Profiles with High-Resolution N-Body Simulations. ApJ, 574:538–553, August 2002.

[44] M. Jubelgas, V. Springel, and K. Dolag. Thermal conduction in cosmological SPH simulations. MNRAS, 351:423–435, June 2004.

[45] J. S. Kaastra and R. Mewe. *Legacy*, 3:16, January 1993.

[46] N. Kaiser and G. Squires. Mapping the dark matter with weak gravitational lensing. ApJ, 404:441–450, February 1993.

[47] S. Kazantzidis, A. V. Kravtsov, A. R. Zentner, B. Allgood, D. Nagai, and B. Moore. The Effect of Gas Cooling on the Shapes of Dark Matter Halos. ApJ, 611:L73–L76, August 2004.

[48] I. R. King. Density Data and Emission Measure for a Model of the Coma Cluster. ApJ, 174:L123+, June 1972.

[49] J.-P. Kneib, P. Hudelot, R. S. Ellis, T. Treu, G. P. Smith, P. Marshall, O. Czoske, I. Smail, and P. Natarajan. A Wide-Field Hubble Space Telescope Study of the Cluster Cl 0024+1654 at z=0.4. II. The Cluster Mass Distribution. ApJ, 598:804–817, December 2003.

[50] A. V. Kravtsov, D. Nagai, and A. A. Vikhlinin. Effects of Cooling and Star Formation on the Baryon Fractions in Clusters. ApJ, 625:588–598, June 2005.

[51] G. A. Kriss, D. F. Cioffi, and C. R. Canizares. The X-ray emitting gas in poor clusters with central dominant galaxies. ApJ, 272:439–448, September 1983.

[52] J. Lee and Y. Suto. Reconstructing the Three-dimensional Structure of Underlying Triaxial Dark Halos from X-Ray and Sunyaev-Zel'dovich Effect Observations of Galaxy Clusters. ApJ, 601:599–609, February 2004.

[53] E. S. Levine, A. E. Schulz, and M. White. Future Galaxy Cluster Surveys: The Effect of Theory Uncertainty on Constraining Cosmological Parameters. ApJ, 577:569–578, October 2002.

[54] A. D. Lewis, D. A. Buote, and J. T. Stocke. Chandra Observations of A2029: The Dark Matter Profile Down to below 0.01 r_vir in an Unusually Relaxed Cluster. ApJ, 586:135–142, March 2003.

[55] G. F. Lewis, A. Babul, N. Katz, T. Quinn, L. Hernquist, and D. H. Weinberg. The Effects of Gasdynamics, Cooling, Star Formation, and Numerical Resolution in Simulations of Cluster Formation. ApJ, 536:623–644, June 2000.

[56] G.-L. Li, S. Mao, Y. P. Jing, M. Bartelmann, X. Kang, and M. Meneghetti. Is the Number of Giant Arcs in ΛCDM Consistent with Observations? ApJ, 635:795–805, December 2005.

[57] G. L. Li, S. Mao, Y. P. Jing, H. J. Mo, L. Gao, and W. P. Lin. The giant arc statistics in the three-year Wilkinson Microwave Anisotropy Probe cosmological model. MNRAS, 372:L73–L77, October 2006.

[58] D. A. Liedahl, A. L. Osterheld, and W. H. Goldstein. New calculations of Fe L-shell X-ray spectra in high-temperature plasmas. ApJ, 438:L115–L118, January 1995.

[59] L. B. Lucy. An iterative technique for the rectification of observed distributions. AJ, 79:745–+, June 1974.

[60] L. B. Lucy. Optimum strategies for inverse problems in statistical astronomy. A&A, 289:983–994, September 1994.

[61] A. Mahdavi, H. Hoekstra, A. Babul, J. Sievers, S. T. Myers, and J. P. Henry. Joint Analysis of Cluster Observations. I. Mass Profile of Abell 478 from Combined X-Ray, Sunyaev-Zel'dovich, and Weak-Lensing Data. ApJ, 664:162–180, July 2007.

[62] S. Majumdar and J. J. Mohr. Self-Calibration in Cluster Studies of Dark Energy: Combining the Cluster Redshift Distribution, the Power Spectrum, and Mass Measurements. ApJ, 613:41–50, September 2004.

[63] R. Mandelbaum and U. Seljak. A robust lower limit on the amplitude of matter fluctuations in the universe from cluster abundance and weak lensing. *Journal of Cosmology and Astro-Particle Physics*, 6:24–+, June 2007.

[64] R. Mandelbaum, U. Seljak, R. J. Cool, M. Blanton, C. M. Hirata, and J. Brinkmann. Density profiles of galaxy groups and clusters from SDSS galaxy-galaxy weak lensing. MNRAS, 372:758–776, October 2006.

[65] M. Markevitch, W. R. Forman, C. L. Sarazin, and A. Vikhlinin. The Temperature Structure of 30 Nearby Clusters Observed with ASCA: Similarity of Temperature Profiles. ApJ, 503:77–+, August 1998.

[66] J. C. Mather, E. S. Cheng, D. A. Cottingham, R. E. Eplee, Jr., D. J. Fixsen, T. Hewagama, R. B. Isaacman, K. A. Jensen, S. S. Meyer, P. D. Noerdlinger, S. M. Read, L. P. Rosen, R. A. Shafer, E. L. Wright, C. L. Bennett, N. W. Boggess, M. G. Hauser, T. Kelsall, S. H. Moseley, Jr., R. F. Silverberg, G. F. Smoot, R. Weiss, and D. T. Wilkinson. Measurement of the cosmic microwave background spectrum by the COBE FIRAS instrument. ApJ, 420:439–444, January 1994.

[67] P. Mazzotta, E. Rasia, L. Moscardini, and G. Tormen. Comparing the temperatures of galaxy clusters from hydrodynamical N-body simulations to Chandra and XMM-Newton observations. MNRAS, 354:10–24, October 2004.

[68] I. G. McCarthy, R. G. Bower, and M. L. Balogh. Revisiting the baryon fractions of galaxy clusters: a comparison with WMAP 3-yr results. MNRAS, 377:1457–1463, June 2007.

[69] M. Meneghetti, M. Bartelmann, K. Dolag, L. Moscardini, F. Perrotta, C. Baccigalupi, and G. Tormen. Strong lensing efficiency of galaxy clusters in dark energy cosmologies. A&A, 442:413–422, November 2005.

[70] M. Meneghetti, M. Bartelmann, A. Jenkins, and C. Frenk. The effects of ellipticity and substructure on estimates of cluster density profiles based on lensing and kinematics. *ArXiv Astrophysics e-prints*, astro-ph/0509323, September 2005.

[71] M. Meneghetti, M. Bartelmann, and L. Moscardini. Cluster cross-sections for strong lensing: analytic and numerical lens models. MNRAS, 340:105–114, March 2003.

[72] M. Meneghetti, M. Bolzonella, M. Bartelmann, L. Moscardini, and G. Tormen. Effects of cluster galaxies on arc statistics. MNRAS, 314:338–347, May 2000.

[73] J. Miralda-Escude. Statistics of highly magnified gravitational images in clusters of galaxies. I - Implications for the clusters. II - Implications for the sources. ApJ, 403:497–516, February 1993.

[74] J. Miralda-Escude. Statistics of Highly Magnified Gravitational Images in Clusters of Galaxies. II. Implications for the Sources. ApJ, 403:509–+, February 1993.

[75] J. J. Monaghan. Smoothed particle hydrodynamics. ARA&A, 30:543–574, 1992.

[76] J. J. Monaghan and R. A. Gingold. Shock Simulation by the Particle Method SPH . *J. Comp. Phys.*, 52:374–389, 1983.

[77] B. Moore, F. Governato, T. Quinn, J. Stadel, and G. Lake. Resolving the Structure of Cold Dark Matter Halos. ApJ, 499:L5–+, May 1998.

[78] J.P. Morris and J.J. Monaghan. *J. Comp. Phys.*, 136:41, 1997.

[79] R. Morrison and D. McCammon. Interstellar photoelectric absorption cross sections, 0.03-10 keV. ApJ, 270:119–122, July 1983.

[80] R. Narayan and M. Bartelmann. Lectures on Gravitational Lensing. *ArXiv Astrophysics e-prints*, astro-ph/9606001, June 1996.

[81] R. Narayan and M. V. Medvedev. Thermal Conduction in Clusters of Galaxies. ApJ, 562:L129–L132, December 2001.

[82] P. Natarajan and D. Lynden-Bell. An Analytic Approximation to the Isothermal Sphere. MNRAS, 286:268–270, April 1997.

[83] J. F. Navarro and W. Benz. Dynamics of cooling gas in galactic dark halos. ApJ, 380:320–329, October 1991.

[84] J. F. Navarro, C. S. Frenk, and S. D. M. White. Simulations of X-ray clusters. MNRAS, 275:720–740, August 1995.

[85] J. F. Navarro, C. S. Frenk, and S. D. M. White. The Structure of Cold Dark Matter Halos. ApJ, 462:563–+, May 1996.

[86] J. F. Navarro and S. D. M. White. Simulations of dissipative galaxy formation in hierarchically clustering universes - 2. Dynamics of the baryonic component in galactic haloes. MNRAS, 267:401–412, March 1994.

[87] M. L. Norman. The Impact of AMR in Numerical Astrophysics and Cosmology. *ArXiv Astrophysics e-prints*, astro-ph/0402230, February 2004.

[88] M. L. Norman and G. L. Bryan. Cosmological Adaptive Mesh Refinement. In S. M. Miyama, K. Tomisaka, and T. Hanawa, editors, *Astrophysics and Space Science Library*, volume 240 of *Astrophysics and Space Science Library*, pages 19–+, 1999.

[89] A. J. Oemler. The Systematic Properties of Clusters of Galaxies. Photometry of 15 Clusters. ApJ, 194:1–20, November 1974.

[90] M. Oguri, J. Lee, and Y. Suto. Arc Statistics in Triaxial Dark Matter Halos: Testing the Collisionless Cold Dark Matter Paradigm. ApJ, 599:7–23, December 2003.

[91] N. Ota, E. Pointecouteau, M. Hattori, and K. Mitsuda. Chandra Analysis and Mass Estimation of the Lensing Cluster of Galaxies Cl 0024+17. ApJ, 601:120–132, January 2004.

[92] T. Padmanabhan. *Structure formation in the universe*. Cambridge University Press, Cambridge, 1993.

[93] P. J. E. Peebles. Structure of the Coma Cluster of Galaxies. AJ, 75:13–+, February 1970.

[94] C. Power, J. F. Navarro, A. Jenkins, C. S. Frenk, S. D. M. White, V. Springel, J. Stadel, and T. Quinn. The inner structure of ΛCDM haloes - I. A numerical convergence study. MNRAS, 338:14–34, January 2003.

[95] G. W. Pratt and M. Arnaud. The mass profile of A1413 observed with XMM-Newton: Implications for the M-T relation. A&A, 394:375–393, November 2002.

[96] W. H. Press and P. Schechter. Formation of Galaxies and Clusters of Galaxies by Self-Similar Gravitational Condensation. ApJ, 187:425–438, February 1974.

[97] E. Puchwein and M. Bartelmann. Three-dimensional reconstruction of the intracluster medium. A&A, 455:791–801, September 2006.

[98] E. Puchwein and M. Bartelmann. Probing the dynamical state of galaxy clusters. *ArXiv e-prints*, 0706.0696 [astro-ph], June 2007.

[99] E. Puchwein, M. Bartelmann, K. Dolag, and M. Meneghetti. The impact of gas physics on strong cluster lensing. A&A, 442:405–412, November 2005.

[100] S. W. Randall, C. L. Sarazin, and P. M. Ricker. The Effect of Merger Boosts on the Luminosity, Temperature, and Inferred Mass Functions of Clusters of Galaxies. ApJ, 577:579–594, October 2002.

[101] K. Reblinsky. Cluster deprojection combining multiple observable data sets. A&A, 364:377–390, December 2000.

[102] K. Reblinsky and M. Bartelmann. Cluster Deprojection with Joint Lensing, X-ray, and Sunyaev-Zel'dovich Data. In T. G. Brainerd and C. S. Kochanek, editors, *Gravitational Lensing: Recent Progress and Future Go*, volume 237 of *Astronomical Society of the Pacific Conference Series*, pages 337–+, January 2001.

[103] T. H. Reiprich and H. Böhringer. The Mass Function of an X-Ray Flux-limited Sample of Galaxy Clusters. ApJ, 567:716–740, March 2002.

[104] E. Rozo, D. Nagai, C. Keeton, and A. Kravtsov. The Impact of Baryonic Cooling on Giant Arc Abundances. *ArXiv Astrophysics e-prints*, astro-ph/0609621, September 2006.

[105] G. B. Rybicki and A. P. Lightman. *Radiative processes in astrophysics*. John Wiley & Sons, New York, 1979.

[106] D. J. Sand, T. Treu, G. P. Smith, and R. S. Ellis. The Dark Matter Distribution in the Central Regions of Galaxy Clusters: Implications for Cold Dark Matter. ApJ, 604:88–107, March 2004.

[107] A. J. R. Sanderson, A. Finoguenov, and J. J. Mohr. Possible AGN Shock Heating in the Cool-Core Galaxy Cluster Abell 478. ApJ, 630:191–205, September 2005.

[108] C. L. Sarazin. *X-ray emission from clusters of galaxies*. Cambridge University Press, Cambridge, 1988.

[109] R. W. Schmidt and S. W. Allen. The dark matter haloes of massive, relaxed galaxy clusters observed with Chandra. MNRAS, 379:209–221, July 2007.

[110] P. Schneider, J. Ehlers, and E. E. Falco. *Gravitational lenses*. Springer, Berlin, 1992.

[111] M. Sereno, E. De Filippis, G. Longo, and M. W. Bautz. Measuring the Three-dimensional Structure of Galaxy Clusters. II. Are Clusters of Galaxies Oblate or Prolate? ApJ, 645:170–178, July 2006.

[112] R. K. Sheth, H. J. Mo, and G. Tormen. Ellipsoidal collapse and an improved model for the number and spatial distribution of dark matter haloes. MNRAS, 323:1–12, May 2001.

[113] R. K. Sheth and G. Tormen. Large-scale bias and the peak background split. MNRAS, 308:119–126, September 1999.

[114] G. Soucail, B. Fort, Y. Mellier, and J. P. Picat. A blue ring-like structure, in the center of the A 370 cluster of galaxies. A&A, 172:L14–L16, January 1987.

[115] G. Soucail, Y. Mellier, B. Fort, G. Mathez, and F. Hammer. Further data on the blue ring-like structure in A 370. A&A, 184:L7–L9, October 1987.

[116] D. N. Spergel, R. Bean, O. Doré, M. R. Nolta, C. L. Bennett, J. Dunkley, G. Hinshaw, N. Jarosik, E. Komatsu, L. Page, H. V. Peiris, L. Verde, M. Halpern, R. S. Hill, A. Kogut, M. Limon, S. S. Meyer, N. Odegard, G. S. Tucker, J. L. Weiland, E. Wollack, and E. L. Wright. Three-Year Wilkinson Microwave Anisotropy Probe (WMAP) Observations: Implications for Cosmology. ApJS, 170:377–408, June 2007.

[117] L. Spitzer. *Physics of Fully Ionized Gases.* Interscience, New York, 1962.

[118] V. Springel. The cosmological simulation code GADGET-2. MNRAS, 364:1105–1134, December 2005.

[119] V. Springel and L. Hernquist. Cosmological smoothed particle hydrodynamics simulations: the entropy equation. MNRAS, 333:649–664, July 2002.

[120] V. Springel and L. Hernquist. Cosmological smoothed particle hydrodynamics simulations: a hybrid multiphase model for star formation. MNRAS, 339:289–311, February 2003.

[121] V. Springel and L. Hernquist. The history of star formation in a Λ cold dark matter universe. MNRAS, 339:312–334, February 2003.

[122] V. Springel, S. D. M. White, A. Jenkins, C. S. Frenk, N. Yoshida, L. Gao, J. Navarro, R. Thacker, D. Croton, J. Helly, J. A. Peacock, S. Cole, P. Thomas, H. Couchman, A. Evrard, J. Colberg, and F. Pearce. Simulations of the formation, evolution and clustering of galaxies and quasars. Nature, 435:629–636, June 2005.

[123] V. Springel, N. Yoshida, and S. D. M. White. GADGET: a code for collisionless and gasdynamical cosmological simulations. *New Astronomy*, 6:79–117, April 2001.

[124] M. Steinmetz. Mergers and Formation of Disk Galaxies in Hierarchically Clustering Universes. In R. Bender and R. L. Davies, editors, *New Light on Galaxy Evolution*, volume 171 of *IAU Symposium*, pages 259–+, 1996.

[125] R. A. Sunyaev and I. B. Zeldovich. The velocity of clusters of galaxies relative to the microwave background - The possibility of its measurement. MNRAS, 190:413–420, February 1980.

[126] G. Tormen, F. R. Bouchet, and S. D. M. White. The structure and dynamical evolution of dark matter haloes. MNRAS, 286:865–884, April 1997.

[127] G. Tormen, L. Moscardini, and N. Yoshida. Properties of cluster satellites in hydrodynamical simulations. MNRAS, 350:1397–1408, June 2004.

[128] E. Torri, M. Meneghetti, M. Bartelmann, L. Moscardini, E. Rasia, and G. Tormen. The impact of cluster mergers on arc statistics. MNRAS, 349:476–490, April 2004.

[129] L. van Waerbeke. Noise properties of gravitational lens mass reconstruction. MNRAS, 313:524–532, April 2000.

[130] G. M. Voit. Tracing cosmic evolution with clusters of galaxies. *Reviews of Modern Physics*, 77:207–258, April 2005.

[131] J. Wambsganss, P. Bode, and J. P. Ostriker. Giant Arc Statistics in Concord with a Concordance Lambda Cold Dark Matter Universe. ApJ, 606:L93–L96, May 2004.

[132] J. Wambsganss, J. P. Ostriker, and P. Bode. The effect of baryon cooling on the statistics of giant arcs and multiple quasars. *ArXiv e-prints*, 0707.1482 [astro-ph], July 2007.

[133] S. D. M. White. Formation and Evolution of Galaxies. In R. Schaeffer, J. Silk, M. Spiro, and J. Zinn-Justin, editors, *Cosmology and Large Scale Structure*, pages 349–+. Elsevier, Amsterdam, January 1996.

[134] S. D. M. White, J. F. Navarro, A. E. Evrard, and C. S. Frenk. The Baryon Content of Galaxy Clusters - a Challenge to Cosmological Orthodoxy. Nature, 366:429–+, December 1993.

[135] B. C. Whitmore, D. M. Gilmore, and C. Jones. What determines the morphological fractions in clusters of galaxies? ApJ, 407:489–509, April 1993.

[136] S.-J. Xue and X.-P. Wu. Chandra X-Ray Observatory Observation of A1689: New Determination of Mass Distribution and Comparison to Lensing Measurements. ApJ, 576:152–158, September 2002.

[137] N. Yoshida, R. K. Sheth, and A. Diaferio. Non-Gaussian cosmic microwave background temperature fluctuations from peculiar velocities of clusters. MNRAS, 328:669–677, December 2001.

[138] N. Yoshida, F. Stoehr, V. Springel, and S. D. M. White. Gas cooling in simulations of the formation of the galaxy population. MNRAS, 335:762–772, September 2002.

[139] D. Zaritsky and A. H. Gonzalez. On the Incidence of Strong Gravitational Lensing by Clusters in the Las Campanas Distant Cluster Survey. ApJ, 584:691–701, February 2003.

[140] S. Zaroubi, G. Squires, G. de Gasperis, A. E. Evrard, Y. Hoffman, and J. Silk. Deprojection of Galaxy Cluster X-Ray, Sunyaev-Zeldovich Temperature Decrement, and Weak-Lensing Mass Maps. ApJ, 561:600–620, November 2001.

[141] S. Zaroubi, G. Squires, Y. Hoffman, and J. Silk. Deprojection of Rich Cluster Images. ApJ, 500:L87+, June 1998.

[142] Y. B. Zeldovich and R. A. Sunyaev. The Interaction of Matter and Radiation in a Hot-Model Universe. Ap&SS, 4:301–+, 1969.

[143] S. Zibetti, S. D. M. White, D. P. Schneider, and J. Brinkmann. Intergalactic stars in z˜ 0.25 galaxy clusters: systematic properties from stacking of Sloan Digital Sky Survey imaging data. MNRAS, 358:949–967, April 2005.

Appendix A

Richardson-Lucy deconvolution

Richardson-Lucy deconvolution is an iterative deconvolution scheme [59, 60]. The problem to be solved is finding a function $\phi(\xi)$ related to a known function $\psi(x)$ by the integral equation

$$\psi(x) = \int \phi(\xi) P(x|\xi) d\xi, \tag{A.1}$$

where the convolution kernel $P(x|\xi)$ is assumed to be known. For the moment also non-negativity and normalisation to unity is assumed, namely

$$\psi(x) \geq 0, \qquad \int \psi(x) dx = 1, \tag{A.2}$$

$$\phi(\xi) \geq 0, \qquad \int \phi(\xi) d\xi = 1, \tag{A.3}$$

$$P(x|\xi) \geq 0, \qquad \int P(x|\xi) dx = 1. \tag{A.4}$$

Then $\psi(x)$, $\phi(\xi)$, and $P(x|\xi)$ can be interpreted as probability distribution functions for x, ξ, and x for given ξ, respectively. Thus, using the inverse probability distribution function $Q(\xi|x)$ for ξ for given x, one can write

$$\psi(x) dx \times Q(\xi|x) d\xi = \phi(\xi) d\xi \times P(x|\xi) dx. \tag{A.5}$$

Plugging into Eq. (A.1) yields

$$Q(\xi|x) = \frac{\phi(\xi)P(x|\xi)}{\int \phi(\xi)P(x|\xi)d\xi}, \tag{A.6}$$

which is just Bayes' theorem. By integrating Eq. (A.5) over x and using the normalisation of $P(x|\xi)$ one finds

$$\phi(\xi) = \int \psi(x)Q(\xi|x)dx. \tag{A.7}$$

This equation, however, does not allow direct computation of $\phi(\xi)$ because $Q(\xi|x)$ depends on the sought function $\phi(\xi)$. However, an iterative solution is possible. Using some guess $\phi_n(\xi)$ for $\phi(\xi)$ one can derive

$$Q_n(\xi|x) \equiv \frac{\phi_n(\xi)P(x|\xi)}{\int \phi_n(\xi)P(x|\xi)d\xi}. \tag{A.8}$$

By plugging this into Eq. (A.7) another guess is obtained

$$\phi_{n+1}(\xi) = \int \psi(x)Q_n(\xi|x)dx = \phi_n(\xi)\int \frac{\psi(x)}{\psi_n(x)}P(x|\xi)dx, \tag{A.9}$$

where I defined

$$\psi_n(x) \equiv \int \phi_n(\xi)P(x|\xi)d\xi, \tag{A.10}$$

in analogy to Eq. (A.1). Hence if the input function $\psi(x)$ is some observed data, $\psi_n(x)$ is essentially the data that would be observed for the reconstruction $\phi_n(\xi)$ of $\phi(\xi)$.

From Eqs. (A.9) and (A.10) it follows that, if $\psi(x)/\psi_n(x)$ is different from unity on scales much larger than the extension of the convolution kernel $P(x|\xi)$, the deviation is removed in essentially one iteration. If it is different from unity on scales much smaller than the kernel, the contribution to the integral in Eq. (A.9) averages out and the algorithm is unresponsive.

Thus Richardson-Lucy deconvolution reproduces large scale features quickly while it converges only slowly to small scale fluctuations. If such small scale fluctuations in $\psi(x)$ are due to observational noise, it may be favourable to either abort the iteration after a couple of steps or to alternatively use a penalty function to suppress their impact on the reconstructions. More details about convergence behaviour and regularisation techniques can be found in [60].

Note, that the requirements that $\psi(x)$ and $\phi(\xi)$ are normalised to unity were only used to interpret them as probability distribution functions. They are actually not necessary for applying Eqs. (A.9) and (A.10) to perform a deconvolution.